Formation of bicontinuous structures through liquid film migration

Vom Promotionsausschuss der
Technischen Universität Hamburg
zur Erlangung des akademischen Grades
Doktor-Ingenieur (Dr.-Ing.)

genehmigte Dissertation (Monografie)

von

Zhongyang Li

aus

Shenyang, China

2026

Erstgutachter: Prof. Dr.-Ing. Jörg Weissmüller
Zweitgutachter: Prof. Carl E. Krill III, Ph.D.
Vorsitzender: Prof. Dr. rer. nat. Alexander Schlaich

Tag der mündlichen Prüfung: März 24, 2026

DOI: https://doi.org/10.15480/882.16950

ORCID iD: https://orcid.org/0009-0001-9796-9269

Acknowledgements

I would like to express my gratitude to my supervisor, Prof. Jörg Weißmüller, for his patient guidance, enlightening discussions and invaluable support. I am impressed by his profound knowledge and enthusiasm for scientific research. I feel privileged to have the opportunity to learn from him, whom I regard as a role model as a scientist.

I would also like to thank Dr. Lukas Lührs for the inspiring discussions and practical laboratory guidance he provided. With his help, I was able to have a smooth start and a satisfying completion of my PhD studiy.

My gratitude also goes to Prof. Carl Krill, my second reviewer, for his constructive feedback and for dedicating his valuable time to reviewing my thesis, and to Prof. Alexander Schlaich for chairing the examination.

Over the years, I have received countless help from my friends and colleagues, including Dr. Marine Bossert, Nina Petersen, Haonan Sun, Prof. Shan Shi, Dr. Yong Li, Haide Alfort-Springer, Dr. Xinyan Wu, Weiche Chang, Yizhou Huang, Dr. Seoyun Sohn, Dr. Jürgen Markmann, Ulrike Dette, Dr. Tim Fischer, Dr. Ying Zhang, Dr. Nadiia Mameka, Dr. Olga Matts, Celina Passig, Gideon Henkelmann, Dr. Robert Günther, Irene Bauer, Claudia Plaumann, Dr. Lukas Riedel, Dr. Tobias Krekeler, Dr. Gunnar Schaan, Jens Timmermann, Lida Wang, Andrea Bluhm. Their warm welcome and unwavering support really make not just my work, but also my life here a truly memorable experience.

Finally, I would like to thank my parents for their unconditional love. Their care and encouragement have made the many challenges along my journey far less daunting.

I gratefully acknowledge the financial support I received during my studies, including Deutsche Forschungsgemeinschaft (DFG), Germany within the Collaborative Research Centre CRC 986 “Tailor-Made Multi-Scale Materials Systems” (Project No. 192346071), Cluster of Excellence EXC 3120/1 BlueMat: Water-Driven Materials – 533771286, and China Scholarship Council.

Abstract

Bicontinuous structures, characterized by two interpenetrating and contiguous phases, exhibit unique properties in various metallic materials. Peritectic melting has been proposed as a novel dealloying method of fabricating bicontinuous structures, yet the underlying microstructure formation mechanism is still not fully understood.

In this work, we successfully obtained interpenetrating Ti and Ag phases after peritectic melting of TiAg. Further observation of partially decomposed samples, along with compositional and crystallography orientation studies suggest a fundamentally distinct microstructure formation mechanism from typical dealloying processes. The decomposition of TiAg during peritectic melting follows the liquid film migration mechanism, meaning that both Ti and Ag atoms dissolve into the melt, then deposit on the opposite grain as the equilibrium phase at the annealing temperature. The connectivity of the solid Ti phase comes from incompletely wetted grain boundaries.

Another example of bicontinuous structure formation via liquid film migration is peritectic melting of Ni_3Sn_4. A unique structure containing clusters of Ni_3Sn_2 cells are obtained. Different from the Ti phase, which forms through heterogeneous nucleation at wetted TiAg grain boundaries, Ni_3Sn_2 phase nucleates homogeneously within the melt. Subsequently, these nuclei experience cellular growth driven by the compositional gradient across the liquid layer. This finding indicates that different nucleation and growth mechanisms of the solid phase during peritectic melting result in diverse microstructures.

Partial melting may serve as an alternative to peritectic melting, without the strict requirement of a peritectic reaction. By heating a single-phase $Cu_{93}In_7$ solid solution to a solid-melt coexistence state, a bicontinuous structure consisting of Cu solid solution and solidified melt can be obtained. Here, the generalized method of initiating the melting process from pre-melting sites within the interior regions of the alloy is termed distributed internal melting (DIM).

In this thesis, the potential of DIM as a novel method of fabricating bicontinuous structures is demonstrated. The formation mechanism of bicontinuous structures during DIM of alloys is explained, which provides a basis for exploring other capable alloy systems.

Contents

List of Figures

List of Tables

Chapter 1

Introduction

1.1 Synthesis of bicontinuous structures

1.1.1 Bicontinuous structures

Bicontinuous structures refer to two interpenetrating and contiguous phases, each of them having a distinct composition or state of matter [1]. This kind of structure is found in various materials, including metal composites with two interpenetrating solid phases [2–5], as well as porous metals consisting of an interconnected metal network and open pores [6–9]. Examples of bicontinuous metal composites and porous metals are shown in Fig 1.1 below.

For some metal composites, bicontinuous structures are highly desirable, as they show enhanced mechanical properties including plasticity [10, 11], fracture resistance [12], yield strength [2, 13], and lower Young's modulus [4, 14]. Moreover, in porous metals, the presence of open pore channels reduces the density of the material and increases the surface area significantly. As a result, porous metals show better performance than dense metal materials in catalysis [15, 16], sound absorption [17], energy absorption [18], charge capacity [19], and electrochemical activities [20, 21].

Given the huge application potential of bicontinuous metal composites and porous

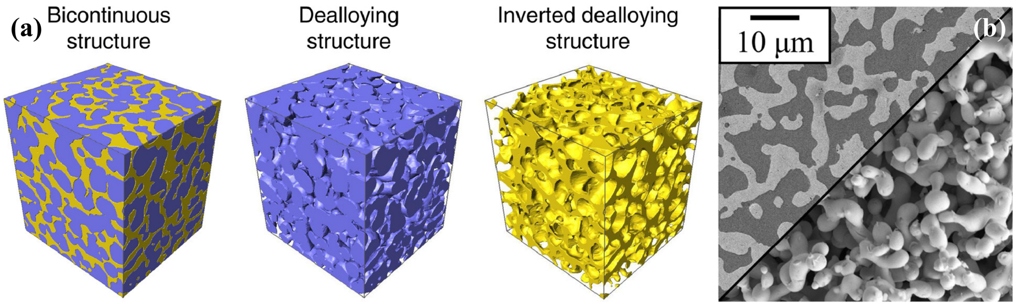

Figure 1.1: Bicontinuous structure of (a) a metal composite (reprinted from Ref [22] with permission) and (b) porous Ta (reprinted from Ref [3] with permission).

metals, the key challenge lies in developing effective synthesis strategies. According to percolation theories [23–25], volume fraction of each component can be an important factor in determining the connectivity of each phase. For instance, connectivity of both phases can be expected in spinodal decomposition, when the volume fraction of each phase is above 15% [23]. As a result, a bicontinuous structure can be a natural result of spontaneous processes, for example, interpenetrating α-Ti and Ti_2Cu phases after eutectoid reaction in Ti-25Cu (wt.%) alloy [26]. However, for the practical application of these materials, a tunable structure is an essential requirement. Here, various dealloying methods will be introduced as controllable approaches to fabricating bicontinuous structures.

1.1.2 Dealloying methods

Dealloying has long been studied as a form of corrosion [27, 28], before its potential in producing porous metals was discovered. The basic principle of different dealloying processes is similar. The pore channels are generated by selective removal of the sacrificial component, and the solid network forms through surface reorganization of the remaining component [29].

The most extensively studied dealloying process is electrochemical dealloying (ECD), in which the less noble component dissolves into aqueous electrolyte, driven by its above-equilibrium electrochemical potential. The dissolution and surface reorganization rates can be controlled experimentally, which allows the production of porous metals with tunable microstructures [8]. This can be achieved by altering the composition of the master alloy [30], dealloying time, temperature and potential [31, 32], as well as the concentration and nature of the electrolyte [33]. ECD is mainly applied to the manufacture of porous noble metals, due to the requirement of a significant difference in corrosion potential between different components.

Recent studies have shown that in addition to ECD, dealloying can also occur using molten or solid metal as the dealloying medium, respectively known as liquid metal dealloying (LMD) [34] and solid-state interfacial dealloying (SSID) [35]. Both processes generate bicontinuous structures through dissolution and surface reorganization mechanisms similar to those of ECD. However, the driving force differs. Instead of electrochemical potential, LMD and SSID rely on the difference in mixing enthalpy between the sacrificial element and the remaining component with the dealloying medium (metal melt or solid alloy) [35–37]. The distinct driving force enables the application of LMD and SSID on manufacturing porous metals with less noble elements, for example, Ti [34], Fe [35], Nb [38], Pb [39], Mo [40] and Mg [41].

Another novel dealloying method is vapor phase dealloying (VPD), which utilizes the difference in vapor pressure between the sacrificial component and the remaining component [42–44]. Like other dealloying techniques mentioned above, VPD also follows the dissolution and reorganization mechanism. The sacrificial phase is here the more volatile component, which evaporates from the master alloy to the atmosphere. This new

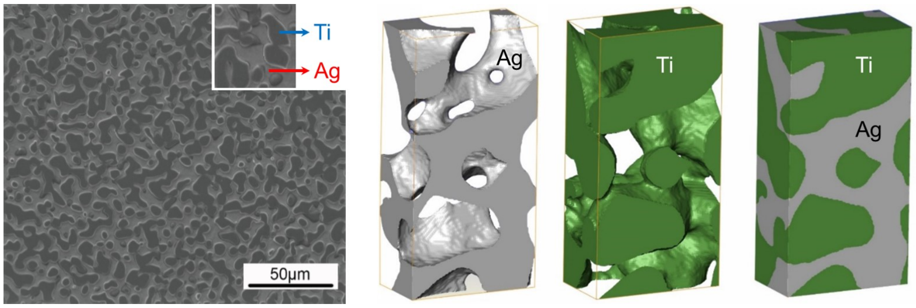

Figure 1.2: Bicontinuous structure consists of Ti and Ag phase obtained after peritectic melting of intermetallic compound TiAg and subsequent quenching. Image taken with promission from Ref [45].

method enables the fabrication of novel porous metals, such as porous Mn [44].

A peculiar case worth mentioning is the newly discovered dealloying method, namely peritectic melting [45]. It has been found that, after reverse peritectic reaction of intermetallic compound TiAg, a bicontinuous structure containing Ti and Ag networks can be obtained. The structure, shown in Fig 1.2, closely resembles that formed through LMD, which is a counterintuitive outcome after just simple heat treatment of the sample in the semi-solid state. This finding introduces a novel approach to fabricating bicontinuous structures. However, by far the TiAg remains the only successful master alloy for this method, and it is still unclear whether this qualifies as a true dealloying process. The main goal of this study is to discover the formation mechanism of bicontinuous structures during peritectic melting and potentially other types of phase transformation processes similar to peritectic melting.

1.1.3 Coarsening of dealloyed structures

Coarsening has an important effect on the microstructural evolution of the dealloyed structure, as it is ubiquitous in all dealloying processes. For nanoporous metals produced by dealloying, due to the large surface area, the dealloyed structure is thermodynamically unstable and prone to coarsening at elevated or even room temperature [8, 42, 46–48]. The coarsening of the nanoporous metal is governed by the pinch-off effect, caused by Rayleigh instability of the ligaments [49, 50]. This could be a self-similar (same morphology regardless of the length scale) coarsening process [51–54], associated with a decrease in local genus [49]. The coarsening of nanoporous gold is shown in Fig 1.3 as an example.

Coarsening of the dealloyed structure can have a detrimental effect on practical application of nanoporous materials, since the total surface area decreases with increasing ligament size, resulting in deterioration of physical properties [55, 56]. For low solid volume fraction nanoporous networks, coarsening further compromises connectivity and stiffness [57, 58]. For deposited samples, the detachment of the dealloyed nanoporous gold layer from the pure gold substrate [59] is also caused by coarsening during the dealloying

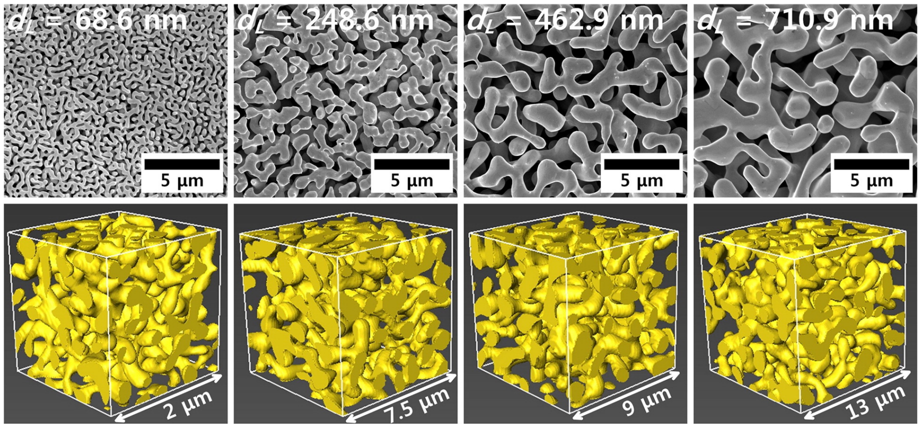

Figure 1.3: Scanning electron microscopy image and focus ion beam volume reconstruction of nanoporous gold at different coarsening stages. Image taken from Ref [53] with permission.

process. The negative effects of coarsening can be mitigated by suppressing surface diffusion. This can be achieved by adding noble components with low surface mobility [60, 61], or by maximizing configurational entropy in high-entropy nanoporous alloys [56].

On the other hand, a well controlled coarsening process can be used to tune the physical and mechanical properties of nanoporous materials, by adjusting the ligament size [11, 62–64]. Fabrication of hierarchical nanoporous metals also utilizes the coarsening process to develop the upper level of structural hierarchy [65, 66]. A hierarchical structure can be obtained through sequential processes including the first-step dealloying, coarsening, and the second-step dealloying. Schematic showing the preparation of hierarchical nanoporous gold is shown in Fig 1.4.

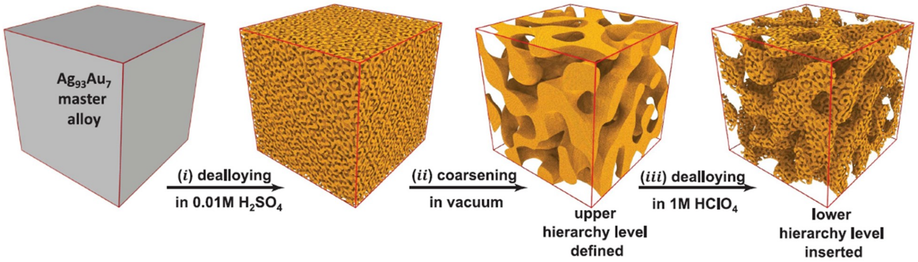

Figure 1.4: Schematic of the two-step dealloying process during fabrication of hierarchical nanoporous gold. Image taken from Ref [66].

1.2 Melting of metal alloys

1.2.1 Differences between melting and solidification

Melting and solidification of alloys play critical roles in various metal processing techniques, including casting [67], joining [68], semi-solid processing [69], surface remelting [70] and additive manufacturing [71]. Despite having significant effects on microstructural evolution, research on melting is relatively scarce compared to its counterpart, the solidification process [72]. Since both processes involve phase transformation between a solid phase and a liquid phase, it is natural to consider applying the relatively well established theories of solidification to the melting process. However, the assumption of solidification and melting as symmetrical processes is incorrect, due to the different behaviors of the solute atoms [72]. The asymmetry of the two processes can be found in many aspects.

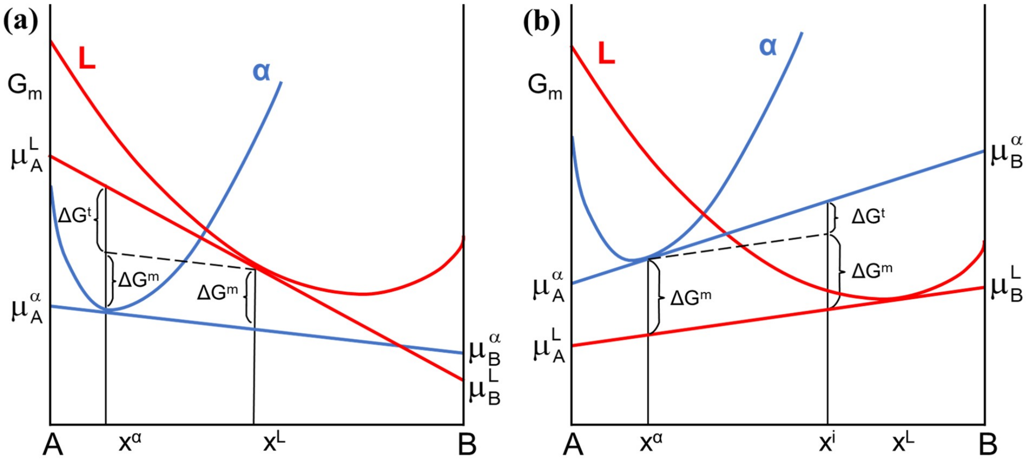

Figure 1.5: Molar Gibbs energy diagram of (a) solidification process and (b) melting process. x^α and x^L are the compositions of the solid and the liquid phase, and x^i is the intermediate composition during melting. $\mu_\mathrm{i}^\mathrm{j}$ refers to the chemical potential of atom *i* in phase *j*. ΔG^m and ΔG^t are the driving forces for interface migration and trans-interface diffusion respectively. Displacements of free energy curves of α and *L* between (a) and (b) are the results of different temperatures chosen for the solidification and melting processes. Schematic redrawn from Ref [73] with permission.

For the solidification process, consider a layer of melt *L* containing A and B atoms with a composition x^L that transforms into solid phase α with a composition x^α. The energy change of this process is illustrated in Fig 1.5 (a), the total change in Gibbs energy, $\Delta G_\mathrm{m}^\mathrm{total}$, is given as

$$\Delta G_\mathrm{m}^\mathrm{total} = (1 - x^\alpha)(\mu_\mathrm{A}^\mathrm{L} - \mu_\mathrm{A}^\alpha) + x^\alpha(\mu_\mathrm{B}^\mathrm{L} - \mu_\mathrm{B}^\alpha) \tag{1.1}$$

Here, $\mu_\mathrm{i}^\mathrm{j}$ represents the chemical potential of atom *i* in phase *j* [74]. Based on the work of

Hillert [75], the equation can be rewritten into the following form:

$$\Delta G_{\mathrm{m}}^{\mathrm{total}} = (1 - x^{\mathrm{L}})(\mu_{\mathrm{A}}^{\mathrm{L}} - \mu_{\mathrm{A}}^{\alpha}) + x^{\mathrm{L}}(\mu_{\mathrm{B}}^{\mathrm{L}} - \mu_{\mathrm{B}}^{\alpha}) + (x^{\mathrm{L}} - x^{\alpha})(\mu_{\mathrm{A}}^{\mathrm{L}} - \mu_{\mathrm{A}}^{\alpha} - \mu_{\mathrm{B}}^{\mathrm{L}} + \mu_{\mathrm{B}}^{\alpha}) \quad (1.2)$$

The first two terms are the Gibbs energy change of 1 mol *L* with composition x^{L} dissolving into the solid phase α, which will be denoted as ΔG^{m}. The last term, denoted as ΔG^{t}, describes the loss of Gibbs energy caused by composition adjustment from x^{L} to x^{α}, achieved by diffusion of A and B atoms between the two phases. Hence, the two terms can be written as:

$$\Delta G^{\mathrm{m}} = (1 - x^{\mathrm{L}})(\mu_{\mathrm{A}}^{\mathrm{L}} - \mu_{\mathrm{A}}^{\alpha}) + x^{\mathrm{L}}(\mu_{\mathrm{B}}^{\mathrm{L}} - \mu_{\mathrm{B}}^{\alpha}) \quad (1.3)$$

$$\Delta G^{\mathrm{t}} = (x^{\mathrm{L}} - x^{\alpha})(\mu_{\mathrm{A}}^{\mathrm{L}} - \mu_{\mathrm{A}}^{\alpha} - \mu_{\mathrm{B}}^{\mathrm{L}} + \mu_{\mathrm{B}}^{\alpha}) \quad (1.4)$$

Here, it is assumed that the growing phase (α in the case of solidification) does not exist initially, and the change in composition from x^{L} to x^{α} is accomplished entirely by diffusion inside the parent phase. In this condition, solidification and melting can be a symmetrical process in thermodynamic aspects. The analysis is still correct for the solidification process when the product phase (α) already exists, under the assumption that diffusion in α is considerably slow, or α precipitates with a constant composition. In that case, no diffusion is expected in the product phase. However, this may not be true for the melting process when the liquid phase already exists. The diffusion rate of atoms in the liquid phase is too fast to be neglected, and the composition gradient in the liquid phase can modify the interface composition. As a result, the composition change from x^{α} to x^{L} should also take into account diffusion in the product phase (*L*). This is shown by the molar Gibbs energy diagram in Fig 1.5 (b). To calculate the driving force in this scenario, an intermediate composition x^{i} is introduced and Equation 1.2 can be rewritten as:

$$\Delta G_{\mathrm{m}}^{\mathrm{total}} = (1 - x^{\alpha})(\mu_{\mathrm{A}}^{\alpha} - \mu_{\mathrm{A}}^{\mathrm{L}}) + x^{\alpha}(\mu_{\mathrm{B}}^{\alpha} - \mu_{\mathrm{B}}^{\mathrm{L}}) + (x^{\alpha} - x^{\mathrm{i}})(\mu_{\mathrm{A}}^{\alpha} - \mu_{\mathrm{A}}^{\mathrm{L}} - \mu_{\mathrm{B}}^{\alpha} + \mu_{\mathrm{B}}^{\mathrm{L}}) \quad (1.5)$$

and x^{i} is decided by the flux of solute atoms (B atoms) toward the interface in both phases [73].

Apart from the thermodynamic aspect, another difference between the two processes is solute partitioning. During solidification, solute rejection is expected to happen. This leads to solute enrichment at the solidification front. For the melting process, solute concentration at the interface is usually the lowest, as diffusion in the solid phase is not fast enough to transport solute atoms toward the interface [72].

Asymmetry may also arise due to the difference in atomic accommodation at the interface: solid metal usually has a crystal structure, whereas metal melt does not display a long-range order. During solidification, deposition of atoms on an atomically smooth faceted surface is less favorable than on a rough surface, which leads to faceted growth of the crystal. For melting, the atoms can be accommodated at any location at the interface, which usually results in a rough melting front [76].

1.2.2 Pre-melting

Pre-melting refers to melting of solids below the equilibrium melting temperature. The notion was initially postulated by Faraday [77], who observed surface melting of ice, and then was found in metal systems including Pb [78], Al [79], Cu [80], and Ni [81]. Surface melting of metals is closely related to the surface orientation, for example, surface melting of Pb occurs at various crystal faces, but not for a zone around (111) orientation [82]. Additionally, surface strain can also affect the melting behavior at the surface. Although a lower melting point is expected for a strained (both positive and negative) solid, the effect on the onset temperature of surface melting is different [83]. Positive strain will always lower the surface melting temperature, while negative strain will lead to incomplete or even non-melting at the surface.

It is a natural thought to compare the pre-melting behavior at the surface with that at the interface in polycrystalline materials. Indeed, grain boundary pre-melting in pure Al has been found $4\,^{\circ}\mathrm{C}$ below the equilibrium melting temperature and a similar effect has been observed for several other materials [84–86]. For alloys, pre-melting can also be induced by solute segregation at grain boundaries [87]. Apart from surfaces and interfaces, pre-melting is also expected to occur at dislocations [88] and vacancies [89]. Based on the experimental evidence mentioned above, together with various simulation studies [90–92], it can be concluded that pre-melting happens at loosely packed areas of the crystal structure [72].

It is common for melting to happen below equilibrium melting point for bulk metals due to various pre-melting behaviors. As a result, superheating of metal solid is hard to achieve in experiments. However, it is still observable if the pre-melting process is suppressed. This can be achieved by coating or embedding the single crystal metal particle with high melting point materials [93, 94]. In contrast, solidification of metals is never observed above the melting point. Certain degrees of supercooling are required, since the additional interfacial energy acts as a barrier to the nucleation process [95].

1.2.3 Partial melting and peritectic melting

Partial melting refers to the heat treatment of materials within the two-phase region, where both the solid and liquid phases coexist. This technique is widely employed in fundamental studies, for example, on grain boundary wetting [96–98], as well as metal forming technologies, such as semisolid metal processing [99, 100].

Partial melting is an important method to tune the microstructure of the materials. It can induce the separation of grains by wetting the grain boundaries with the melt. This process is particularly relevant in semisolid metal processing, where a non-dendritic semisolid slurry is the desired microstructure. The structural evolution of inclusions during partial remelting has been extensively studied in many alloy systems [101–103], showing that fine globular structure can emerge from initially dendritic or rosette-like structures [104]. This is attributed to the combination effect of Ostwald ripening and coalescence [104].

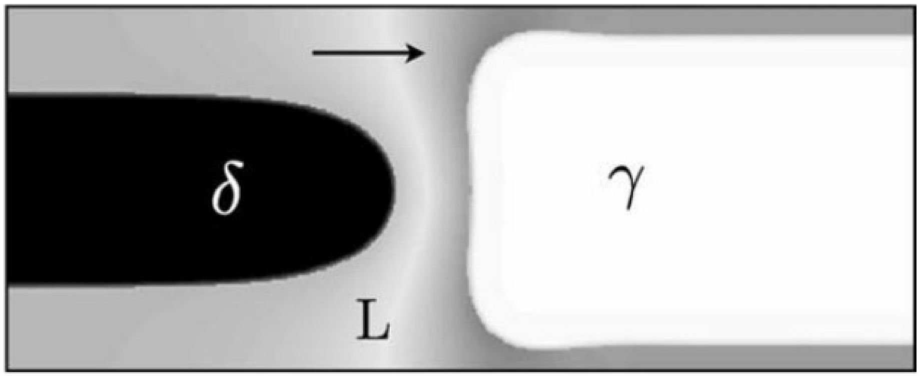

Figure 1.6: Phase field simulation of the peritectic melting process of γ phase decomposes into δ phase and the melt. The black arrow indicates the reaction direction, the δ phase grows at the expense of γ phase, with a liquid layer in between. Schematic taken from Ref [107] with permission.

Peritectic melting refers to the decomposition of one solid phase through a reverse peritectic reaction. This process shares similarity with partial melting, as both processes result in a solid-liquid two phase coexistence state. However, compared to partial melting, peritectic melting has been significantly less studied. One study on peritectic melting of a Fe-Cr-Ni alloy observed spherical ferrites after decomposition of dendritic austenite at an elevated temperature [105]. Based on that observation, the study concluded that the reverse peritectic reaction always results in spherical structures, under the assumption that the newly formed phase should be completely wetted by the melt. However, a counterexample of that will be peritectic melting of TiAg introduced in the previous section. Certainly more experiments are required to verify that conclusion.

The peritectic melting process is also studied using phase field simulations [106–109]. These simulations suggest that peritectic melting follows a liquid film migration (LFM) mechanism, which means complete dissolution of the parent phase and simultaneous precipitation of the new solid phase, as shown in Fig 1.6. This mechanism is indirectly supported by the observation of dendrite fragmentation in Ti-Al alloy [110], however, direct evidence of LFM during peritectic melting has not yet been found. In this thesis, experimental results supporting the LFM mechanism will be given.

1.3 Liquid film migration

1.3.1 Liquid film migration processes

Diffusion induced grain boundary migration (DIGM) refers to chemically induced migration of different types of boundaries, including grain boundaries, liquid films, and solid/liquid interfaces. The moving boundary, as a reaction front, usually results in composition or orientation changes between the product phase and the matrix [111–113]. One special case of DIGM is liquid film migration, which refers to the movement of a liquid layer in a predominantly solid structure. LFM is distinguished from other types of DIGM by the presence of the liquid layer, which offers a fast mass transportation pathway compared to bulk or interface diffusion. LFM has been observed in various materials including metals and ceramics, and in different processing methods, such as sintering, brazing, welding, partial melting, and also solidification. The occurrence of LFM during different processes is listed in table 1.1 below.

As mentioned above, the LFM process can be described as simultaneous melting and solidification at different liquid/solid interfaces. The solidification process on one side of the liquid film provides the latent heat required for melting on the opposite side. Since enthalpic effects are not involved in this process, the liquid film is highly mobile [72].

Melting/resolidification mechanisms similar to LFM has been observed as well. Temperature gradient zone melting is one example of such mechanisms: under an imposed steep temperature gradient, liquid droplet migrates through the solid phase in order to adjust the equilibrium composition [114]. However, a temperature gradient is not required during LFM, as it can happen during isothermal heat treatments. LFM also shares similarity with the already discounted dissolution/deposition mechanism for the electrochemical dealloying of non-noble alloys [115]. The major difference between the two mechanisms lies in the direction of atom diffusion. According to the dissolution/deposition mechanism, atoms diffuse to the nearest ligaments, whereas in LFM, atoms diffuse across the liquid layer.

1.3.2 Structures formation through liquid film migration

The unique microstructure formed through LFM during different materials processing techniques have been extensively studied. Figure 1.7 (a) [122] shows the microstructure of a sintered Mo-Ni alloy reheated above the sintering temperature. The temperature change alters the equilibrium composition, causing the Mo-Ni grains to move towards a new equilibrium through diffusion. The arrows in Fig 1.7 (a) indicate the original grain boundaries, and a clear contrast can be found between two sides of the interface. The brighter contrast corresponds to a higher Ni content, which is the newly formed phase at equilibrium at the reheating temperature. A convex solid/liquid interface is visible at the growth front of the new phase, while a concave interface is found at the opposite matrix grain, with a liquid layer separating the two phases. The characteristic microstructure here suggests that the growth of the new phase is at the expense of the matrix grain.

In addition to smoothly curved interfaces, highly faceted interfaces were also observed during LFM, as demonstrated in Fig 1.7 (b) [151]. The liquid film is sectioned perpendicular to the (100) axis of the dissolving Co-Cu grain, indicating that the shape of the newly formed phase is determined by the orientation of the receding grain. This is further supported by the observation of two nearly parallel liquid films migrating into the same grain [151]. A similar faceted structure is also found during isothermal heat treatment of a sintered Fe-Cr-Mo alloy [120]. The special C-shaped TiC particles in commercial TiC-Fe alloys

Table 1.1: Liquid film migration in different material systems

system	process	reference	system	process	reference
Al-Cu-Mg-Fe	sintering	[116]	Ni-Cr-Co	welding	[117]
Co-Cu	sintering	[118]	Ni-Cr-Fe	welding	[119]
Fe-Cr-C	sintering	[120]	Ni-Co-Nb	welding	[121]
Mo-Ni	sintering	[122, 123]	Fe-Ni-Cr	welding	[124]
Mo-Ni-W	sintering	[125]	Al-Si	partial melting	[126, 127]
Mo-Ni-Fe	sintering	[128]	Al-Cu	partial melting	[129–131]
Mo-Ni-Co-Sn	sintering	[132, 133]	Al-Cu-Mg	partial melting	[134]
Nb_2O_5-$SrTiO_3$-CuO	sintering	[135]	Co-Cu	partial melting	[118]
Nd-Fe-B-Tb	sintering	[136]	Cu-In	partial melting	[137, 138]
W-Ni-Fe	sintering	[139]	CoCrCuFeNi	partial melting	[140]
ZrO_2-Y_2O_3	sintering	[141]	Fe-Al-Zn	partial melting	[142]
ZrO_2-CaO-MgO	sintering	[143]	Mg-Al	partial melting	[144]
ZrO_2-CeO_2-La_2O_3	sintering	[145]	Mo-Ni	partial melting	[122]
Al-Fe-Mn-Si	brazing	[146, 147]	Ni-Sn	solidification	[148, 149]
Al-Mn-Cu-Mg	brazing	[150]	Ti-Al	solidification	[110]

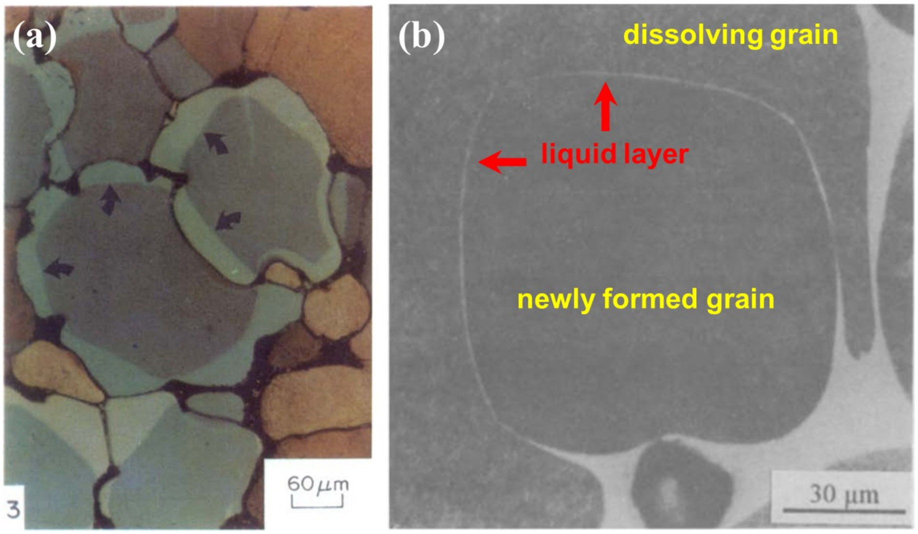

Figure 1.7: Structure obtained after liquid film migration. (a) Microstructure of Mo-Ni sintered at 1400 °C for 20 h and annealed at 1510 °C for 1 h. The contrast difference comes from the composition-sensitive etching process. Arrows indicate original grain boundaries. Figure taken from Ref [122] with permission. (b) Microstrcuture of a Co-Cu alloy sintered at 1300 °C for 20 h then reheated at 1150 °C for 3 h. A faceted structure can be observed. Figure adapted from Ref [151] with permission.

is another example [152]. These findings suggest that LFM, like other DIGM processes [153–155], is also dependent on the crystal orientation.

1.4 Outline of the thesis

This thesis will be structured as described below.

Theoretical background for the discussion of this thesis is presented in detail in Chapter 2. The concept of grain boundary wetting and its dependence on boundary orientation is introduced, as it is essential for analyzing the connectivity of the newly formed solid phase during partial melting. Afterward, the mechanism of bicontinuous structure formation during LMD is explained, for comparison with our LFM mechanism proposed for peritectic melting. The interface instability is introduced for later analysis on the morphology of the newly formed solid phase. Finally, the thermodynamic basis of the parallel tangent construction is given for composition analysis of Ti nuclei.

Chapter 3 provides experimental details including information on sample preparation, experimental setup, and characterization techniques.

Chapter 4 focuses on peritectic melting of TiAg. The experimental results presented in the previous paper are first verified, then a more detailed study on structural evolution and the coarsening effect is performed. Based on both structural and compositional studies of the partially decomposed samples, contradictions between the previously proposed dealloying-like mechanism and our observations are pointed out. A new structure formation mechanism compatible with our experimental findings is given.

Chapter 5 studies the peritectic melting of Ni_3Sn_4 intermetallic compound. The peculiar structure obtained after peritectic melting and quenching is observed and analyzed. The different nucleation and growth mechanisms between peritectic melting of Ni_3Sn_4 and TiAg are investigated and explained in detail.

Chapter 6 examines the structural evolution of a Cu-In alloy during partial melting. The connectivity of both phases is verified through a dealloying test, and the coarsening effect is analyzed with prolonged annealing durations. The discussion in this chapter focuses on the microstructure formation through LFM during partial melting and the extension of the fabrication method from peritectic melting to distributed internal melting.

Chapter 7 as the last chapter summarizes the experimental results and the proposed structure formation mechanism in this thesis. An outlook on the potential application of this novel method for fabricating bicontinuous structures is also given.

Chapter 2

Fundamentals

2.1 Grain boundary wetting

Grain boundary wetting typically occurs at the initial stage of melting in a polycrystalline material. The wetting behavior at the grain boundary is characterized by the dihedral angle θ as shown in Fig 2.1. Given the value of θ, the grain boundary is either completely (θ = 0) or incompletely wetted ($\theta > 0$). The equilibrium condition for wetting is described by the following equation:

$$\cos(\frac{\theta}{2}) = \frac{\gamma_{\mathrm{GB}}}{2\gamma_{\mathrm{SL}}} \tag{2.1}$$

where γ_{GB} and γ_{SL} represent the excess free energies of the grain boundary and the solid/liquid interface respectively [156].

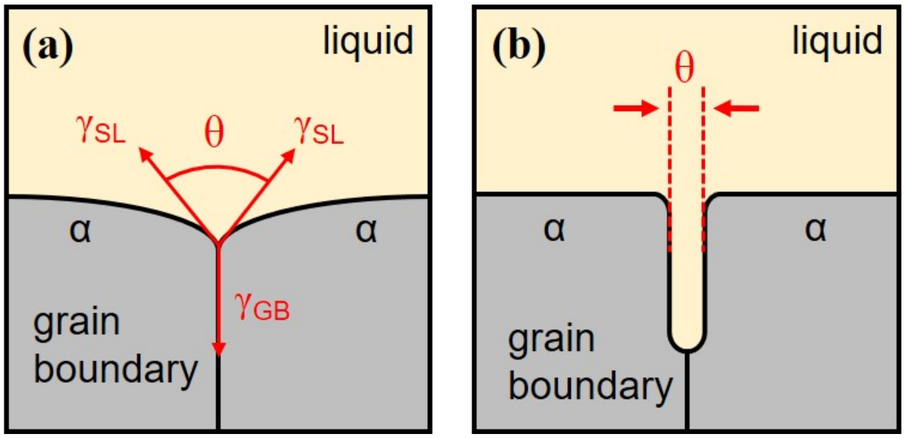

Figure 2.1: Schematic of different types of grain boundary wetting. (a) Incompletely wetted grain boundary, with a contact angle $\theta > 0$. (b) Completely wetted grain boundary, θ = 0.

A transition from the incomplete wetting state to complete wetting may occur above a critical temperature, T_{w} [157–159], which depends on the grain boundary energy and the liquid/solid interfacial energy [96, 160, 161].

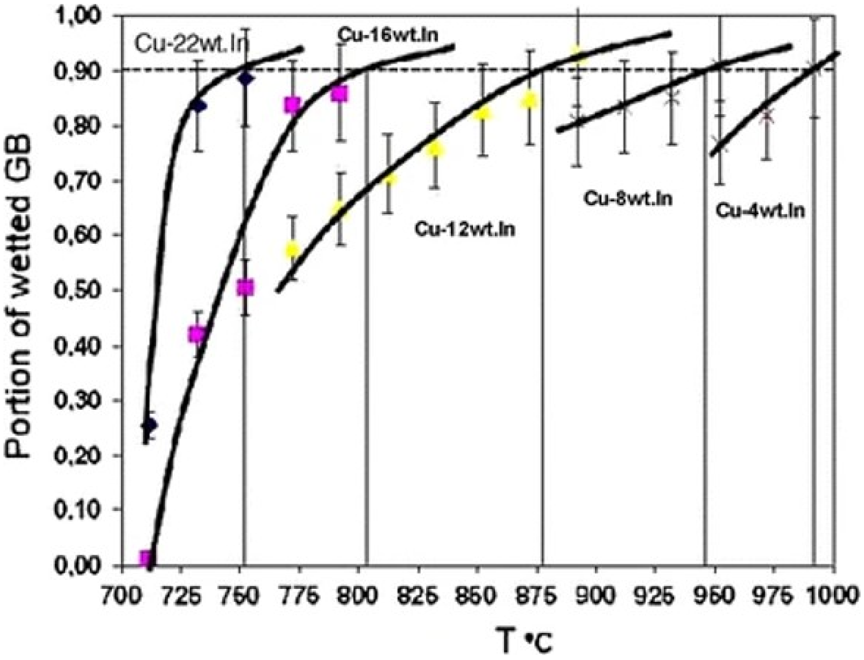

Figure 2.2: Fraction of completely wetted grain boundaries of Cu-In alloys with various In contents at different annealing temperatures. The Cu-In alloy studied in this work (see Chapter 6) has the same composition as 'Cu-12 wt.In' in this figure. Image taken from Ref [96] with permission.

In polycrystalline materials, different grain boundaries exhibit distinct wetting behaviors, and the relationship between grain boundary energy and crystallography orientation of the boundaries has been studied for a long time [162–164]. For example, boundaries with special orientation relationships, such as $\Sigma 3$ coincident site lattices, usually have lower boundary energies compared to randomly oriented boundaries [165].

In the case of Cu-In alloys, various types of boundary can be observed in the Cu solid solution phase, resulting in different wetting behaviors [96, 166]. When heated from the single-phase region (Cu solid solution) to the solid-liquid coexistence region in the phase diagram, only a fraction of the boundaries experience complete wetting. Figure 2.2 illustrates the relationship between the annealing temperature and the fraction of completely wetted grain boundaries. It is evident that both completely and incompletely wetted boundaries exist after annealing.

2.2 Structural evolution during LMD

LMD is able to generate a porous solid network similar to an electrochemically dealloyed structure, despite having a different driving force [34, 167]. A schematic of the LMD process is illustrated in Fig 2.3. During LMD, driven by the negative enthalpy of mixing between the dissolving component A and the metal melt, the sacrificial element (A) atoms dissolve into the liquid metal. The remaining component B reorganizes through surface diffusion at the dealloying front, resulting in a porous network. Meanwhile, the clustering of the B atoms by lateral diffusion along the interface exposes fresh surfaces, allowing the dealloying process to proceed further into the master alloy.

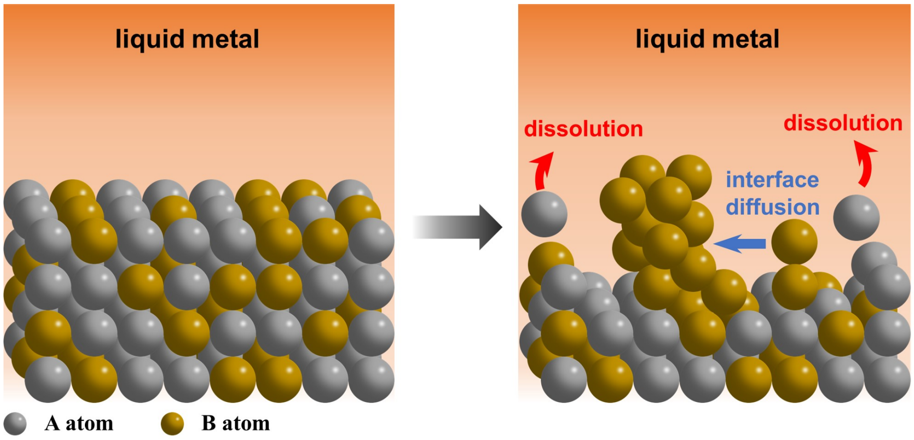

Figure 2.3: Schematic of the liquid metal dealloying (LMD) process. Master alloy contains A (sacrificial component) and B (remaining component) atoms. During LMD, A atoms dissolve into the liquid metal, and B atoms form clusters through interface diffusion. The resulting structure is the porous solid network of B.

A major drawback of dealloying methods is the limitation on the sample size. During ECD, the dealloying velocity is sufficiently low compared to the diffusion rate of metal ions in the electrolyte to maintain a constant dealloying velocity [168, 169]. The rate-limiting step during LMD is different from that of electrochemical dealloying, since LMD operates in liquid metal instead of electrolyte. During LMD, the dealloying velocity is expected to be orders of magnitude faster than in ECD, with the mass transportation of sacrificial elements in the melt being the rate-controlling process [37, 167, 170]. As LMD proceeds into the master alloy, mass transport in the melt becomes increasingly difficult, leading to a reduction in the dealloying velocity.

2.3 Morphological instability of solid/liquid interfaces

2.3.1 Solute concentration at a moving solid/liquid planar interface

The alloy microstructure after solidification can be greatly affected by the growth mechanism of the solid phase, which is closely related to the stability of the solidification front. During solidification, solute atoms will generally be rejected into the melt at the solid/liquid interface, due to their lower solubility in the solid phase. These solute atoms will accumulate ahead of the interface, resulting in a solute-enriched boundary layer in the melt. The solute concentration at the solidification front is shown in the schematic in Fig 2.4.

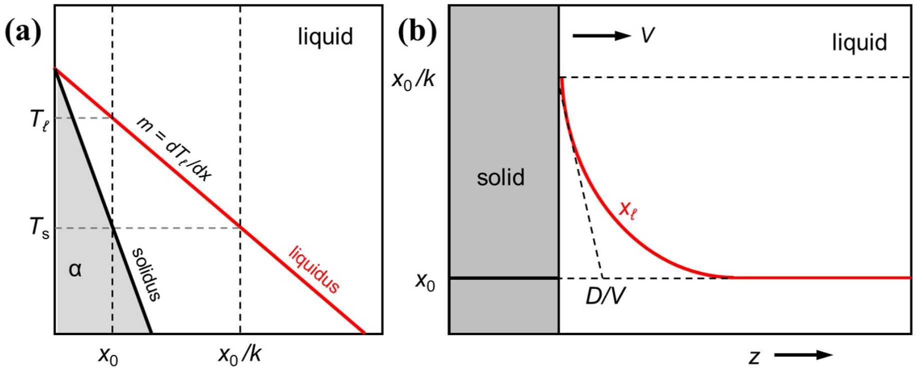

Figure 2.4: Schematic of solute concentration during solidification of an alloy, with the composition x_0. (a) Simplified phase diagram showing the solidus and liquidus line. (b) Steady-state boundary layer in front of the planar solid/liquid interface. The schematics were redrawn from Ref [171].

Consider the solidification of an alloy melt with an initial solute concentration x_0, with the corresponding phase diagram illustrated in Fig 2.4 (a). Assuming local equilibrium at the interface, the difference in composition between the solid and liquid phases is described using the distribution coefficient k, given by the following equation:

$$k = \frac{m_\ell}{m_\mathrm{s}} \tag{2.2}$$

where m_ℓ and m_s represent the slope of the liquidus and solidus line, respectively. For simplicity, both liquidus and solidus lines are drawn as straight lines. The formation of a solid phase with the composition x_0 leads to a local change in solute concentration. The liquid composition at the interface, x_0/k is determined by the liquidus line. The steady-state solute concentration during solidification is shown in Fig 2.4 (b). Within the solid phase, the solute concentration is expected to be constant at x_0. However, inside the liquid phase, the solute concentration decrease from x_0/k at the interface to x_0 away from the interface.

According to Ref [172], the solute concentration decreases exponentially in front of the solid/liquid interface. The liquid concentration x_ℓ in the boundary layer is calculated as:

$$x_\ell = x_0 + (\frac{x_0}{k} - x_0)\exp(-\frac{Vz}{D}) \tag{2.3}$$

where V represents the rate of interface movement in z direction, and D is the solute diffusion coefficient in liquid. At the solid/liquid interface, z equals 0.

2.3.2 Interface instability and constitutional supercooling

During solidification, the solid/liquid interface can be affected by random disturbances, such as temperature fluctuations. If the perturbation promotes further development of itself, the interface is considered unstable; otherwise, a stable interface is expected. For solidification of pure metals, a simple criterion exists. A stable interface can be obtained when the temperature gradient in front of the interface is positive, and a negative temperature gradient leads to an unstable interface. However, such a simple criterion is not enough to characterize the interface of alloys during solidification. The solute concentration at the interface should also be considered, as it affects the local equilibrium solidification point.

Based on Fig 2.4 (a), the local equilibrium liquidus temperature T_ℓ is decided by the liquid composition as :

$$T_\ell(x_0) - T_\ell(x_\ell) = m_\ell(x_0 - x_\ell) \tag{2.4}$$

here, $T_\ell(x_0)$ refers to the liquidus temperature of the initial composition x_0. At the interface (*z=0*), the imposed temperature T_q is equal to the liquidus temperature. Based on the discussion in the above section (see Fig 2.4), the composition of the melt at the interface is equal to x_0/k.

The stability of the interface is affected by the actual temperature imposed by the external heat flux, and the liquidus temperature T_ℓ decided by the solute composition in the liquid phase. If the actual temperature T_q is lower than the local liquidus temperature T_ℓ, the melt is in the supercooling state, resulting in an unstable solidification front. Both stable and unstable interfaces during solidification are illustrated in Fig 2.5.

The stability of the interface can be predicted by the temperature gradient G_t at the interface, which is defined as

$$G_\mathrm{t} = (\frac{\mathrm{d}T_\mathrm{q}}{\mathrm{d}z})_{z=0} \tag{2.5}$$

The gradient of liquidus temperature G_ℓ at the interface is defined as

$$G_\ell = (\frac{\mathrm{d}T_\ell}{\mathrm{d}z})_{z=0} = m_\ell G_\mathrm{x} \tag{2.6}$$

G_x represents the concentration gradient at the interface. A stable interface is expected if T_q is always higher than T_ℓ in the melt, in which case, the actual temperature gradient should always be larger than the liquidus temperature gradient at the interface (z=0). As a result, the criterion for morphological instability is :

$$G_\mathrm{t} < m_\ell G_\mathrm{x} \tag{2.7}$$

When $G_\mathrm{t} > m_\ell G_\mathrm{x}$, as shown in Fig 2.5 (a), the actual temperature is always higher than the solidification temperature of the melt. The resulting microstructure is a planar solid/liquid interface during solidification. The situation of constitutional supercooling is drawn in Fig 2.5 (b), where $G_\mathrm{t} < m_\ell G_\mathrm{x}$. As a result, a region exists in front of the interface

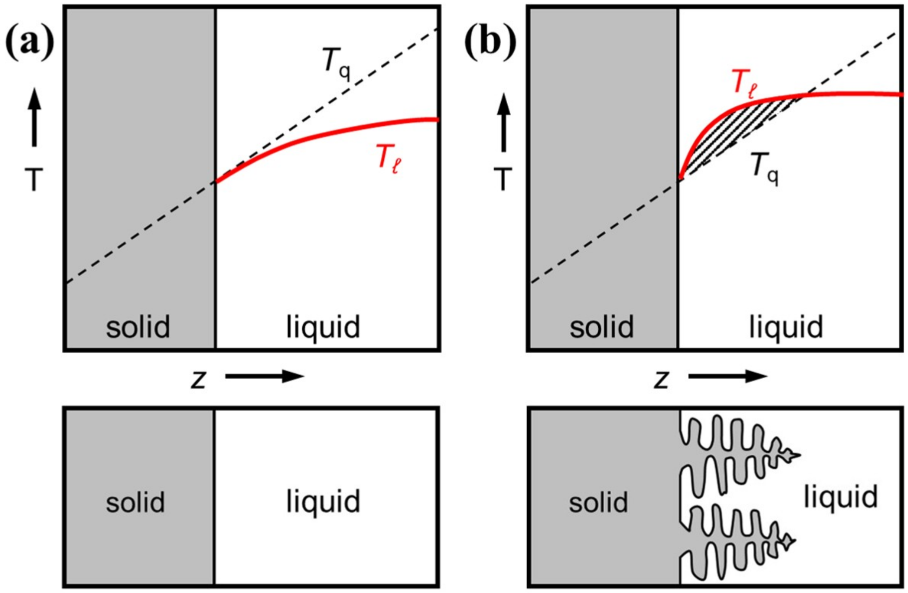

Figure 2.5: Morphological evolution of a solid/liquid interface during solidification. (a) planar growth of the interface. The actual temperature T_q in front of the interface is larger than the liquidus temperature of the melt, no constitutional supercooling zone exists, thus a planar interface is maintained during growth of the solid phase. (b) T_q is lower than T_ℓ in certain region (shaded area), forming a constitutional supercooling zone ahead of the interface, which favors the cellular or dendritic growth of the solid phase. Schematic redrawn from Ref [171].

where the actual temperature T_q is lower than the local liquidus temperature (T_ℓ), as indicated by the shaded area between the T_ℓ line and the T_q line. If any perturbation advances the solidification and forms a tip at the interface, the tip will encounter supercooling, which provides a driving force for the tip to grow. This means that the instability of the interface will increase, resulting in cellular or dendritic growth of the solid phase.

2.4 Parallel tangent construction

Gibbs free energy diagrams can be a useful tool to determine the driving force of phase transformation, and the composition of newly formed phases [74, 173, 174]. In this section, the parallel tangent method will be introduced, which is commonly employed to analyze the precipitation process in a supersaturated melt [175, 176]. The parallel tangent construction of the precipitation process of the β phase from a supersaturated α phase is illustrated in Fig 2.6.

Consider the equilibrium between the α phase with an initial composition x_α (supersaturated with B atoms), and the precipitated β phase. Equilibrium between the two phases (α and β) is achieved if the chemical potentials of atoms A and B (μ_A and μ_B) are equal in both phases. This condition can be easily illustrated by drawing the common tangent line

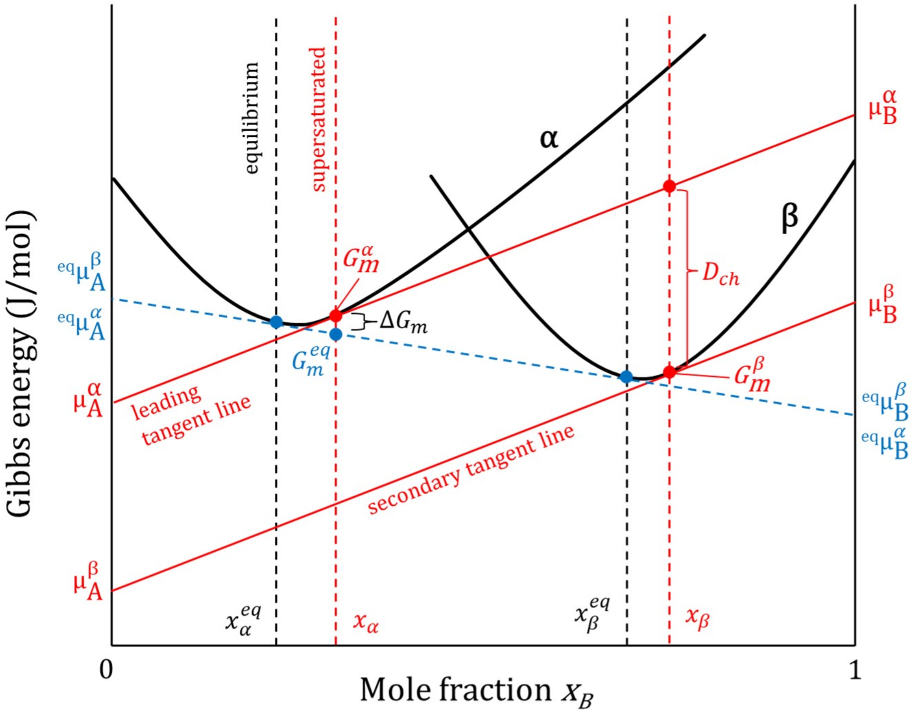

Figure 2.6: Molar Gibbs free energy diagram of β phase precipitation process from supersaturated α phase. The blue dashed line is the common tangent line which indicates the equilibrium composition of both phases. For early precipitation of β phase, a parallel tangent construction is shown as the two red lines, which marks the highest chemical driving force for β formation. Schematic based on Ref [174].

(blue dashed line in Fig 2.6) of the two Gibbs free energy curves. The two intersecting points, marked in blue, represent the equilibrium composition of the two phases, denoted as x_α^{eq} and x_β^{eq}. The total change in Gibbs energy during the process, ΔG_{m}, is given by:

$$\Delta G_{\mathrm{m}} = G_{\mathrm{m}}^{\mathrm{eq}} - G_{\mathrm{m}}^{\alpha} \tag{2.8}$$

here, $G_{\mathrm{m}}^{\mathrm{eq}}$ is the Gibbs energy of the final state (equilibrium), and G_{m}^{α} is the Gibbs energy of the initial stage (α phase with the composition x_α).

Now consider the early stage of phase transformation, when the β phase precipitates directly from the supersaturated α phase with the composition x_β. In this case, the molar Gibbs free energy of β phase is now G_{m}^{β}, and the Gibbs free energy of the initial state is calculated by taking out atoms with the composition x_β from the α phase as $x_\beta\mu_{\mathrm{B}}^{\alpha} + (1 - x_\beta)\mu_{\mathrm{A}}^{\alpha}$. Thus the Gibbs free energy change of the phase transformation is

$$\Delta G_{\mathrm{m}}^{\beta} = G_{\mathrm{m}}^{\beta} - (x_\beta\mu_{\mathrm{B}}^{\alpha} + (1 - x_\beta)\mu_{\mathrm{A}}^{\alpha}) \tag{2.9}$$

The chemical driving force D_{ch} is

$$D_{\mathrm{ch}} = \Delta G_{\mathrm{m}}^{\beta} \tag{2.10}$$

At this point, it is important to know the composition of the β precipitates, x_β. This can be calculated under the assumption that x_β gives the maximum chemical driving force D_{ch}. The value of x_β satisfying this condition can be easily obtained through the parallel tangent construction of the Gibbs energy diagram, as shown in Fig 2.6. The initial Gibbs free energy is obtained by the α curve tangent line (leading tangent line) at the composition x_α. The maximum driving force can be obtained by drawing the β phase tangent line (secondary tangent line) parallel to the α phase tangent line. The composition x_β is determined by the intersecting point of the Gibbs free energy curve of the β phase and the secondary tangent line.

Chapter 3

Materials and methods

3.1 Sample preparation

3.1.1 Preparation and peritectic melting of TiAg

Due to the significant difference in the melting temperature of Ti (1668 °C) and Ag (961.78 °C), cold-crucible induction melting proves to be an efficient method of producing bulk intermetallic compound TiAg, since the fast heating speed leads to simultaneous melting of different components. Ti (>99.99%, ChemPur) pellets and Ag (>99.99%, ChemPur) wires (1 mm in diameter) were melted in a cold copper crucible in an argon atmosphere. The chamber was evacuated and subsequently refilled with argon multiple times to reduce the remaining oxygen. The melting process was also repeated several times to ensure complete melting of all components, particularly the Ti pellets. The sample solidified inside the water-cooled crucible and was then taken out for further processing. The layout of the cold-crucible induction furnace is shown in Fig 3.1 (a).

After melting, the sample was homogenized to obtain a uniform single-phase structure. The homogenization temperature was carefully selected. A high annealing temperature can speed up the homogenization process by increasing the diffusion rate, but the potential risk of remelting due to overshooting of the furnace temperature should also be considered. Taking this into account, the homogenization temperature was set at 630 °C. The sample was heated in a tube furnace under an argon flow for 7 days, then cooled within the furnace. Subsequently, the sample was cut into small cuboids with the size of 1 mm × 1 mm × 2 mm.

Peritectic melting was performed on the cut samples. The samples were placed in a cylindrical stainless steel crucible (internal diameter 1.5 mm) and inserted into the preheated tube furnace set at 1050 °C. After annealing for various durations, the samples were immediately pulled out and quenched directly in room-temperature water to preserve the microstructure obtained at high temperature.

Porous Ti and Ag samples can be produced through chemical corrosion of the peritectic melted samples. To obtain porous Ti, the samples were immersed in 4 M HNO_3 inside a beaker at room temperature, which was then covered with ductile film to minimize evaporation. For porous Ag, the solution was changed to concentrated HCl. The samples

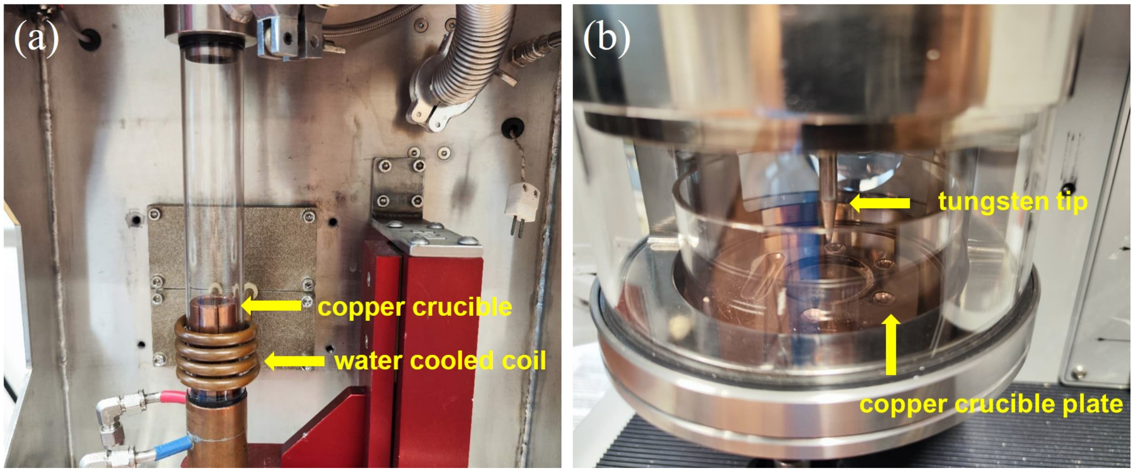

Figure 3.1: Devices used for producing bulk alloys. (a) Cold-crucible induction furnace used to produce TiAg intermetallic compound. Raw materials were melted in argon atmosphere in the copper crucible. (b) Arc melter used for alloys containing low melting point elements. Melting happens on the water cooled copper crucible plate.

were taken out after 5 days to ensure complete removal of the other phase. Then these porous samples were cleaned with ethanol. Throughout the entire corrosion and cleaning processes, these porous samples remain coherent and load-bearing. The fracture surfaces of the porous samples were obtained by breaking the samples with a scalpel.

3.1.2 Preparation and peritectic melting of Ni_3Sn_4

Difficulties were encountered in attempts to produce intermetallic compound Ni_3Sn_4 with the cold-crucible induction furnace. Due to the extremely low melting point ($231.9\,^{\circ}\mathrm{C}$), liquid Sn tends to leak from the copper crucible during solidification. As a result, the samples were produced via arc melting, with raw materials chosen as Ni (>99.99%, ChemPur) wire and Sn (>99.999%, ChemPur) granules. All materials were thoroughly cleaned with acetone and ethanol prior to melting. Similar to induction melting, multiple pumping and venting cycles were conducted to achieve an argon atmosphere with minimal oxygen remain. Figure 3.1 (b) shows the chamber of the arc melter, the melting was done by the electric arc between the tungsten tip and the copper plate. The samples were remelted several times to ensure complete mixing.

Due to equipment limitations, the samples were small in size, with a weight of approximately 2 g. As a result, it was possible to seal the samples in quartz tubes to conduct the homogenization process under vacuum. For intermetallic compound Ni_3Sn_4, the sample was annealed at $700\,^{\circ}\mathrm{C}$ for 7 days, then cooled inside the furnace chamber. Subsequently, these samples were cut into cuboids of the same dimensions as the TiAg samples. Then the Ni_3Sn_4 samples were exposed to conditions of peritectic melting by applying the same

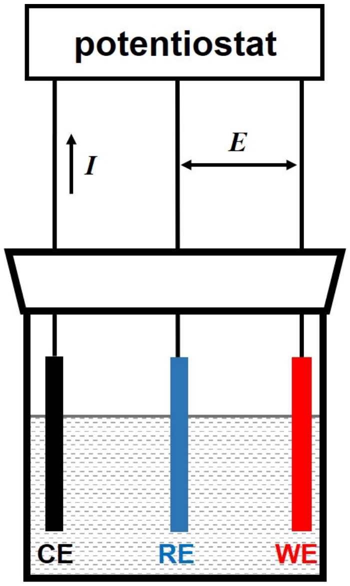

Figure 3.2: Schematic of the three-electrode configuration. Working electrode (WE), reference electrode (RE) and counter electrode (CE) is illustrated in red, blue and black respectively. The potential *E* of the WE is controlled by the potentiostat and the current *I* through the CE is measured.

protocol described in the previous section, but at a different annealing temperature at 820 °C.

Obtaining porous Ni_3Sn_2 has been found to be more challenging than producing porous Ti or Ag, as Ni_3Sn_2 has a relatively high Sn content, making it difficult to separate it from the Sn solid solution. As a result, electrochemical etching was employed instead of chemical etching when producing porous Ni_3Sn_2 samples, using a typical three-electrode configuration, as illustrated in Fig. 3.2. The corrosion process can be precisely controlled through the potentiostat by adjusting the applied electric potential on the working electrode (WE). In this study, electrochemical etching was performed in a beaker sealed with laboratory film. The sample was fixed to a homemade gold clamp, which serves as the WE. A self-made Ag/AgCl electrode served as the reference electrode, which is made according to the protocol described in detail in Ref [177]. A carbon rod was used as the counter electrode. For porous Ni_3Sn_2, the sample was electrochemically etched in 0.5 M H_2SO_4 at -0.6 V. After corrosion, these samples went through the same cleaning protocol as for porous Ti and Ag samples.

3.1.3 Preparation and partial melting of $Cu_{93}In_7$

Cu solid solution with In atoms was selected for partial melting. Cu (>99.995%, ChemPur) plate and In (>99.999%, ChemPur) granules were arc-melted following the same process described above. For homogenization, these samples were annealed in evacuated quartz

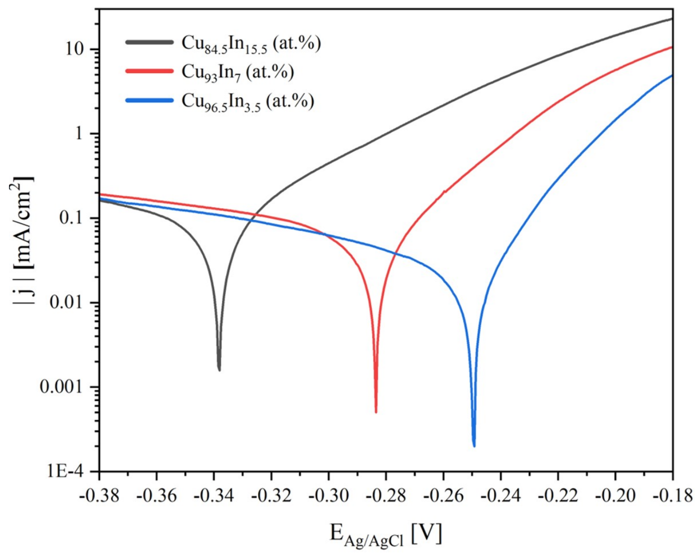

Figure 3.3: Polarization curves of as-homogenized $Cu_{93}In_7$, Cu solid solution phase after partial melting ($Cu_{96.5}In_{3.5}$) and the solidified melt after partial melting ($Cu_{84.5}In_{15.5}$) in 0.5 M H_2SO_4 against a homemade Ag/AgCl electrode.

tubes at 630 °C for 7 days, then quenched in room temperature water. Cuboids with the same dimensions as mentioned before were cut from these samples for partial melting.

The partial melting process is similar to that of peritectic melting, as both involve annealing at high temperature and subsequent quenching. According to the Cu-In phase diagram, the Cu solid solution and the solidified melt have a similar composition, which requires careful control of the corrosion process to selectively remove one phase without etching the other. For that reason, porous Cu solid solution was also produced through electrochemical corrosion, using the same three-electrode configuration as illustrated in Fig 3.2.

Polarization curves were obtained for different phases inside the partial melted samples. After partial melting, the master alloy $Cu_{93}In_7$ decomposed into two phases with the composition $Cu_{84.5}In_{15.5}$ (solidified melt) and $Cu_{96.5}In_{3.5}$ (Cu solid solution). Cu-In samples with corresponding compositions were obtained under the same melting and homogenization protocol as described earlier in this section. Their polarization curves were tested to determine the appropriate etching potential. The Tafel plots are shown in Fig 3.3. The goal is to obtain a porous Cu solid solution by etching out the solidified melt. Based on the polarization curves, the etching was performed in 0.5 M H_2SO_4 at -0.26 V.

3.2 Sample characterization

3.2.1 Microstructure observation

Scanning electron microscopy (SEM, Zeiss Supra VP55) was used to obtain microstructural information of the samples. The microstructure of the cross section and the fracture surface are the primary focuses in this study. For cross-sectional observation, samples were first cold embedded in epoxy, then ground with abrasive papers, following the sequence 320, 600, 1200, 2500, up to 4000 grits. After that, these samples were polished in colloidal silica suspension on a polishing cloth using an automatic polishing machine. After polishing, the surfaces were cleaned first with water, then with ethanol to remove residual silica particles, and then dried with hot air from a hair dryer to prevent watermarks formation on the surface. Since epoxy is not conductive, silver glue and conductive tapes were used to attach the embedded sample to the aluminum SEM holder prior to SEM tests. For fracture surface observation, the sample was fixed to a small SEM holder using conductive tapes and silver glue.

Backscattered electron (BSE) mode was selected for phase distribution observation, as contrast differences arising from variations in chemical composition are more obvious under this mode. Phases containing atoms with higher atomic numbers usually exhibit brighter contrast in BSE images. For observation of the fracture surface, secondary electron (SE) mode is chosen, as it is more sensitive to surface morphology and topography.

3.2.2 Phase identification

X-ray diffraction tests were performed to identify different phases inside the samples. The samples were cut into flat pieces, then ground with sand paper to expose the cross section. The tests were based on Bragg-Brentano X-ray diffraction with Ni-filtered Cu K_α radiation (Bruker D8 Advance), on a rotating sample holder. The diffraction results were analyzed using DIFFRAC.EVA software (BRUKER).

The composition of different areas within the samples can be measured using energy dispersive spectroscopy (EDS) in both SEM and transmission electron microscopy (TEM), then analyzed in AzTec software (Oxford instruments).

3.2.3 Crystallographic orientation

Electron backscatter diffraction (EBSD) provides useful information, including phase distribution, crystallographic orientation, and grain boundary types, all of which contain crucial information for this work. For EBSD tests, cut samples were embedded and polished following the same protocol described previously. After that, the samples were polished again using ion milling to reduce the residual stress induced by mechanical polishing.

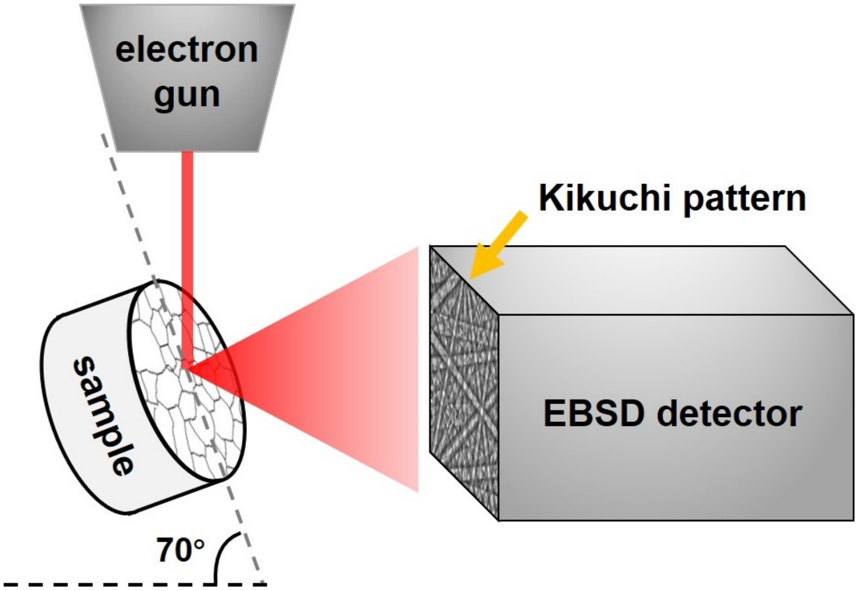

Figure 3.4: Standard electron backscatter diffraction configuration.

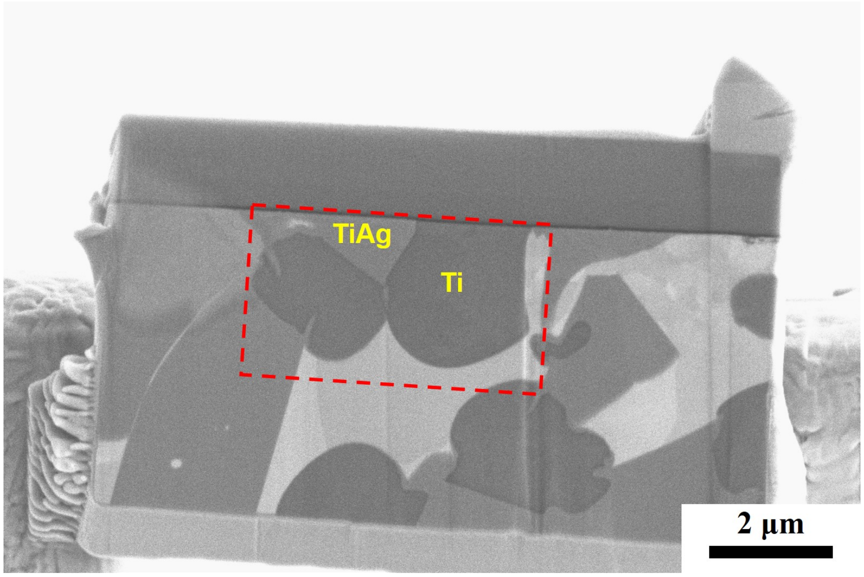

Figure 3.5: Lamella for transmission electron microscopy study, prepared with gallium focus ion beam. The plate was cut from a partially decomposed TiAg sample. The area of interest is indicated by the red rectangle, which contains both TiAg and Ti grains, and Ti/TiAg interfaces.

The standard EBSD configuration is illustrated in Fig 3.4. The electron beam hit the pre-tilted (70 degree) sample, and the backscattered electrons are gather by the detector, forming Kikuchi patterns which contain orientation information of the material. In this work, the beam voltage was set to 15 kV, and the beam current to 1.5 nA. The obtained patterns were then analyzed using AzTec HKL (Oxford instruments) and Channel 5 (HKL Technology, Co.) software.

For an in-depth study of the orientation relationship between the Ti phase and the TiAg phase, a thin lamella was cut from the partially melted TiAg sample using a gallium focus ion beam (FIB, installed in Helios Nanolab G3 UC). The cut plate (10 μm in width, 100 nm thick) is shown in Fig 3.5. After FIB cutting, the sample was transferred to a TEM instrument for further analysis. The red rectangle with dashed lines indicates the area examined by TEM, which contains Ti/TiAg interfaces.

TEM tests were conducted in a Thermo Scientific Talos F200X, equipped with an energy-dispersive X-ray unit. Crystal orientations of both TiAg and Ti grains were studied using selected area electron diffraction (SAED), the obtained patterns from these two grains were indexed and labeled according to standard indexed diffraction patterns. Both the FIB cutting and the TEM observations are conducted by Dr. Tobias Krekeler.

Chapter 4

Peritectic melting of TiAg

In one earlier study [45], a bicontinuous structure containing porous Ti and porous Ag was obtained after peritectic melting of TiAg and was explained as a process similar to liquid metal dealloying. In this chapter, those previous results are verified. Then experiments focusing on the microstructure of the partially decomposed TiAg sample, as well as the orientation relationship between the Ti phase and the TiAg phase, are conducted. Based on the experimental results in this work, a new explanation based on LFM is proposed, which is fundamentally different from the previously suggested dealloying mechanism. The experimental results and images in this chapter have been published in Ref [178].

4.1 Results

4.1.1 Microstructure after peritectic melting

The phase diagram of the Ti-Ag system is shown in Fig 4.1 (a). As indicated by the green dot, the homogenized TiAg sample falls within the single-phase TiAg region. This is further confirmed by the microstructure of the as-homogenized sample given in Fig 4.1 (c), as well as the X-ray diffraction result (black line in Fig 4.2), which shows only the intermetallic compound TiAg peaks [180].

Microstructure of the sample after annealing at $1050\,^{\circ}\mathrm{C}$ for 4 min is shown in Fig 4.1 (b), where two phases can be clearly observed. The two phases were further identified as α-Ti solid solution (denoted as α-Ti only, for simplicity) and Ag solid solution, see the blue line in Fig 4.2. It should be stated here that an overlap exists between diffraction peaks at 2θ =38.1° for (111) Ag and 2θ =38.4° for (002) α-Ti. The peak is labeled as Ag, as it has a larger contribution to the peak intensity. Similarly, the presence of α-Ti will be indicated by its strongest diffraction peak (101) at 40.2°.

Since the element with a higher atomic number shows a brighter contrast under the BSE mode in SEM images, the dark phase in Fig 4.1 (b) is identified as α-Ti and the bright phase corresponds to Ag solid solution. The TiAg phase is not present in the microstructure, indicating that the decomposition of TiAg (reverse peritectic reaction) is complete, and

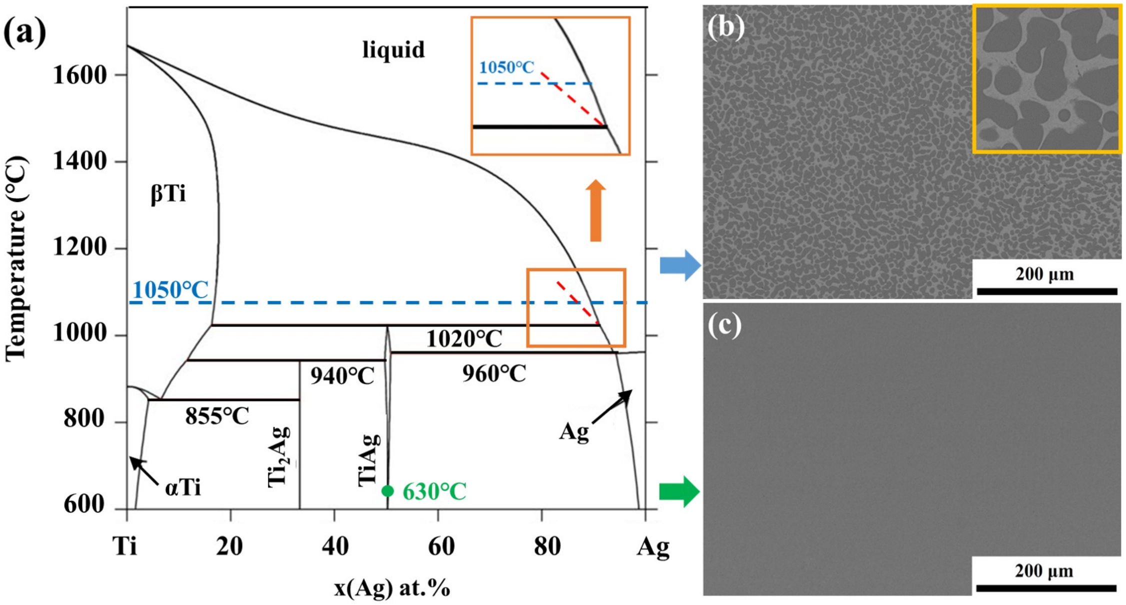

Figure 4.1: Phase diagram of Ti-Ag system and microstructure of samples before and after peritectic melting. (a) Ti-Ag phase diagram, redrawn after [179]. (b) Backscattered electron (BSE) image of a sample heated at 1050 °C for 4 min, with a zoomed in image at the top right corner, which shows clearly a two phase structure. (c) BSE image of an as-homogenized sample, where only one phase can be detected.

the quenching process is fast enough to suppress the peritectic reaction and prevent the formation of TiAg during solidification.

It is important to note that, at the annealing temperature (1050 °C), the equilibrium phases are β-Ti and liquid silver. However, the diffraction results suggest that the quenching process is not fast enough to prevent the phase transformation from β-Ti to α-Ti.

X-ray diffraction results of samples after various heating durations are shown in Fig 4.2. Notably, peritectic melting was not complete after 2 min of annealing at 1050 °C, as the TiAg phase can still be detected (see the red line in Fig 4.2). The decomposition was finished after annealing for 4 min and no new phases were detected after a prolonged heating time for 1 h.

Microstructure of the sample after 60 min of annealing is shown in Fig 4.3, revealing a two-phase structure consisting of α-Ti, which is the solid phase at the annealing temperature, and the Ag solid solution phase, which is the melt at the annealing temperature. While attempts to obtain crystal orientation were unsuccessful, areas exhibiting characteristic features of incompletely wetted grain boundaries are observed (see yellow arrows). This indicates that the Ag melt at the annealing temperature cannot wet all of the α-Ti boundaries.

After peritectic melting, porous Ti and Ag samples can be produced by selective etching in 4 M HNO_3/concentrated HCl respectively. As shown in Fig 4.4 (a) and (b), a porous

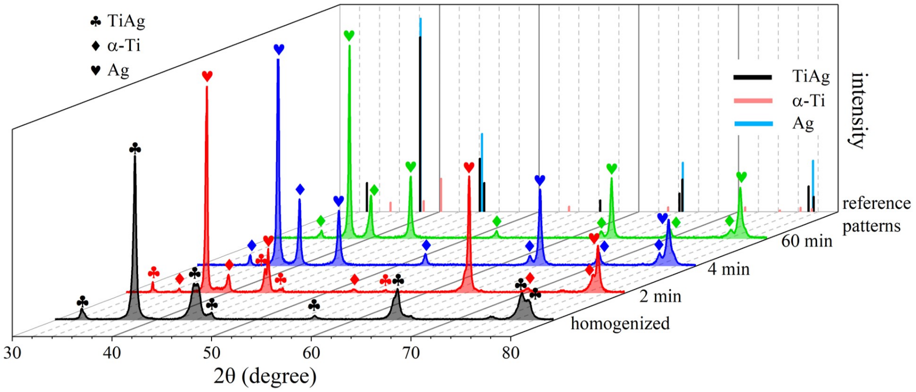

Figure 4.2: X-ray diffraction results of the as-homogenized sample and samples after annealing at $1050\,^{\circ}\mathrm{C}$ for 2, 4 and 60 minutes. Reference peak positions are labeled in different colors. Diffraction peaks of TiAg in the 2 min heated sample suggests that the decomposition is not finished, while the absence of TiAg peaks in 4 min and 60 min samples indicates that the peritectic melting is complete and the two phases remain stable with prolonged heating time.

network of Ti ligaments is left after removal of the Ag phase. Conversely, by removing the Ti phase, porous Ag with an inverted dealloying structure is obtained, see Fig 4.4 (c) and (d). These structures show similarities with samples after LMD [22]. Both porous

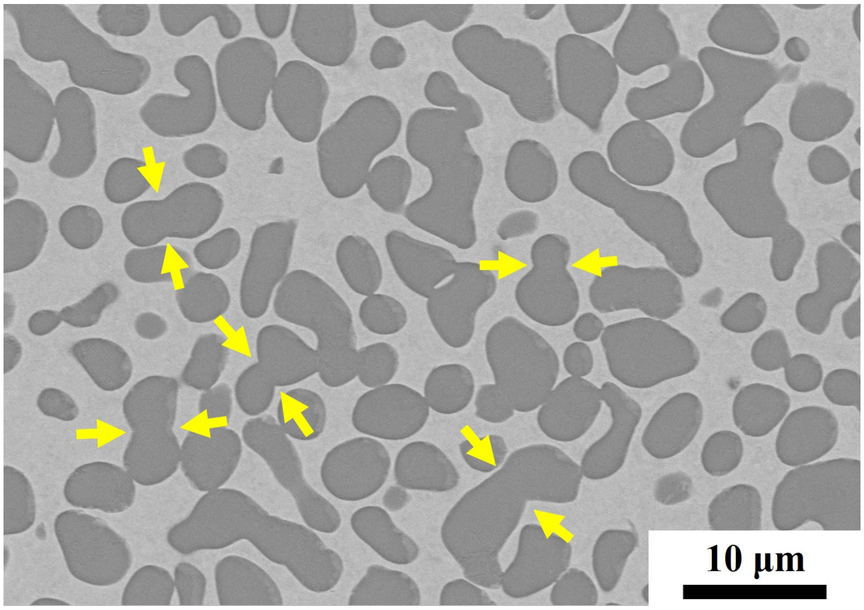

Figure 4.3: Backscattered electron image of the sample after annealing at $1050\,^{\circ}\mathrm{C}$ for 60 min. Areas representing incompletely wetted grain boundaries are indicated by yellow arrows.

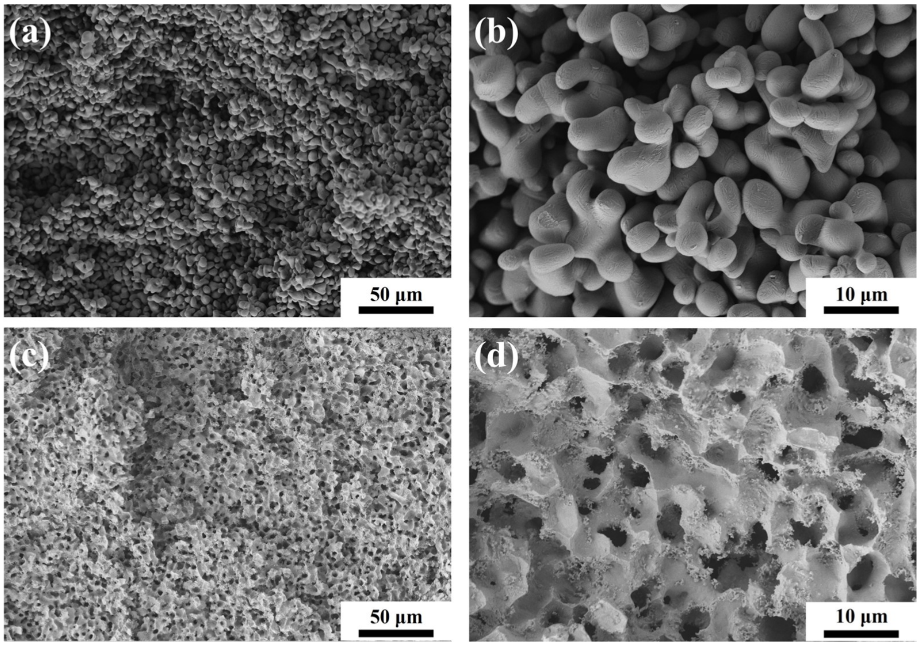

Figure 4.4: Secondary electron images of porous samples. (a,b) Porous Ti obtained after chemical etching in 4 M HNO_3 for 5 days. A network structure with Ti ligaments can be found, which is similar to the typical dealloying structure. (c,d) Porous Ag obtained after chemical etching in concentrated HCl for 5 days, showing an inverted dealloying structure.

samples remain physically stable after etching, showing excellent physical connectivity within the phases. This means that a bicontinuous structure forms after peritectic melting and quenching, supporting the findings reported in Ref [45].

The coarsening effect was also investigated by prolonging the heating duration at the annealing temperature. As shown in Fig 4.5, Ti ligament size increased from around 4 μm after 4 min of heating to approximately 10 μm after 60 min of annealing. The complete removal of the Ag phase in all samples suggests that despite the obvious coarsening, both the Ti and Ag phases remain contiguous and the bicontinuous structure is preserved.

4.1.2 Microstructure of partially decomposed samples

To study the formation mechanism of the bicontinuous microstructure, we annealed the sample at $1050\,^{\circ}\mathrm{C}$ for 2 min to obtain the partially melted microstructure. BSE images of partially decomposed samples are given in Fig 4.6, where three phases can be detected. These phases are identified as Ti (the dark phase), TiAg (the grey phase) and Ag solid solution (the bright phase).

The Ag phase was chemically etched and replaced with epoxy to provide a clearer view of the microstructure, the embedded sample is shown in Fig 4.6 (b). A hemispherical Ti phase is observed to be attached to a TiAg grain by a planar interface. At the opposite

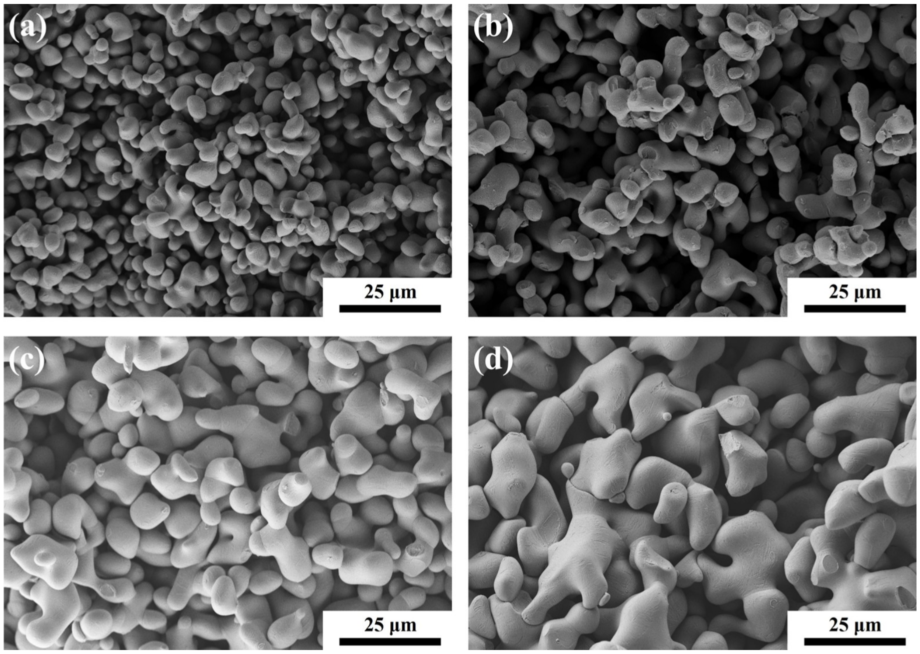

Figure 4.5: Secondary electron images of porous Ti after annealing at 1050 °C for (a) 4 min, (b) 10 min, (c) 20 min, (d) 60 min. The TiAg samples were first heated for various durations, then quenched and chemically removed the Ag phase. Coarsening of Ti ligaments can be observed with prolonged heating time.

TiAg grain, a concave surface is found, and an Ag layer (replaced with epoxy) separates the TiAg grain and the Ti phase.

After chemical etching, the fracture surface of the partially decomposed sample was obtained by breaking the sample with a scalpel. Secondary electron images of the fracture surface are shown in Fig 4.7, containing both the TiAg phase and the Ti phase. SEM-EDX results are listed in Table 4.1, with the identified phases. Structure containing a hemispherical Ti attached to a flat TiAg surface can be observed in areas indicated by yellow arrows, suggesting that it is a general structure during peritectic melting. This observation agrees well with the microstructure of the cross section of the partially decomposed samples shown in Fig 4.6.

Another interesting feature found at the fracture surface is the mushroom-like structure (see Fig 4.7 (b)). It contains several Ti grains attached to a TiAg grain by a narrowed neck of the Ti phase and a trench in the TiAg phase. This peculiar structure usually appears at the triple point during peritectic melting where three phases (Ti, TiAg and liquid Ag) meet.

4.1.3 Structure of the Ti/TiAg interface

As mentioned in the previous section, a newly formed Ti phase attached to a planar TiAg surface can be seen as a general feature during peritectic melting. Therefore, studies on

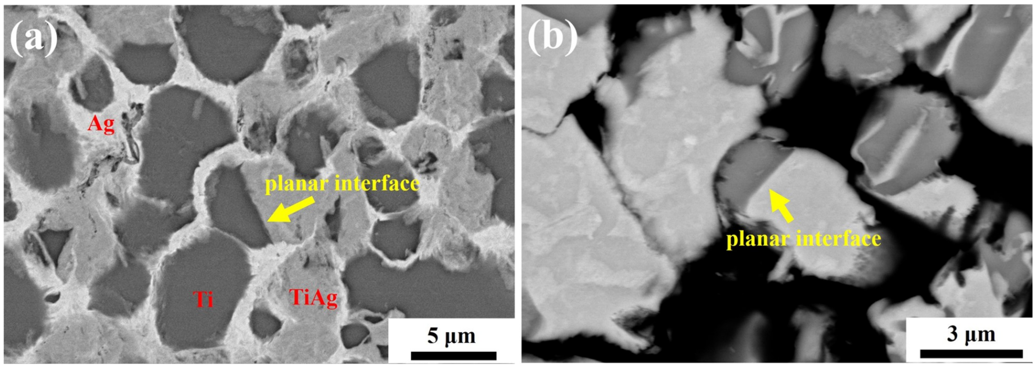

Figure 4.6: Microstructure of partially decomposed samples. (a) Backscattered electron (BSE) image of sample after 2 min annealing. (b) BSE image of the embedded partially decomposed sample, the black area is epoxy which replaces the Ag phase.

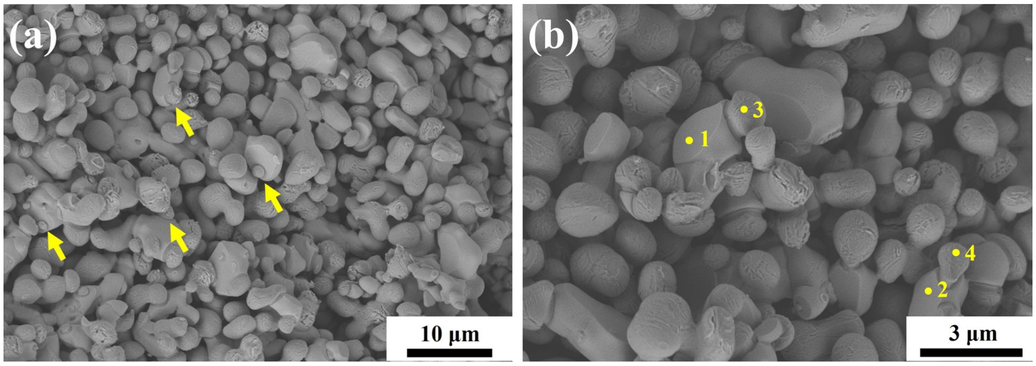

Figure 4.7: Fracture surface of a partially decomposed sample. (a) Secondary electron image of the fracture surface. Yellow arrows point to areas where Ti phase is attached to a planar TiAg surface. (b) Mushroom-like structure observed at the fracture surface. The structure agrees well with backscattered electron images of the cross section.

such Ti/TiAg interfaces can provide valuable insights into the formation mechanism of the Ti phase. For better observation of the interface, we obtained a 100 nm thick lamella (Fig 3.5) with FIB cutting. The selected area is illustrated in Fig 4.8 (a) by the red rectangle.

The high-angle annular dark-field image of the lamella is shown on Fig 4.8 (b), where the interface can be clearly observed. TEM-EDX was performed in area 1 and 2, and the mapping shows that the dark phase on the right (Ti: 80.8 at.%, Ag: 19.2 at.%) is Ti, while the grey phase on the left (Ti: 50.4 at.%, Ag: 49.6 at.%) corresponds to TiAg. These findings are further supported by the element mapping results presented in Fig 4.8 (c,d).

EDX line scan was also conducted on the lamella, which started from the TiAg side, proceeded into the Ti phase, and crossed the interface perpendicularly. From the results shown in Fig 4.8 (e), no obvious composition change is found within the TiAg phase. However, in the Ti phase, the Ag content gradually increases from 9 at.% to 19 at.%, as

Table 4.1: Energy dispersive X-ray spectroscopy results of selected areas in Fig 4.7 (b).

position	Ti (at.%)	Ag (at.%)	phase
1	57.5	42.5	TiAg
2	55.2	44.8	TiAg
3	84.3	15.7	α-Ti
4	84.2	15.8	α-Ti

moving away from the interface.

Crystallographic orientations of the Ti and TiAg phases were also investigated with TEM. In the bright field image of the FIB lamella (see Fig 4.9 (a)), bend contours without disruption can be found, suggesting that the Ti phase is a single grain in the vicinity of the interface. SAED patterns were obtained from both the Ti and TiAg phases (blue and red circles in Fig 4.9 (e)). The labeled diffraction pattern of the Ti grain is given in Fig 4.9 (d), showing a hexagonal close-packed lattice ($P6_3/mmc$), with the electron beam aligned with $[2\bar{1}\bar{1}0]$ zone axis. The diffraction pattern in Fig 4.9 (f) confirms the body-centered structure of the TiAg phase (P4/mmm), with the beam direction along [111].

The two sets of patterns (Fig 4.9 (d,f)) seem to share a common direction. Overlapping spots in two sets of SAED pattern obtained at the interface area can be found in Fig 4.9 (c). The yellow rectangle corresponds to the α-Ti pattern, while the red hexagon represents the TiAg pattern. The overlapping spots are found to be (0002) plane of the α-Ti and $(\bar{1}01)$ plane of the TiAg phase, indicating the parallel relationship between these two planes. This relationship is also observed in the high-resolution TEM image (Fig 4.9 (b)).

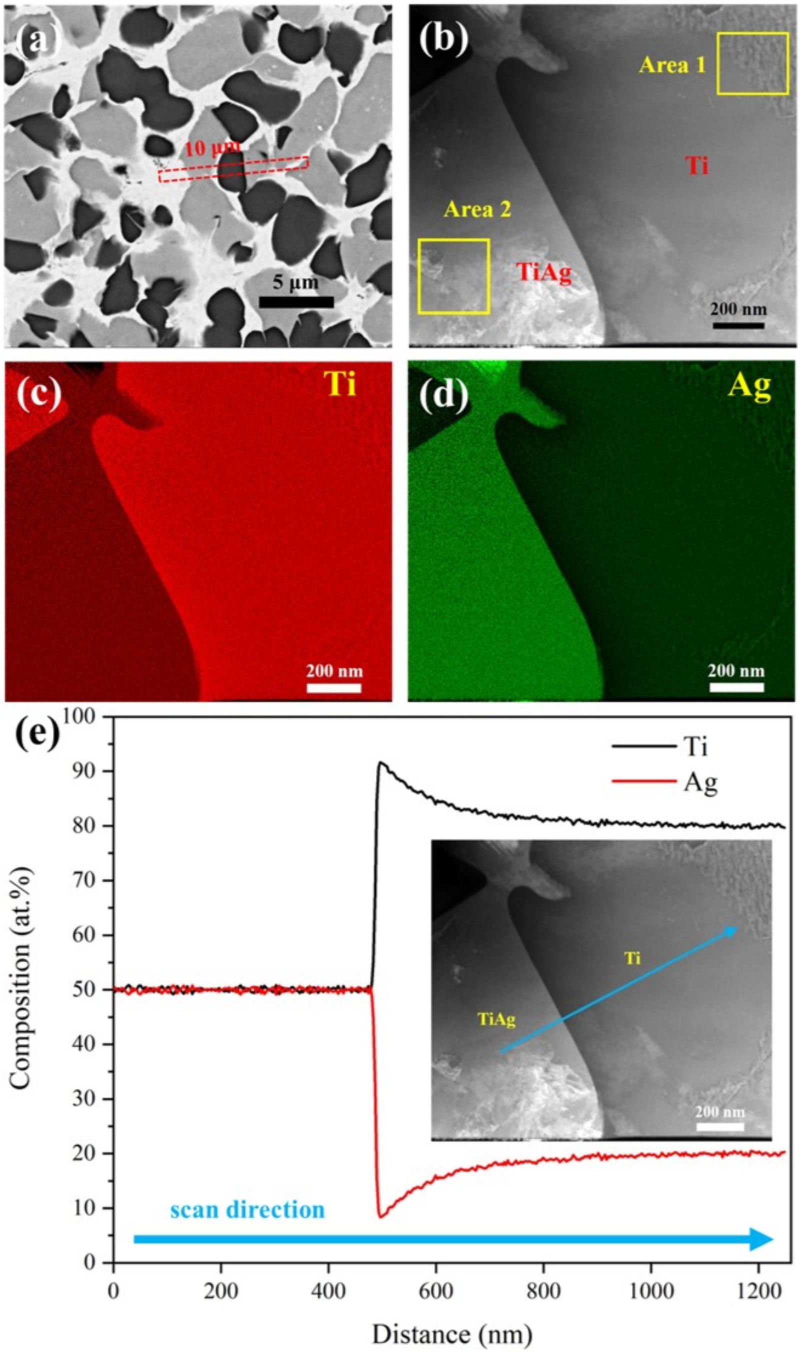

Figure 4.8: Energy dispersive X-ray (EDX) results of the focus ion beam (FIB) cut lamella. (a) Area selected for FIB cutting, the red rectangle shows the position of the lamella. (b) High-angle annular dark-field image of the lamella, showing Ti phase on the right and TiAg phase on the left, the Ti/TiAg interface can be seen clearly. (c,d) EDX mapping of the plate. (e) EDX line scan perpendicular to the interface. The composition remain uniform within TiAg, while a gradient in the Ti phase is found.

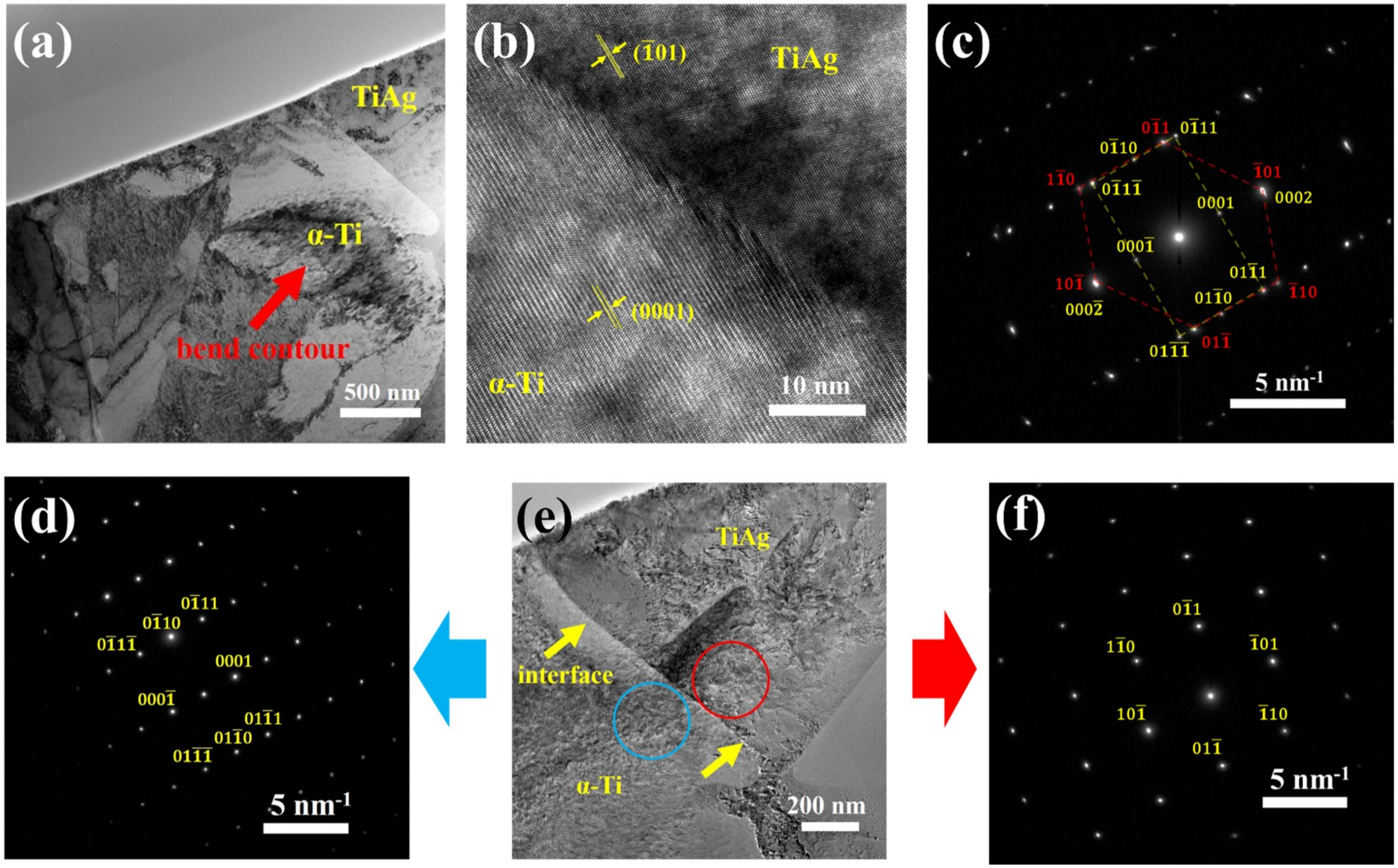

Figure 4.9: Transmission electron microscopy images of the lamella. (a) Bright field image of the plate. Undisturbed bend contour is found inside the sample. (b) High-resolution image at the interface. (c) Selected area electron diffraction (SAED) pattern of the interface area, the overlapping spots in two sets of patterns suggest preferred orientation between the Ti and TiAg grain. (d,e,f) Selected areas for SAED tests and the corresponding pattern of (d) Ti and (f) TiAg phase.

4.2 Discussion

4.2.1 Orientation relationship between the Ti phase and the TiAg phase

SAED patterns of the Ti and TiAg phases (Fig 4.9) have clearly demonstrated the orientation relationship between the two grains as $(0001)_{\alpha-\mathrm{Ti}} \parallel (\bar{1}01)_{\mathrm{TiAg}}$. Schematics of the two lattices at the interface is illustrated in Fig 4.10, based on crystallography data from Ref [180, 181]. The blue hexagon represents the (0001) plane of α-Ti, while the $(\bar{1}01)$ plane of TiAg is shown as the black rectangle, showing a near hexagonal symmetry with only a slight distortion. The mismatch calculated at $[010]_{\mathrm{TiAg}}$ ($[\bar{1}2\bar{1}0]_{\alpha}$) direction is 1.63%, and at $[111]_{\mathrm{TiAg}}$ ($[11\bar{2}0]_{\alpha}$) is 2.03%, indicating a good match in both directions. The low misfit is attributed to the similar atomic radii of Ti (144 pm) and Ag (148 pm), these crystallography data is taken from Ref [181].

It should be noticed that the Ti phase formed at the annealing temperature should be β-Ti, according to the Ti-Ag phase diagram. Thus, the orientation relationship found between α-Ti and TiAg in the quenched sample suggests that such relationship is preserved after phase transformation from β-Ti to α-Ti during quenching. The possible transformation mechanism, known as Burgers orientation relationship [182, 183], is shown in Fig 4.10 (b), which illustrates the orientation relationship between $(0001)_{\alpha}$ and $(\bar{1}01)_{\beta}$ plane. During the quenching process, phase transformation from β-Ti to α-Ti could follow the Burgers orientation relationship as: $(\bar{1}01)_{\beta} \parallel (0001)_{\alpha}$, and the orientation relationship at the annealing temperature can be inferred as $(\bar{1}01)_{\beta} \parallel (\bar{1}01)_{\mathrm{TiAg}}$.

A similar transformation mechanism was observed during quenching of Ti-Cu eutectics [184]. During annealing, Ti_2Cu forms from the β-Ti matrix, with the orientation relationship as $(110)_{\beta} \parallel (103)_{\mathrm{Ti_2Cu}}$. In the subsequent quenching process, phase transformation from β-Ti to α-Ti follows the Burgers orientation relationship and forms a new lattice correspondence as $(0001)_{\alpha} \parallel (103)_{\mathrm{Ti_2Cu}}$.

Due to the low lattice misfit at the Ti/TiAg interface, a low interfacial energy is expected, which favors the heterogeneous nucleation of the Ti phase on the TiAg/melt interface. As a result, Ti phase attached to the TiAg grains with a planar interface can easily be found in partially decomposed samples.

4.2.2 Contradictions between the dealloying mechanism and the experimental observation

In a previous study [45], peritectic melting of TiAg was speculated to proceed through a dealloying-like mechanism, since the final bicontinuous structure closely resembled that of LMD products. However, conflicts between the dealloying mechanism and the experimental results obtained in this study are found. In this section, we introduce the previously proposed dealloying-like mechanism and highlight the contradiction with our observation.

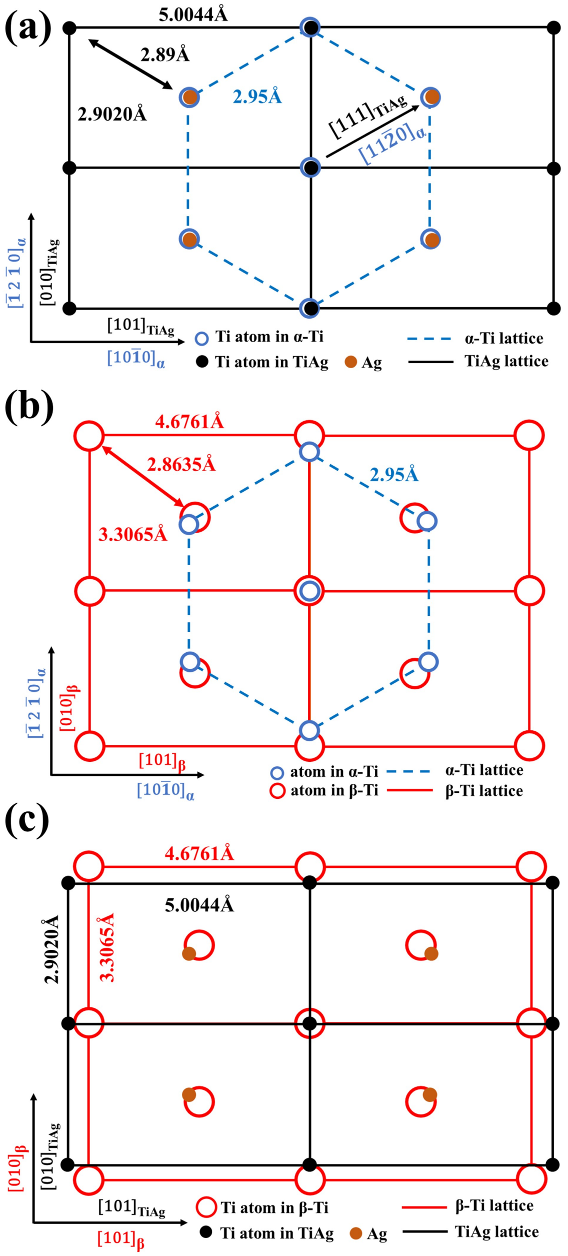

Figure 4.10: Orientation relationship between TiAg, α-Ti and β-Ti. (a) Schematic of the observed orientation relationship between $(0001)_\alpha$ and $(\bar{1}01)_{TiAg}$. Low mismatch is found between the two planes in both $[010]_{\mathrm{TiAg}}$ ($[\bar{1}2\bar{1}0]_\alpha$) direction and $[111]_{\mathrm{TiAg}}$ ($[11\bar{2}0]_\alpha$) direction. (b) One possible type of Burgers orientation relationship between β-Ti and α-Ti during phase transformation, known as $(\bar{1}01)_\beta \parallel (0001)_\alpha$. (c) Possible lattice correspondence between β-Ti and TiAg at the annealing temperature as $(\bar{1}01)_\beta \parallel (\bar{1}01)_{\mathrm{TiAg}}$.

Microstructure evolution during LMD has been discussed in detail in Chapter 2. A schematic illustrating the dealloying mechanism of TiAg is shown in Fig 4.11. At the initial stage of peritectic melting, the grain boundary between the two TiAg grains is wetted and separated by a liquid Ag layer. As decomposition progresses, Ag atoms at the wetted surfaces diffuse into the melt (see red arrows), while the remaining Ti atoms form ligaments through surface diffusion (black arrows) at the dealloying fronts. Similar to the LMD process, decomposition of TiAg also goes from the grain boundaries to the center of the TiAg grains, and the newly formed Ti ligaments are always attached to the parent phase.

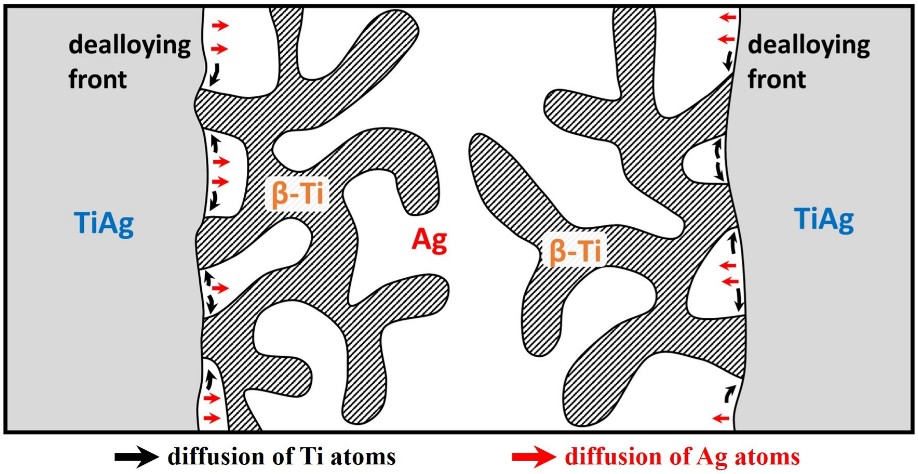

Figure 4.11: Schematic of the incorrect dealloying-like mechanism. During decomposition of TiAg, Ag atoms at the dealloying front diffuse into the melt, and Ti atoms reorganize into ligaments through surface diffusion.

The dealloying mechanism is enough to explain the obtained bicontinuous structure; however, some of the experimental results in this study conflict with this theory. First, as the dealloying process proceeds into the TiAg grains, the Ti/TiAg interface at the dealloying front should also migrate in the same direction. However, a fast migration mechanism of the planar Ti/TiAg interface has yet to be proposed. Furthermore, the characteristic feature of the planar Ti/TiAg interface can not be a natural consequence of the dealloying mechanism. At the dealloying front, Ag atoms from areas that are not covered by the Ti phase can diffuse directly into the melt through surface diffusion, while at the interface, these atoms have to go through bulk diffusion or interface diffusion, which is significantly slower. As a result, it would be difficult to maintain a planar interface during peritectic melting if the dealloying mechanism were active.

Apart from the microstructure side, the composition gradient in the newly formed Ti phase (Fig 4.8 (e)) is also difficult to explain as a consequence of dealloying. Normally, in other dealloying processes, the fraction of sacrificial elements is higher at the dealloying front, compared to the external surface [37, 185, 186]. In this study, Ti/TiAg is equivalent to the dealloying front, and an inverse composition gradient was detected in the Ti phase, as Ag composition (sacrificial element in this study) increased as moving away from the Ti/TiAg interface. This is not compatible with the dealloying mechanism.

4.2.3 Peritectic melting through liquid film migration

The previously mentioned dealloying mechanism has difficulties in explaining our experimental results. As an alternative, we propose the liquid film migration mechanism. As illustrated in Fig 4.12 (a), the first step of peritectic melting is here also the wetting of the TiAg grain boundaries. A constrained (no Ti phase) equilibrium exists between the melt and the TiAg phase, represented by the red dashed line as the extension of the TiAg liquidus in Fig 4.1 (a).

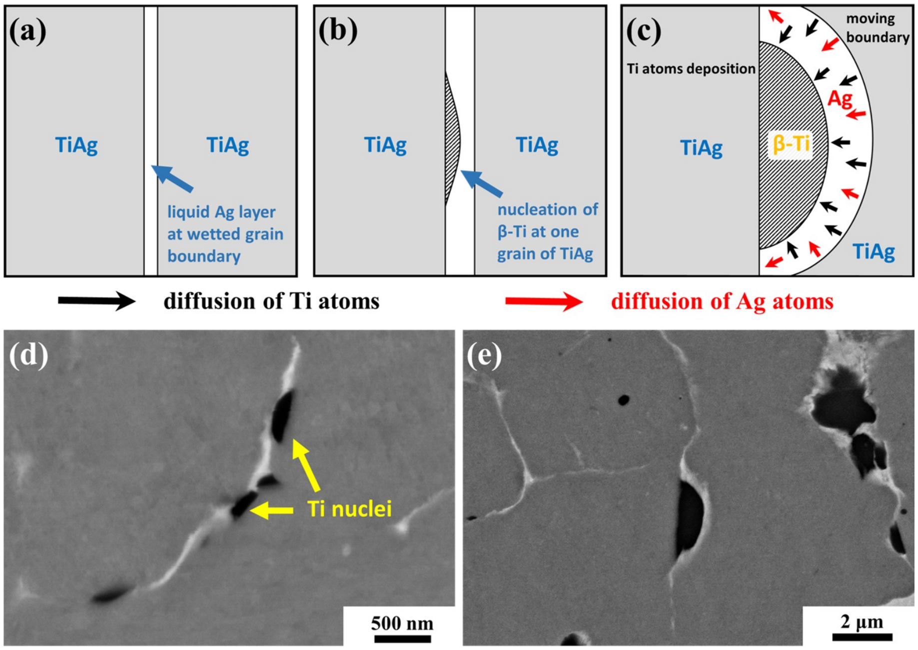

Figure 4.12: Schematics of the liquid film migration (LFM) mechanism. (a) Grain boundary wetting at the beginning of peritectic melting. (b) Heterogeneous nucleation on TiAg surface. (c) Decomposition of TiAg and growth of β-Ti through LFM mechanism. Red and black arrows represent the diffusion of Ag and Ti atoms. (d) Backscattered electron (BSE) image of Ti nuclei (yellow arrows) forming at a wetted grain boundary in partially decomposed sample. (e) BSE image of the hemisphere shaped Ti phase corresponding with the schematic in (c).

After the two grains are separated by the melt, the Ti phase will nucleate. The preferred orientation relationship between the Ti phase and the TiAg phase, as detected in this research, results in a low interface energy between the two phases. This lattice correspondence lowers the nucleation barrier and makes the wetted TiAg surface an ideal position for heterogeneous nucleation of the Ti phase. The corresponding microstructure is observed in partially decomposed samples, shown in Fig 4.12 (d).

The decomposition of the TiAg phase begins after nucleation of the Ti phase. Both Ti and Ag atoms at the melt/TiAg surface diffuse into the melt, then deposit on the Ti nuclei across the liquid layer. The surplus Ag atoms remain in the melt, thickening the liquid layer if they are not channeled to nearby intergranular areas. The migration of the liquid layer stops when the TiAg grain is completely decomposed. A possible intermediate state is illustrated in Fig 4.12 (c), characterized by a hemispherical Ti phase and the TiAg grain with a concave surface. This structure is clearly observed in Fig 4.12 (e) in the partially decomposed sample.

Another characteristic feature in the partially decomposed sample is the mushroom structure, see Fig 4.13. The structure resembles the product of melting along the interface between two solid phases, which is numerically studied with phase field simulation [106, 107]. A schematic of this local melting mechanism is presented in Fig 4.13 (a). As melting progresses along the Ti/TiAg interface, TiAg decomposes, and the Ti phase grows through a local LFM mechanism, forming two parabolic interfaces, creating the mushroom structure shown in Fig 4.13 (b).

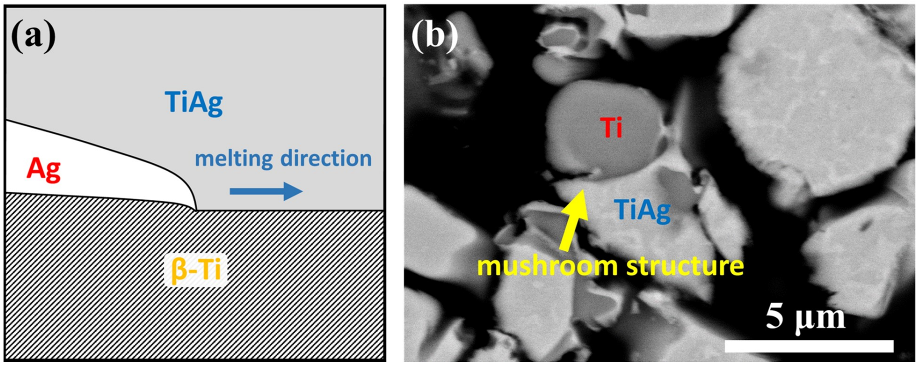

Figure 4.13: Melting along the β-Ti/TiAg interface. (a) Schematic of TiAg dissolution and Ti deposition based on phase field simulation from [107]. (b) Backscattered electron image of the mushroom-like structure found in partially decomposed sample.

The composition gradient within the Ti phase is also compatible with the LFM mechanism. The molar Gibbs free energy curve of the TiAg, Ti and Ag phase is illustrated in Fig 4.14. At the initial stage of peritectic melting, before the decomposition of TiAg, the TiAg grains are in a constrained equilibrium (no Ti phase) with the melt, and the composition of the melt is determined by the TiAg/Ti common tangent. As can be seen, the melt is supersaturated with Ti atoms. Subsequently, β-Ti phase will nucleate at the wetted TiAg grain boundaries, which is a similar process as precipitation from the supersaturated melt. As a result, the composition of the nuclei can be obtained from the parallel tangent construction discussed in Chapter 2. Compared to the equilibrium composition of the Ti phase at the annealing temperature (the grey point on the Ti curve), the composition indicated by the secondary tangent line, $x_{\beta-\mathrm{Ti}}$, suggests a lower Ag content in initial Ti nuclei, exactly as we observed. As the Ti phase grows, the melt will be less supersaturated, causing the Ag content in the Ti phase to increase, eventually approaching the equilibrium composition $x^{\mathrm{eq}}_{\beta-\mathrm{Ti}}$.

With the formation mechanism explained, it is important to understand how it eventually leads to a bicontinuous structure. The connectivity of the Ti phase comes from incompletely wetted grain boundaries, which can be seen in Fig 4.3. While for the Ag phase, the wetted boundaries at the annealing temperature form a connected network automatically. In fact, a similar case has been studied in partial melting of Cu-In [138] alloy, which will be discussed in detail in Chapter 6.

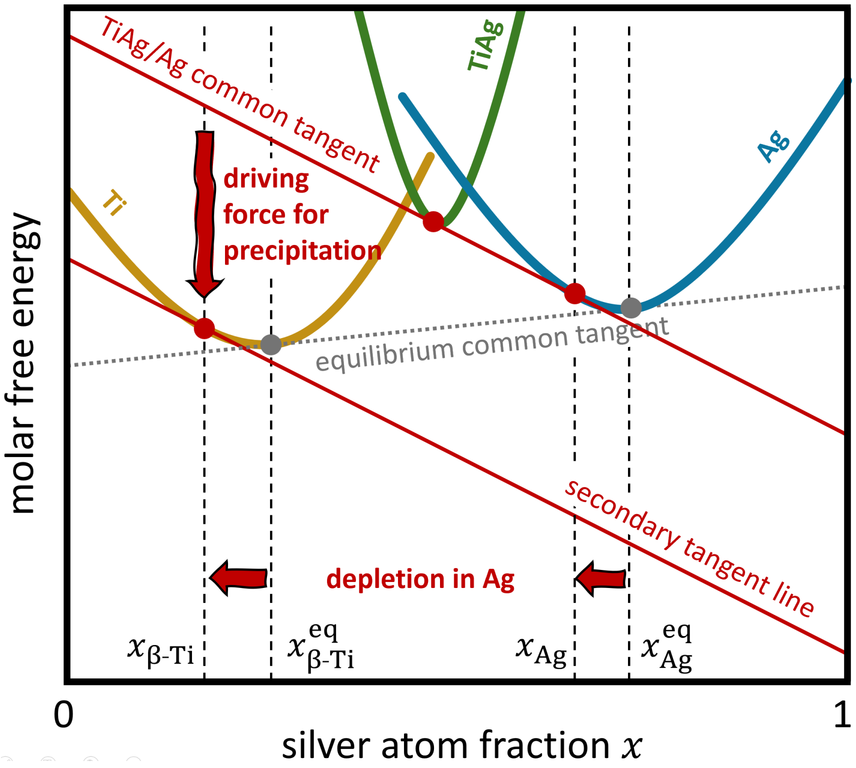

Figure 4.14: Schematic of parallel tangent construction analysis of the Gibbs energy curve of TiAg, Ti and Ag phase. The composition of the Ti nuclei is decided by the intersection point of the Ti Gibbs energy curve and the secondary tangent line as $x_{\beta-\mathrm{Ti}}$. Compared to the equilibrium composition obtained from the common tangent, Ti nuclei is depleted in Ag.

Chapter 5

Peritectic melting of Ni_3Sn_4

In the previous chapter, the mechanism of bicontinuous structure formation during peritectic melting of TiAg is explained through the LFM mechanism. In this chapter, peritectic melting of Ni_3Sn_4 is studied, and a distinct microstructure containing clusters of Ni_3Sn_2 cells is obtained. Based on EBSD studies, the peculiar microstructure comes from homogeneous nucleation and cellular growth of the Ni_3Sn_2 phase. This chapter provides another example of LFM during peritectic melting with a distinct nucleation and growth mechanism, and shows that the final microstructure can be affected by several factors, including annealing temperature, grain size of the master alloy, and the nucleus density of the new solid phase. The experimental results and images in this chapter have been published in Ref [187].

5.1 Results

5.1.1 Microstructure after peritectic melting

The phase diagram of the Ni-Sn system is shown in Fig 5.1 (a). The peritectic line can be found at 798 °C. Above this temperature, a reverse peritectic reaction occurs as: $Ni_3Sn_4 \rightarrow Ni_3Sn_2$ HT + Liquid. In this work, all Ni_3Sn_2 phases will be referred to as Ni_3Sn_2 for simplicity. The red spot shows the homogenization condition, which falls into the single phase Ni_3Sn_4 region. The microstructure of the homogenized sample is shown in Fig 5.1 (b) and (c). Apart from large pores (black areas in panel (c)) that form during solidification after arc melting, mainly Ni_3Sn_4 phase with a grey contrast can be found, together with small amount of extra Sn phase at grain boundaries and triple points.

EBSD test was also conducted on the homogenized sample. As can be seen in Fig 5.2 , large Ni_3Sn_4 grains, approximately 150 μm in size, can be observed, and no obvious texture can be detected from the inverse pole figure.

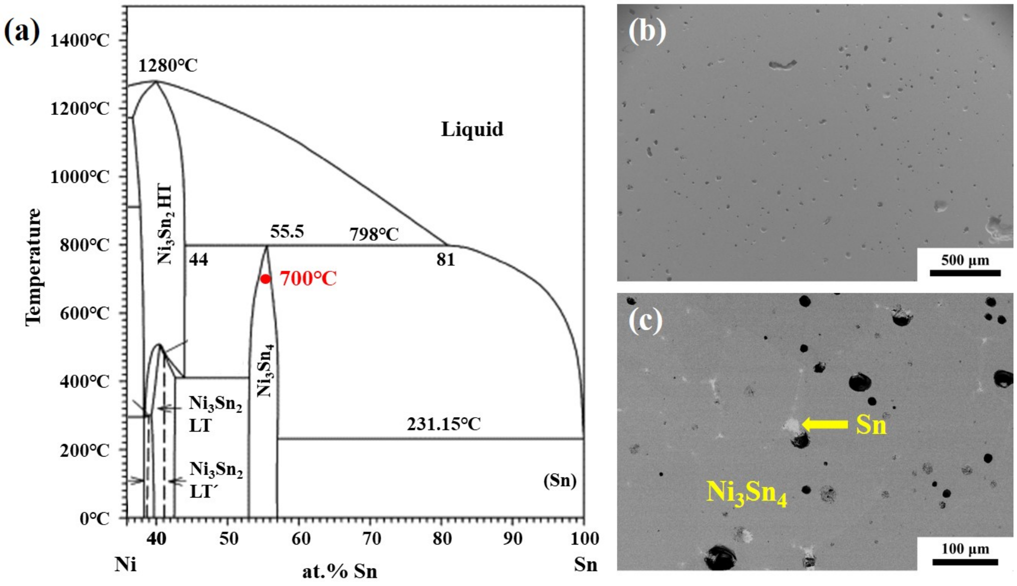

Figure 5.1: Microstructure of the homogenized sample. (a) Phase diagram of the Ni-Sn system, redrawn after [188]. The red spot shows the state of the homogenized sample. (b) Secondary electron image of a homogenized sample, pores formed during arc melting can be found. (c) Backscattered electron image of a homogenized sample. Extra amount of Sn (bright phase) can be found at grain boundaries and triple points of Ni_3Sn_4 (grey phase) grains. Areas with black contrast are casting pores.

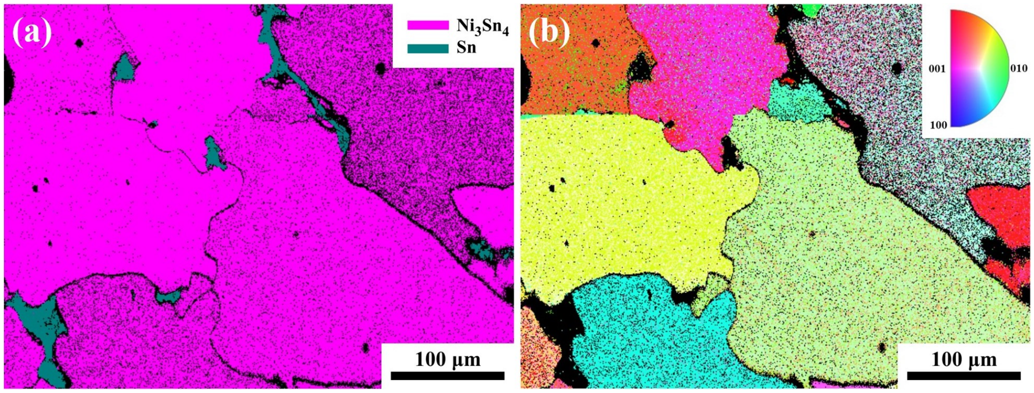

Figure 5.2: Electron backscatter diffraction results of the homogenized sample. (a) Phase identification. (b) Inverse pole figure of the Ni_3Sn_4 phase only.

The microstructure of peritectic melted samples is shown in Fig 5.3. After annealing at 820 °C for 40 s, clusters of Ni_3Sn_2 ligaments are observed. Based on the EDS results (see table 5.1) of pointed areas in Fig 5.3 (b), the dark phase with a ligament structure is identified as Ni_3Sn_2, with Ni_3Sn_4 phase covering the surface of the ligaments. The bright phase corresponds to Sn solid solution containing approximately 2.4 at.% Ni. Different contrast between Ni_3Sn_2 clusters are attributed to the difference in their crystal orientations.

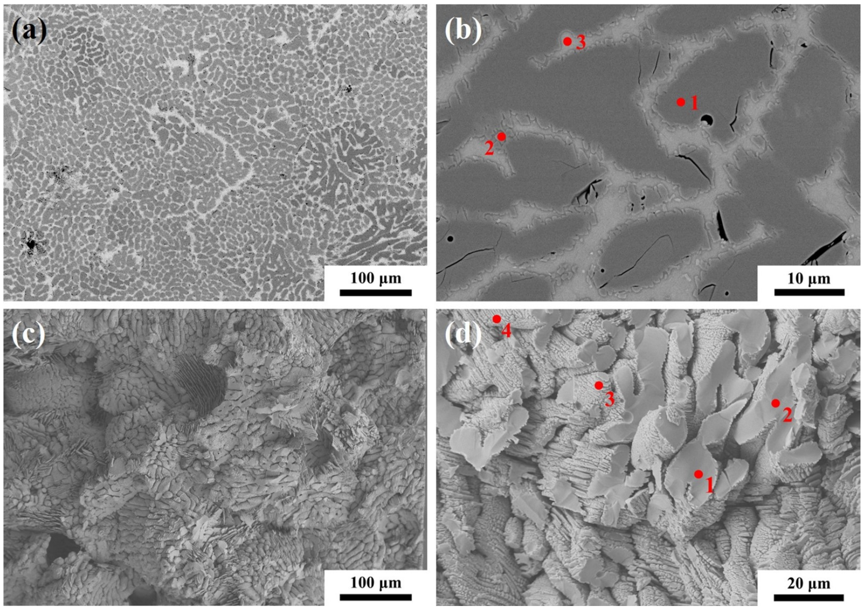

Figure 5.3: Microstructure of the sample after peritectic melting. (a,b) Backscattered electron images of the polished cross section. Clusters of ligaments with a dark contrast can be observed, which is the Ni_3Sn_2 phase. The bright phase is Sn solid solution. A closer look reveals Ni_3Sn_4 phase covering Ni_3Sn_4 ligaments. (c,d) Secondary electron images of the fracture surface, after removal of the Sn phase.

Table 5.1: EDS results of the sample cross section in Fig 5.3 (b)

position	Ni (at.%)	Sn (at.%)	phase
1	54.7	45.3	Ni_3Sn_2
2	43.1	56.9	Ni_3Sn_4
3	2.4	97.6	Sn solid solution

For clear observation of the ligaments, the Sn solid solution phase can be removed by electrochemical etching at -0.6 V in 0.5 M H_2SO_4, against a self-made Ag/AgCl electrode. By breaking the sample with a scalpel, the fracture surface of the peritectic melted sample is revealed, as shown in Fig 5.3 (c) and (d). Features corresponding to pores remain evident. A closer look at the fracture surface (Fig 5.3 (d)) provides a clearer view of the Ni_3Sn_2

ligaments and the covering Ni_3Sn_4 phase. EDS analysis of the ligaments (Table 5.2) is consistent with previous tests in Fig 5.3 (b).

Table 5.2: Composition of center and surface areas of the ligaments in Fig 5.3 (d)

position	Ni (at.%)	Sn (at.%)	phase
1	55.4	44.6	Ni_3Sn_2
2	53.5	46.5	Ni_3Sn_2
3	44.0	56.0	Ni_3Sn_4
4	45.2	54.8	Ni_3Sn_4

The EBSD results of the peritectic melted sample, shown in Fig 5.4, provide interesting insights into the phase distribution and connectivity of Ni_3Sn_2 ligaments. The phase map shown in Fig 5.4 (a) suggests that the ligaments are all Ni_3Sn_2 phase, with the Sn phase filling the gaps between the ligaments, which is consistent with our previous observation. The Ni_3Sn_4 phase is too small to be identified. The inverse pole figure (Fig 5.4 (b)) of Ni_3Sn_2 reveals distinct crystal orientations between different clusters. However, within a given cluster, the orientation of different ligaments remains consistent. This indicates that these ligaments are interconnected, despite seemingly being separated in 2D images. It should also be noted that the cluster size is close to the original Ni_3Sn_4 grain size, which is significantly larger than the ligament size.

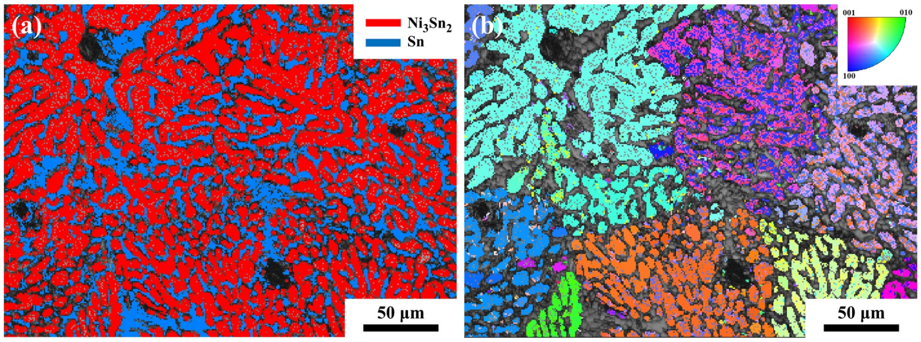

Figure 5.4: Electron backscatter diffraction result of the sample after annealing at 820 °C for 40 s. (a) Phase distribution of Ni_3Sn_2 and Sn phase at the cross section. Ni_3Sn_4 phase is not shown due to the small size. (b) Inverse pole figure of Ni_3Sn_2 phase. Different orientations are found among clusters, but the same orientation is found for ligaments within the same cluster.

5.1.2 Effect of the annealing temperature on the microstructure

Peritectic melting of Ni_3Sn_4 was also conducted at 1000 °C. In order to mitigate the coarsening effect, samples were annealed for various durations, then immediately quenched in water to preserve the microstructure. After multiple tests, it was found that peritectic melting of Ni_3Sn_4 can be finished after annealing at $820\,^\circ$C for 20 s or at $1000\,^\circ$C for 3 s. The corresponding microstructures are shown in Fig 5.5 (a) and (b), respectively. Both samples exhibit a similar structure consisting of clusters of ligaments. However, for the sample after annealing at $820\,^\circ$C, the ligament size is measured to be approximately 4.6 μm, which is significantly larger than that of the sample heated at $1000\,^\circ$C, with a ligament size of 2.1 μm. This is a counterintuitive result, as higher temperatures typically yield coarser structures.

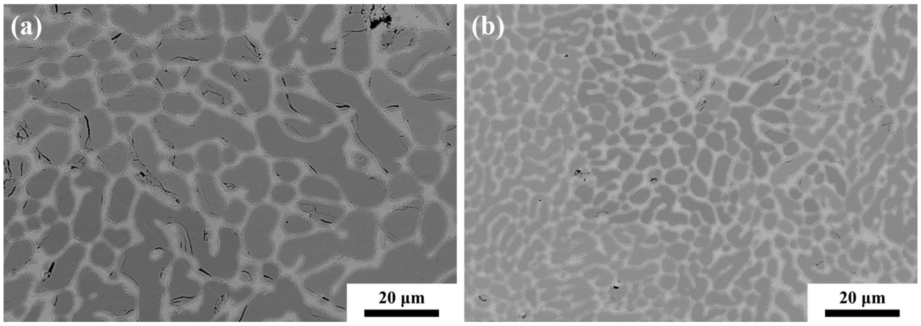

Figure 5.5: Backscattered electron images of samples annealed at (a) $820\,^\circ$C for 20 s, and (b) $1000\,^\circ$C for 3 s. Both images show a ligament structure right after complete decomposition. The ligament size is obviously larger in the sample annealed at the lower temperature.

5.1.3 Microstructure of partially decomposed samples

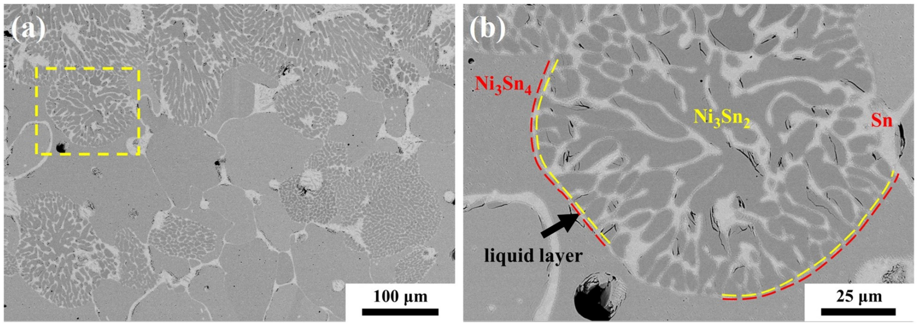

Figure 5.6: Backscattered electron image of a partially decomposed sample after annealing at $820\,^\circ$C for 15 s. Three phases can be found including Ni_3Sn_2, Sn and undecomposed Ni_3Sn_4 grains. The solidification front of Ni_3Sn_2 and melting front of Ni_3Sn_4 are shown as the yellow and red dashed line respectively. Both dashed lines are broken for visibility of the Sn layer which separates the two fronts.

To further investigate the formation mechanism of the ligament structure, partially decomposed samples were obtained after annealing at $820\,^\circ$C for 15 s, as shown in Fig 5.6.

In addition to Ni_3Sn_2 and Sn, undecomposed Ni_3Sn_4 grains are also detected at the cross section. An enlarged image of the area marked by the yellow rectangle in is given as Fig 5.6 (b). A spherical cluster of Ni_3Sn_2 is observed, with the periphery outlined in yellow. Notably, the center of the cluster exhibits a larger ligament size compared to the ligaments at the outer regions. Against the cluster, an undecomposed Ni_3Sn_4 grain can be found with a concave surface marked by the red dashed line, and a Sn layer is found in-between.

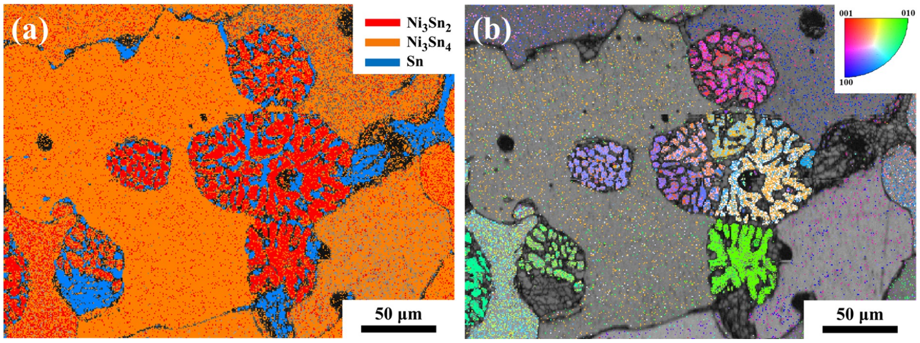

Figure 5.7: Electron backscatter diffraction result of a partially decomposed sample. (a) phase distribution of three phases including Ni_3Sn_4, Ni_3Sn_2 and Sn. (b) Inverse pole figure of the Ni_3Sn_2 phase only.

EBSD analysis of the partially decomposed sample provides additional structural information, as can be seen in Fig 5.7. Obviously, multiple clusters can form within the same grain boundary area, and different orientations can be observed.

5.2 Discussion

5.2.1 Nucleation and liquid film migration

As discussed in the previous chapter, peritectic melting of TiAg follows the LFM mechanism, that is, complete decomposition of TiAg and deposition as β-Ti at the opposite grain, achieved by diffusion across the liquid layer. In fact, during peritectic melting of Ni_3Sn_4, characteristic features of LFM can also be observed in the partially decomposed sample in Fig 5.6, including the convex envelope of Ni_3Sn_2 clusters which is their growth front, the concave surface of the opposite Ni_3Sn_4 grain which is the melting front, and a Sn layer between the two phases. This suggests that peritectic melting of Ni_3Sn_4 also operates through the LFM mechanism, similar to TiAg. However, the resulting structure is rather different.

One significant difference between the two alloy systems is that during the decomposition of TiAg, planar TiAg/Ti interfaces are observed, which forms during heterogeneous nucleation of β-Ti on the wetted TiAg grain boundary. Such interfaces are not found in the partially decomposed Ni_3Sn_4 samples. Instead, judging by the partially decomposed microstructure (see Fig 5.6 and Fig 5.7), the newly formed Ni_3Sn_2 phase is separated from nearby Ni_3Sn_4 grains by a Sn layer in every direction. As a result, instead of the hemisphere-shaped product phase (β-Ti) observed in partially decomposed TiAg samples, the growing Ni_3Sn_2 clusters all have a spherical or ellipsoidal shape. The above observations indicate that during peritectic melting of Ni_3Sn_4, new Ni_3Sn_2 phase forms by homogeneous nucleation within the melt.

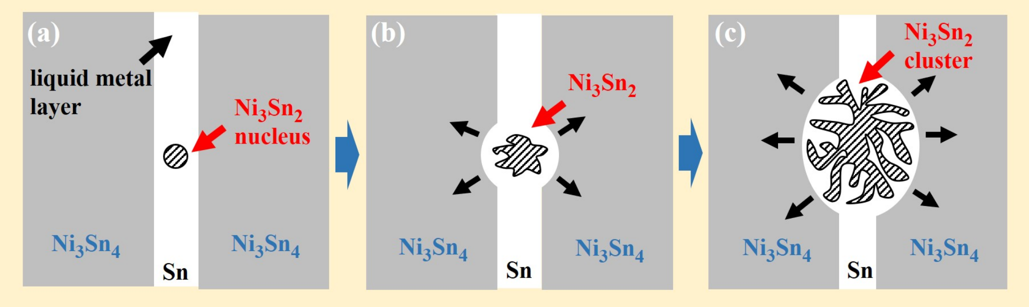

Figure 5.8: Schematic of nucleation and growth mechanism during peritectic melting of Ni_3Sn_4. (a) Homogeneous nucleation of Ni_3Sn_2 inside the melt. (b) Growth of a Ni_3Sn_2 nucleus in all direction, at the expense of Ni_3Sn_4, following the liquid film migration mechanism. (c) Formation of spherical cluster of Ni_3Sn_2 ligaments

The nucleation and growth processes of Ni_3Sn_2 are illustrated in Fig 5.8. Similar to the case of TiAg, the initial stage of peritectic melting of Ni_3Sn_4 is also grain boundary wetting. A liquid Sn layer will form and separate Ni_3Sn_4 grains before decomposition of Ni_3Sn_4 happens. Following this, Ni_3Sn_2 nucleates from the liquid layer through homogeneous nucleation, as illustrated in panel (a) of Fig 5.8. The growth of Ni_3Sn_2 nucleus, without a preferred direction, is coupled with decomposition of Ni_3Sn_4 grains, following the LFM mechanism, as shown in panel (b). It eventually grows into a spherical or ellipsoidal cluster with a cellular structure, shown in panel (c). Reasons for the cellular growth of Ni_3Sn_2 will be discussed in the next section.

It should be noted that in these Ni_3Sn_2 clusters, the ligament is coarser in the central area (see Fig 5.6 (b)). As shown in Fig 5.8, ligaments at the center of the cluster form earlier and have a longer coarsening time, resulting in a larger ligament size. This is another evidence of homogeneous nucleation of Ni_3Sn_2 during peritectic melting.

5.2.2 Growth mechanism of Ni_3Sn_2

In the previous section, the homogeneous nucleation mechanism of Ni_3Sn_2 was introduced, which explains the spherical shape of the Ni_3Sn_2 clusters. In this section, the origin of the cellular growth of Ni_3Sn_2 will be explained. For conciseness, the Ni_3Sn_2 phase will be denoted as α, the Ni_3Sn_4 phase as β and the melt as L.

During reverse peritectic reaction, the β phase will decompose into α and L. This requires phase partitioning at the growth front, which is done through lateral diffusion within the liquid layer. An analogy of the phase partitioning process will be eutectic solidification, which results in a cellular structure. For the lateral diffusion speed at the growth front to be sufficient to support the phase partitioning, a minimum thickness of the liquid layer is required. If the growth front of the α phase moves faster than the melting front of the β phase, the liquid layer will be too thin and the lateral diffusion of the Ni and Sn atoms will be limited. As a result, Sn atoms will enrich ahead of the solidification front and stop the growth of the α phase. This ensures that the solidification front and the melting front will not be in contact with each other.

The above-mentioned process is also compatible with our observation of a finer microstructure obtained at a higher annealing temperature (see Fig 5.5). On the one hand, an enhanced heat flux is expected in the sample when heated at a higher annealing temperature, which leads to a higher driving force for the reverse peritectic reaction. As a result, the growth rate of the α phase will increase and a finer microstructure is favored, since it requires a shorter lateral diffusion length. On the other hand, the diffusion rate of both atoms will also increase at an elevated annealing temperature, and it tends to coarsen the microstructure to reduce the interfacial energy. In short, the size of the microstructure is the result of the competition between the increased overheating, which refines the microstructure, and the increased diffusion rate, which coarsens the microstructure. Compared to the increase of the diffusion rate that starts from a fixed value, the effect of a higher overheating is more prominent, since it starts from zero. This means that a finer structure is expected when heated at a higher annealing temperature, exactly as we observed.

Now we explain the origin of the cellular structure. The growth of the α phase is under the effect of constitutional supercooling, which destabilizes the initial planar solidification front. For the analysis of the growth process, we can consider an already existed α ($\mathrm{Ni_3Sn_2}$) nucleus, separated from a β ($\mathrm{Ni_3Sn_4}$) grain by a liquid film. A schematic of this construction is shown in Fig 5.9 (a).

Due to transport limitations, the β phase will be overheated above the peritectic temperature, T_p, before melting. Assuming that all solid/liquid interfaces are in the local equilibrium state, we can construct a constrained equilibrium (no α) at the β/L interface in the enlarged peritectic region of the Ni-Sn phase diagram, as shown in Fig 5.10. The red dashed line is the extension of the β-liquidus, and its intersection with the annealing temperature, T_exp, represents the β-L equilibrium, with the melt composition as $x^\mathrm{eq}_{\beta/\mathrm{L}}$. At the solidification front of the α nucleus, the local equilibrium is described by the intersection point of T_exp and the α-liquidus (the green line) at $x^\mathrm{eq}_{\alpha/\mathrm{L}}$. The difference in composition at the melting front and the solidification front

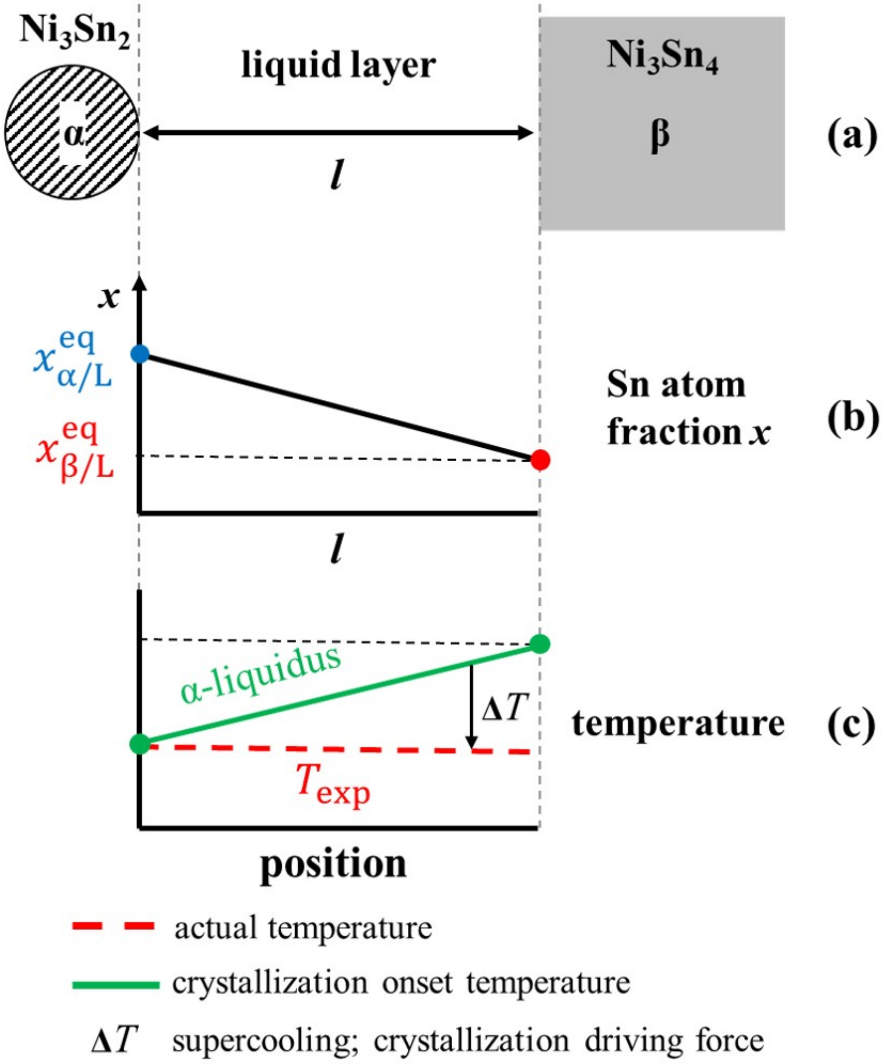

Figure 5.9: Temperature and composition profile within the liquid layer. (a) Geometry of the phases during peritectic melting. Ni_3Sn_2 nucleus is separated with Ni_3Sn_4 grain by a liquid Sn layer. (b) Composition (Sn) gradient within the liquid layer. (c) Actual temperature distribution (red dashed line) and liquidus temperature (green line) across the liquid layer.

creates a composition gradient within the liquid layer, as illustrated in Fig 5.9 (b).

The temperature profile of the liquid film is shown in Fig 5.9 (c), the solidification temperature, decided by the local composition of the melt and the α-liquidus, is shown as the green line. For the actual temperature of the melt, considering the small size of our sample, we assumed a constant temperature across the liquid layer, since the sample is uniformly heated in all directions. This is represented by the red dashed line, at the annealing temperature T_{exp}. It is evident that across the liquid layer, the actual temperature is lower

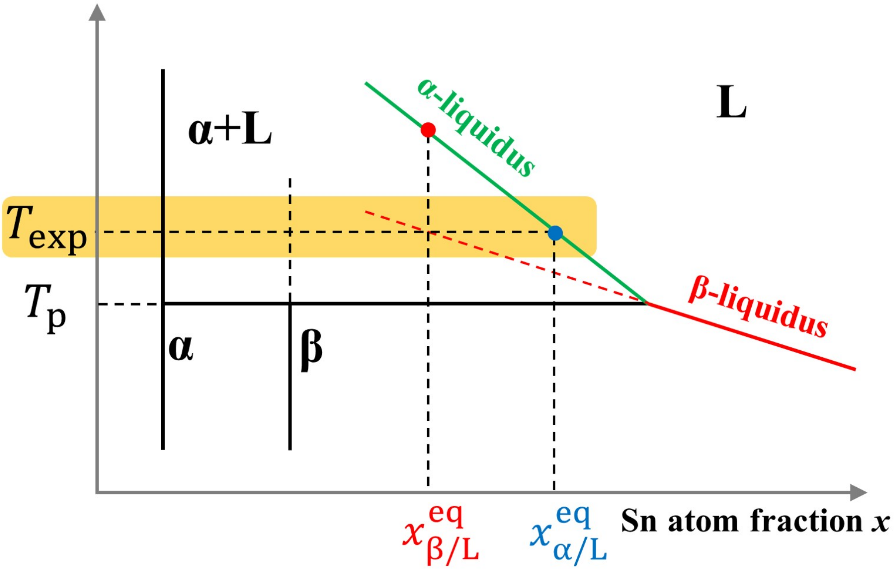

Figure 5.10: Schematic of the enlarged peritectic reaction area in the Ni-Sn phase diagram. The red dashed extended lines shows the constrained equilibrium between β (Ni_3Sn_4) phase and the melt, while the green line represents equilibrium between the α phase and the melt. T_p is the peritectic temperature and the annealing temperature is denoted as T_exp

than the solidification temperature of the melt, suggesting that the melt is in the supercooled state. The supercooling, ΔT, increases as moving away from the solidification front, indicating that the growth of the α phase is under the effect of constitutional supercooling. This reduces the stability of the solidification front and promotes cellular growth of the α phase [171], as discussed in Chapter 2. In conclusion, the clusters of Ni_3Sn_2 ligaments observed in this study are the result of phase partitioning and cellular growth induced by constitutional supercooling.

A similar constitutional supercooling scenario appears in peritectic melting of $Ba_2YCu_3O_{6+\delta}$ [189], which forms rod like BaY_2O_4 phase aligning with the direction of the imposed temperature gradient. In this study, the samples were heated homogeneously in the furnace and a constant temperature is assumed across the liquid layer. Constitutional supercooling is induced solely by the composition gradient within the melt, maintained by the dissolving β phase. Compared to the large grain size of β, the α nucleus is considered surrounded by β grains. Driven by a radial composition gradient, the α phase eventually grows into spherical or ellipsoidal clusters.

5.2.3 Comparing peritectic melting of Ni_3Sn_4 and TiAg

In Chapter 4, the microstructure of a partially decomposed sample is given in Fig 4.6, where a relatively smooth growth front was observed for the newly formed Ti phase. In

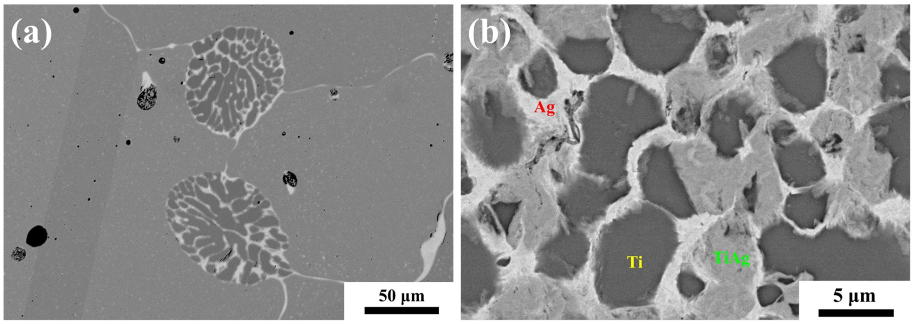

Figure 5.11: Comparing the partially decomposed microstructure of (a) Ni_3Sn_4 and (b) TiAg. The Ni_3Sn_2 phase shows a spherical cluster morphology, with the cell size much smaller than the original Ni_3Sn_4 grain size. For partially decomposed TiAg, the newly formed Ti phase has a similar size as the TiAg grains.

contrast, during peritectic melting of Ni_3Sn_4 the newly formed Ni_3Sn_2 phase follows a cellular growth mechanism. The differences in their microstructure are clearly shown in Fig 5.11.

For the solid product phases after peritectic melting, the cell size of Ni_3Sn_2 is roughly similar to the ligament size of Ti. The most obvious distinction between the two systems is the grain size of the master alloy, which is about 150 μm for Ni_3Sn_4 and 5 μm for TiAg. Judging from the partially decomposed samples, we see roughly one nucleus of the product phase per master grain in both systems. This means that during peritectic melting, the nucleus density is higher in Ti-Ag system, as the grain size is smaller. This is understandable since the lattice correspondence between Ti and TiAg described in Chapter 4 reduces the nucleation barrier. In contrast, nucleation is more difficult during peritectic melting of Ni_3Sn_4, indicated by the large distances between centers of clusters.

Due to the limited nuclei number, the Ni_3Sn_2 phase will eventually grow into large grains with a similar size as the original Ni_3Sn_4 grain size, as observed in Fig 5.4. During the growth process, the Ni_3Sn_2 phase is trapped in the wetted grain boundary area of the large Ni_3Sn_4 grains, as observed in Fig 5.11 (a). This makes it difficult for the liquid product phase (Sn) to move out of the grain boundary area. As a result, the cell structure of Ni_3Sn_2 is the natural product to accommodate the Sn melt. In contrast, the roughly similar size between the TiAg grain and the Ti ligament makes it easier to channel the Ag melt between the Ti grains. This leads to the less ordered structure seen in Fig 5.11 (b).

Chapter 6

Partial melting of $Cu_{93}In_7$ alloy

In Chapter 4 and 5, the potential of peritectic melting as a novel method of fabricating bicontinuous microstructures has been demonstrated. This idea can be further developed by moving from peritectic melting to partial melting, as both processes involve decomposition of a solid phase into a new solid phase and a liquid phase. As the key mechanism of forming bicontinuous microstructures, LFM has also been observed during partial melting of several alloys [118, 122, 126, 131, 137, 144]. In this chapter, $Cu_{93}In_7$ alloy is chosen as an example. The physical continuity of both phases obtained after partial melting is verified through electrochemical dealloying tests, proving that a bicontinuous microstructure can be obtained through partial melting. The results and images in this chapter have been published in Ref [138].

6.1 Results

6.1.1 Microstructure of $Cu_{93}In_7$ before and after partial melting

The phase diagram of the Cu-In system is shown in Fig 6.1 (a). The sample composition is chosen as $Cu_{93}In_7$ in this work. As can be seen from the green dot, after homogenization at $630\,^{\circ}\mathrm{C}$ and the quenching process, single phase Cu solid solution should be the expected phase. Indeed, as shown in Fig 6.1 (b), only one phase can be found in the as-homogenized sample, with some black spots that are casting pores, formed during solidification. This phase is identified as Cu solid solution by X-ray diffraction, shown as the black line in Fig 6.2. It can be noticed that the Bragg reflection positions for Cu in this work are shifted towards the smaller angle direction. This is caused by the larger lattice parameter of Cu solid solution compared to that of pure copper, as In solute atoms have a larger atomic radius.

Figure 6.1 (c) gives the two-phase microstructure after partial melting at $843\,^{\circ}\mathrm{C}$ for 4 min. The dark phase is Cu solid solution, which is the solid phase at the annealing temperature, and the bright phase at intergranular areas is the solidified melt. Judging from the X-ray diffraction result in Fig 6.2 (the red line), it at least contains β-Cu_4In. An enlarged view of the diffraction peaks in Fig 6.2 reveals a slight shift of Cu diffraction

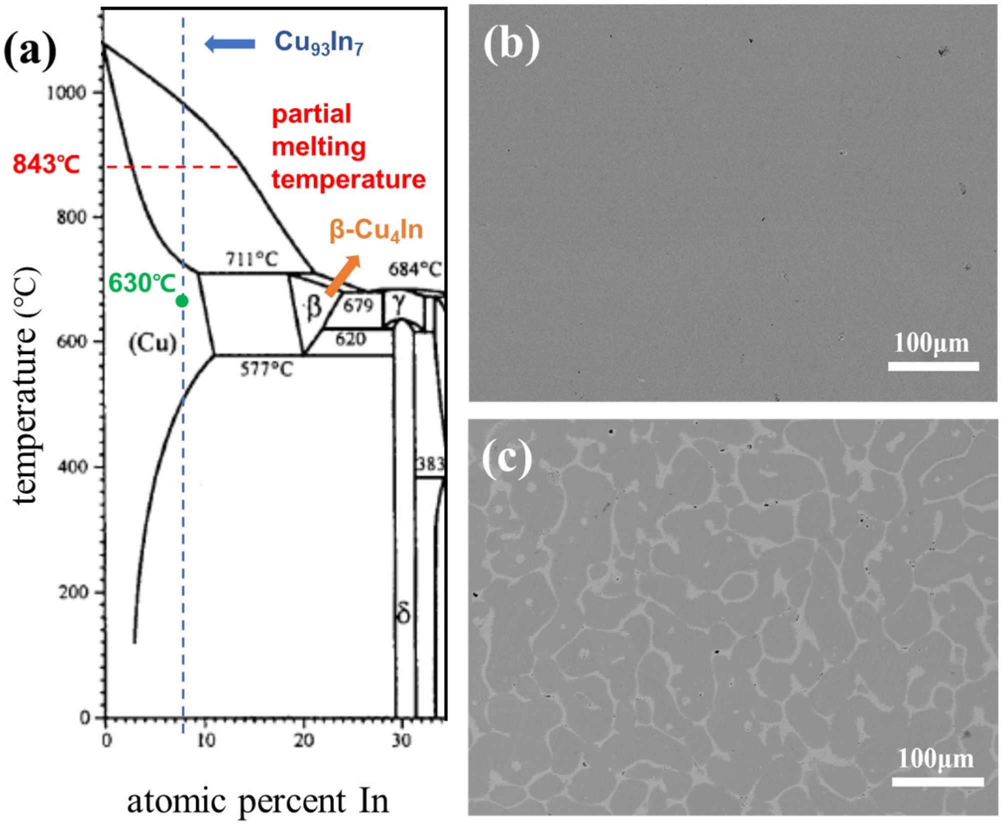

Figure 6.1: Microstructure of Cu-In samples. (a) The Cu-In phase diagram (after [190]). The blue dashed line shows the composition of the sample, the green dot indicates the homogenization temperature, while the red line represents the annealing temperature. (b) Backscattered electron (BSE) image of $Cu_{93}In_7$ after homogenization. No secondary phases were detected. (c) BSE image of $Cu_{93}In_7$ after partial melting (annealing at $843\,°C$ for 4 min). Two phases can be clearly observed.

peaks after partial melting. According to the phase diagram, the Cu solid solution phase after partial melting contains less In content, which decreases the lattice parameter and shifts the peak positions toward the Cu reference lines.

It is insufficient to judge the connectivity of the two phases from just 2D cross-sectional images. In order to check if a bicontinuous structure is obtained after partial melting, we performed dealloying test to remove one of the phases. After electrochemical dealloying in 0.5 M H_2SO_4 at -0.26 V, the solidified melt is selectively removed. Surface structure after partial melting and dealloying is shown on Fig 6.3 (a) and (b). The Cu solid solution phase remains unattacked by the acid, but the solidified melt with a higher In content disappeared and left behind a fine porous network structure at the intergranular areas.

We also ground the sample to reveal the cross section at the center area, the microstruc-

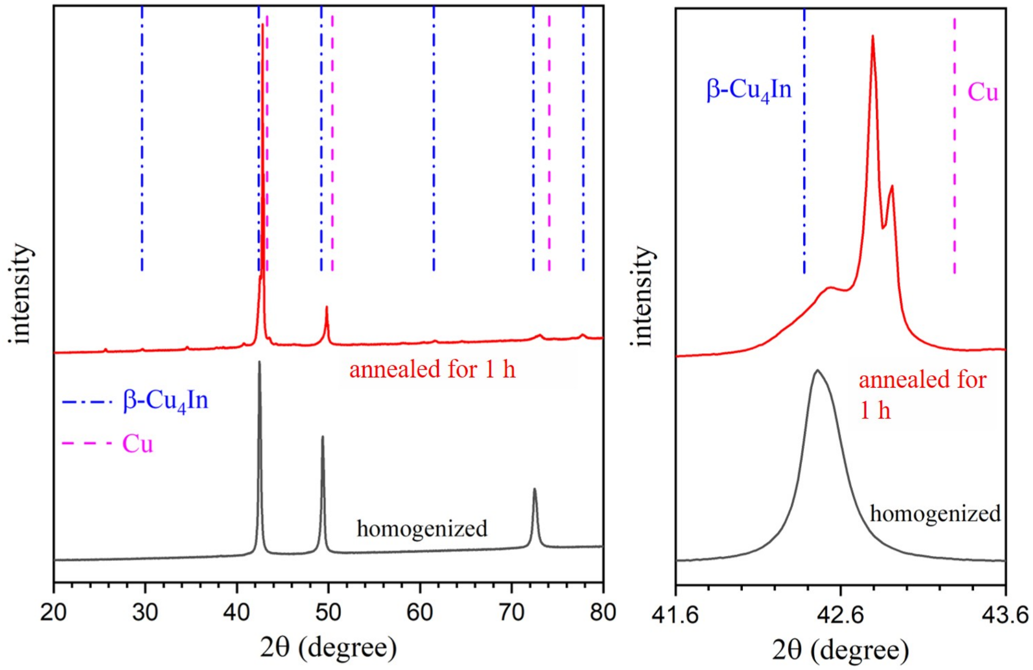

Figure 6.2: X-ray diffractograms of the as homogenized (black line) and the partial melted (red line, annealed for 1 h at $843\,^{\circ}\mathrm{C}$) sample. The homogenized sample shows the three strong diffraction peaks of Cu, with a shift towards the lower angle direction. A zoomed in image focusing at around 42 degree is shown on (b). The splitting (111) reflection is caused by the $K_{\alpha_{1/2}}$ wavelength doublet. Reference lines from Ref [191].

ture is shown in Fig 6.3 (c, d). To protect the structure after dealloying, the sample was vacuum embedded with epoxy. It can be seen from Fig 6.3 (c) that dealloying also happened in the interior of the sample. An enlarged image (Fig 6.3 (d)) shows inclusions with a bright contrast inside the unattacked Cu solid solution grains, as well as dark areas at the grain boundaries (see yellow arrows). These areas with a dark contrast are not observed for partial melted samples before dealloying, as shown in Fig 6.4.

The effect of heating duration on the final microstructure is also studied. Images of $Cu_{93}In_7$ samples after various heating durations are given in Fig 6.5. Based on images (a-d), which show microstructure evolution with prolonged heating time from 1 min to 60 min, an obvious coarsening effect in both phases can be observed. The corresponding dealloyed structures of these samples are given in Fig 6.5 (e-h).

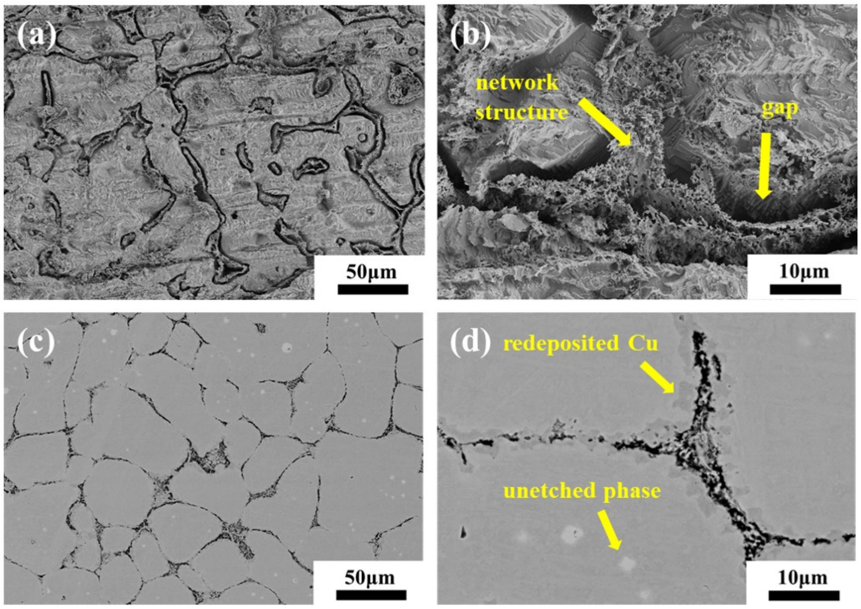

Figure 6.3: Microstructure of partial melted $Cu_{93}In_7$ samples after electrochemical dealloying. (a,b) Secondary electron image of the sample surface. The Cu solid solution phase remain unharmed, while the solidified melt at the intergranular areas is converted to a porous network structure. (c,d) Backscattered electron micrographs of the polished cross section. The sample was embedded with epoxy before grinding and polishing to preserve the gaps between Cu solid solution grains. Redeposited Cu can be found at the grain surfaces, while unetched In rich phase can be found inside the grains.

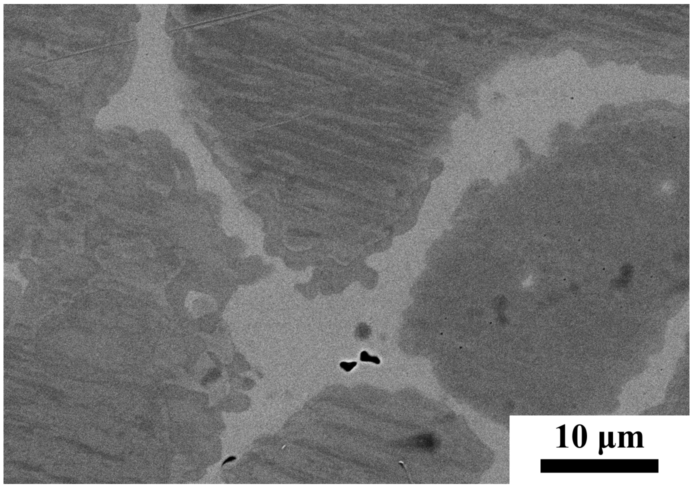

Figure 6.4: Microstructure of the Cu solid solution grain boundaries in a partial melted sample before dealloying. No area with a darker contrast can be detected at the curved grain boundaries.

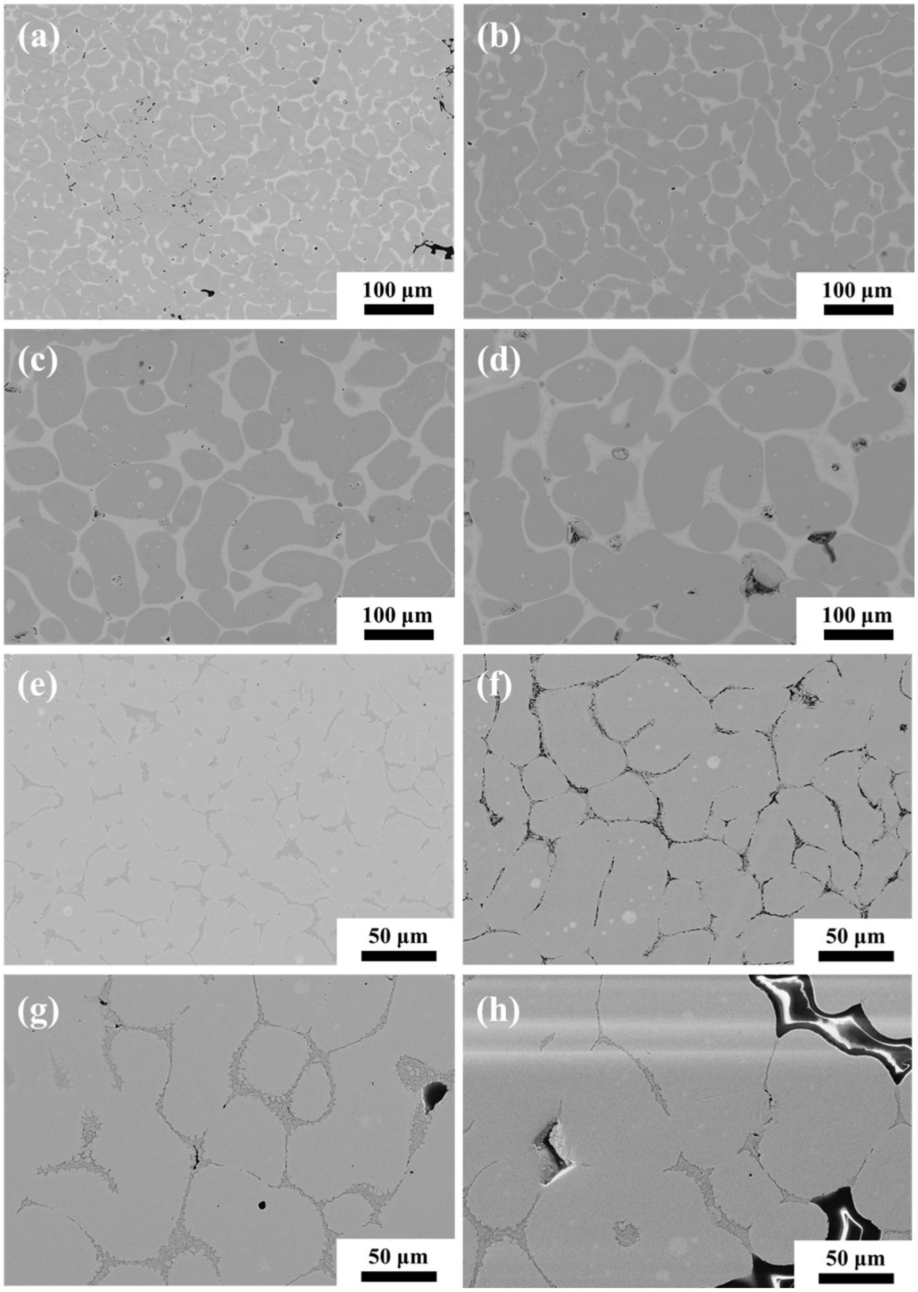

Figure 6.5: Microstructure of $Cu_{93}In_7$ samples after various heating durations. (a-d) Backscattered electron (BSE) images of sample cross section after annealing for 1, 4, 15, 60 min. The coarsening effect is quite obvious. (e-h) BSE images of dealloyed and embedded samples which went through the same heat treatment as in (a-d).

6.1.2 EBSD study of $Cu_{93}In_7$ alloy

EBSD tests were performed on $Cu_{93}In_7$ samples before and after partial melting. As can be seen from the inverse pole figure of the homogenized sample (see Fig 6.6 (a)), the Cu solid solution phase has a grain size of several hundred micrometers. No obvious texture can be found. Figure 6.6 (b) gives information about the boundaries. $\Sigma3$ coincidence site lattice (CSL) boundaries are the most frequently found boundary type, labeled in red. Most of the grain boundaries are found as random high angle grain boundaries (misorientation > 15 degree), while only a small amount of $\Sigma9$ boundaries appear in the sample.

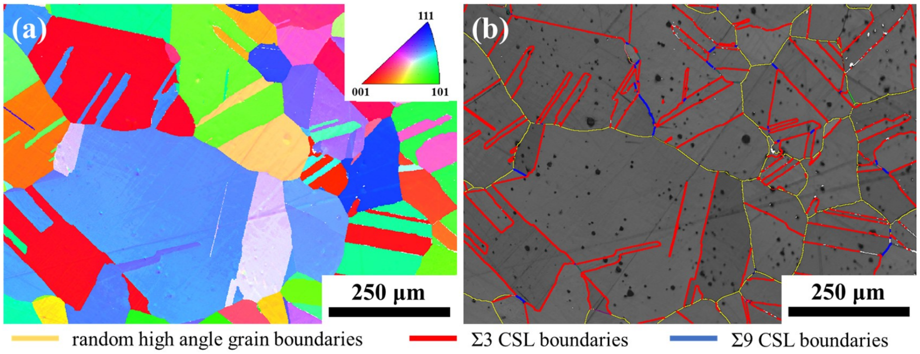

Figure 6.6: Electron backscatter diffraction results of homogenized $Cu_{93}In_7$. (a) Inverse pole figure of the sample, showing no texture after homogenization. (b) Boundaries labeled using Brandon criterion [192]. Mainly $\Sigma3$ boundaries (red) and random high angle grain boundaries (yellow) can be found. Small amount of $\Sigma9$ boundaries (blue) are also detected.

Structure after partial melting was also studied. As can be seen in Fig 6.7 (a), which shows the inverse pole figure of Cu solid solution phase only, some granules form clusters with the same orientation. The solidified melt phase is not shown, since no clear Kikuchi pattern can be obtained from that phase. Judging from the boundary character map shown in Fig 6.7 (b), more types of boundaries, including $\Sigma9$, $\Sigma11$, $\Sigma27$ a and $\Sigma27$ b can be detected in Cu solid solution phase after 4 min of annealing.

6.2 Discussion

6.2.1 Microstructure evolution during electrochemical dealloying

The bicontinuous structure after partial melting is verified with the dealloying test. As shown in Fig 6.3, dealloying happens at the surface area, as well as the interior. Cu solid solution phase remains unetched during electrochemical dealloying, suggesting that the dealloyed solidified melt, distributed at intergranular areas, is the only possible channel for the electrolyte to diffuse into the central area of the sample. The complete removal of the solidified melt indicates that it is a contiguous phase. Additionally, after dealloying, the bulk sample remains coherent and load bearing, which shows the excellent continuity of the Cu solid solution phase. In other words, two physically continued phases are obtained after partial melting, forming a bicontinuous structure.

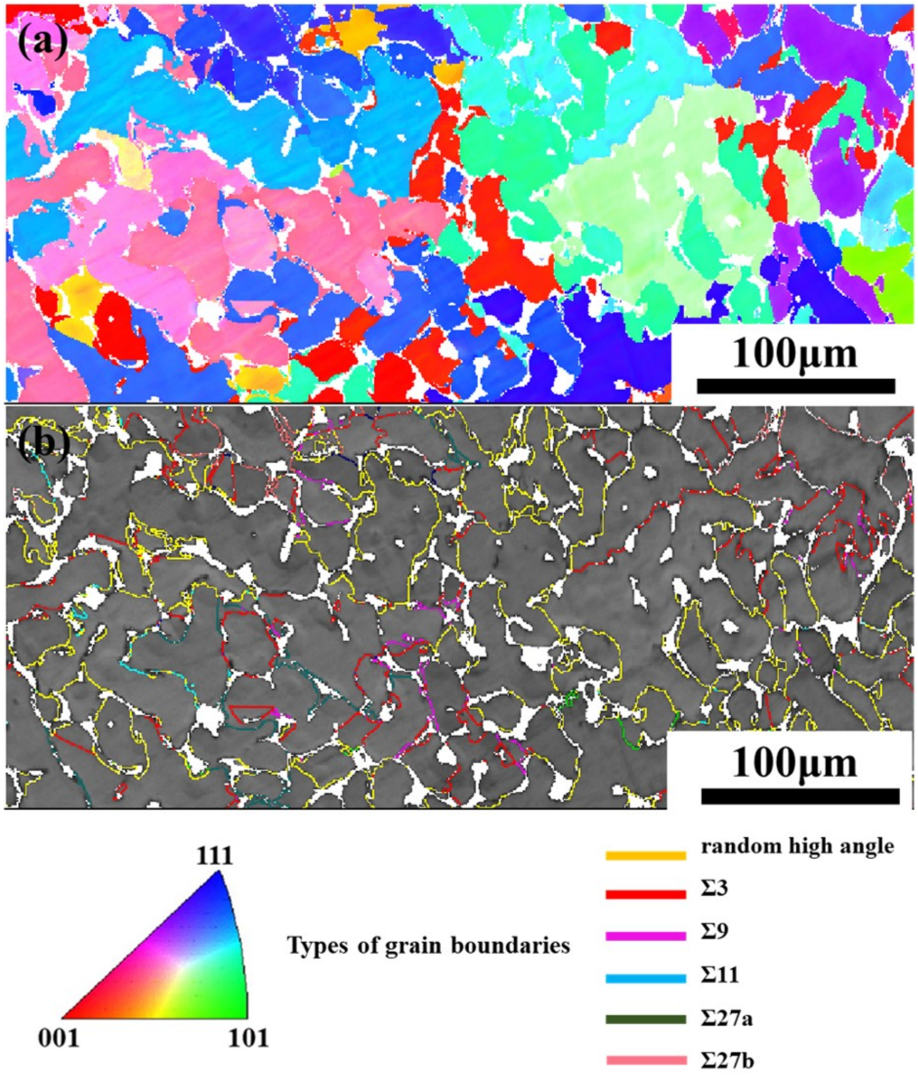

Figure 6.7: Electron backscatter diffraction characterization of the Cu solid solution phase in sample after partial melting for 4 min. (a) Inverse pole figure showing clusters of granules having the same orientation. (b) Boundary information

The inclusions found in Fig 6.3 (d) are identified as the solidified melt phase, as a higher In content brings a brighter contrast in the BSE image. These unetched inclusions found in dealloyed samples further confirm that the Cu solid solution phase is not attacked by the electrolyte during electrochemical dealloying. These inclusions can form due to nucleation at crystal defects (voids, dislocations) inside the Cu solid solution grains. It is also possible that these are the entrapped melt in the solid phase during coarsening at the annealing temperature. This structure can also be observed in other porous metals, as part of the pore space is converted to isolated voids during the coarsening process [49, 193].

Another feature found after electrochemical dealloying is the dark phase at the grain boundaries in Fig 6.3 (d), which is likely to be the redeposited Cu. Redeposition, due to excess chemical potential in the nanoporous structure, is also found in other dealloying studies [194, 195]. This is supported by the absence of dark areas in partial melted samples (see Fig 6.4) prior to dealloying. No obvious contrast difference can be found at the Cu solid solution boundaries, suggesting that the Cu richer particles only formed during electrochemical dealloying. Additionally, in the partial melted sample, curved grain boundaries with concave regions are found at the Cu solid solution grain boundaries, which are the preferential deposition sites for Cu.

An interesting feature here is the gap between the porous structure and the Cu solid solution grains, as indicated by the yellow arrow in Fig 6.3 (d). A similar phenomenon was found during dealloying of deposited AuAg alloy on massive gold substrates [59]. The Gibbs-Thompson excess chemical potential is affected by the mean curvature of the pore surfaces. The reduced mean curvature at the substrate surface leads to a curvature gradient, which prompts a divergence in the diffusive flux. As a result, the Au network structure at the substrate surface is broken, as Au atoms diffuse toward the substrate. The gaps observed in this study form through a similar mechanism, with Cu solid solution grains acting as the substrate.

6.2.2 Microstructure evolution during partial melting

EBSD results before and after partial melting bring insights of the formation mechanism of the bicontinuous structure. The grain size of the homogenized sample is about several hundred micrometers (see Fig 6.6 (a)), but the size of the Cu solid solution granules after 4 min of annealing is reduced to approximately 30 μm, showing an obvious refinement in microstructure.

Similar to peritectic melting of TiAg and Ni_3Sn_4 in previous chapters, the curved Cu solid solution/melt interface also shows characteristic feature of liquid film migration [196], which has been observed during partial melting of other Cu-In alloys as well [137]. Partial melting starts with grain boundary wetting. After Cu solid solution grains are separated by the melt, Cu and In atoms at the wetted boundaries dissolve into the melt, then deposit on the opposite grain with the equilibrium composition. Evidence of this mechanism is found in the partially melted sample (Fig 6.7 (a)), as many seemingly separated granules form clusters with the same orientation.

LFM offers a fast diffusion mechanism. Through LFM, Cu and In atoms can diffuse in the melt across the liquid layer, which is much faster than bulk diffusion. This is supported by the completely decomposed structure found after only 1 min of annealing (see Fig 6.5 (a,e)). Kirkendall voids are not detected in the Cu solid solution phase, due to the negligible contribution of solid-state diffusion. Essentially, partial melting proceeds through the same LFM mechanism as for peritectic melting discussed in previous chapters.

In peritectic melting, nucleation of the new solid phase can happen through heterogeneous (β-Ti in Chapter 4) or homogeneous (Ni_3Sn_2 in Chapter 5) nucleation, depending on interfacial energies. For partial melting of $Cu_{93}In_7$, since the new solid phase shares the same crystal lattice with the parent phase (they are both Cu solid solutions, only with different In contents), it is natural for the new phase to nucleate at the wetted grain boundaries of the parent phase.

It is easy to understand why the melt is a contiguous phase, as the wetted grain boundaries form a connected network. For the Cu solid solution phase, certain fraction of incompletely wetted grain boundaries are required. Previous study [96] on grain boundary wetting of Cu-In alloy suggests that some grain boundaries remain incompletely wetted during annealing between $715\,^{\circ}\mathrm{C}$ and $986\,^{\circ}\mathrm{C}$. This can be seen from the EBSD results shown in Fig 6.7 (b). The incompletely wetted random high angle grain boundaries contribute most to the connectivity of the Cu solid solution phase, similar to the Ti phase after annealing in Chapter 4.

The coarsening of both phases with prolonged annealing time can be clearly seen from Fig 6.5. Judging from Fig 6.5 (e-h), complete removal of the solidified melt phase in all samples suggests that an interconnected liquid phase forms after just 1 min of annealing, and remains interconnected during prolonged annealing time.

6.2.3 Distributed internal melting

In Chapter 4 and 5 we investigated how peritectic melting forms bicontinuous microstructures. However, the requirement of a peritectic reaction can greatly confine the application of this method to limited alloy systems. An alternative method is partial melting, which is demonstrated in this chapter. Partial melting is similar to the peritectic melting process, as both processes involve decomposition of one solid phase into a new solid phase and a liquid phase. However, partial melting requires only a two-phase region, which is ubiquitous in all alloy systems.

LFM has been identified as the key mechanism of generating bicontinuous microstructures. In both peritectic melting and partial melting processes, LFM starts at the pre-metled triple points and grain boundaries. As introduced in Chapter 1, pre-melting also happens at dislocations and vacancies. These crystal defects, distributed uniformly within the alloy, may serve as pre-melting sites and initiate the LFM process during melting. As a result, melting starts at various internal areas of the alloy, and generates a fine-scale phase mixture. Here, we name this process distributed internal melting (DIM).

The potential of obtaining bicontinuous structures through DIM has been demonstrated in this thesis, namely peritectic melting and partial melting. Compared with various dealloying methods that are commonly used to generate bicontinuous structures, the major advantage of DIM is that it does not require mass exchange with the environment. It has the potential of obtaining bicontinuous microstructures at a much larger scale, without mass transport being the rate limiting step as in different dealloying processes. The simple process of DIM is another advantage. Through DIM, a bicontinuous structure can form after heat treatments, without an imposed external dealloying environment, for example, electrolytes or metal melts.

Chapter 7

Conclusion

7.1 Liquid film migration during distributed internal melting

Previous research [45] has found that a bicontinuous structure containing contiguous Ti and Ag phases can be obtained by peritectic melting of TiAg. The mechanism behind this phenomenon was thought to be similar to liquid metal dealloying. For such a process, during peritectic melting, Ag atoms dissolve into the melt, and Ti atoms reorganize through surface diffusion and form Ti phase with a ligament structure. However, this explanation contradicts the experimental observation in this study.

In this work, the microstructure of the partially decomposed TiAg sample is carefully examined. Hemisphere-shaped Ti phase is found to be attached to TiAg grains, forming a planar TiAg/Ti interface. A convex Ti/melt interface is found, and across a liquid layer, a concave TiAg/melt interface is observed. The above mentioned microstructure cannot be explained by the dealloying-like mechanism. TEM-EDX line scan reveals that the Ag content in the Ti phase is lower at the interface and gradually increases to reach the equilibrium composition as it moves into the Ti grain. This gives an inverse composition gradient compared to the prediction based on the dealloying-like mechanism.

Based on the experimental results in this work, it is proposed that the decomposition of TiAg during peritectic melting follows the liquid film migration mechanism. The initial stage of peritectic melting is grain boundary wetting of TiAg grains. After that, the Ti phase will nucleate and grow at the expense of the TiAg phase. This happens through the LFM mechanism; i.e. both the Ti and Ag atoms dissolve in the melt, then diffuse across the liquid layer, and then deposit as β-Ti at the wetted grain boundary of TiAg.

Characteristic features of LFM were also observed during peritectic melting of Ni_3Sn_4, including Ni_3Sn_2 clusters with a convex periphery, Ni_3Sn_4 grains with a concave surface and the liquid layer in-between. This suggests that the decomposition of Ni_3Sn_4 follows the same LFM mechanism as for TiAg. Moreover, a bicontinuous structure formed through LFM is also observed after partial melting and quenching of $Cu_{93}In_7$ alloy. This extends the concept of fabricating bicontinuous structures through the LFM mechanism to distributed internal melting (DIM).

The product of the aforementioned processes is a bicontinuous structure consisting of two contiguous phases, which can be preserved by quenching in room temperature water. At the annealing temperature, the solid phase is found to be connected by incompletely wetted grain boundaries, while the melt forms a physically continued phase automatically.

7.2 Nucleation and growth mechanisms of the newly formed solid phase

7.2.1 Nucleation mechanisms

Planar Ti/TiAg interfaces are observed in partially decomposed TiAg samples. An orientation relationship between the newly formed Ti phase and the TiAg phase can be detected as $(0001)_\alpha \parallel (\bar{1}01)_{\mathrm{TiAg}}$, $[\bar{1}2\bar{1}0]_\alpha \parallel [010]_{\mathrm{TiAg}}$. Based on it, a possible orientation relationship at the annealing temperature is given as $(\bar{1}01)_\beta \parallel (\bar{1}01)_{\mathrm{TiAg}}$. This lattice correspondence favors heterogeneous nucleation of β-Ti at wetted TiAg grain boundaries, as it lowers the nucleation barrier of the Ti phase. After annealing, during the quenching process, phase transformation from β-Ti to α-Ti follows the Burgers orientation relationship. For partial melting of $Cu_{93}In_7$ alloy, the newly formed Cu solid solution phase also nucleates at the grain boundaries of the parent phase, as the new solid phase and the parent phase share the same lattice structure.

In addition to heterogeneous nucleation, the new solid phase can also nucleate through homogeneous nucleation, for example, during peritectic melting of Ni_3Sn_4. Unlike the hemispherical Ti phase in partially decomposed TiAg samples, the Ni_3Sn_2 clusters show a spherical or ellipsoidal shape, and no Ni_3Sn_2/Ni_3Sn_4 interface can be observed. This suggests that the Ni_3Sn_2 phase forms through homogeneous nucleation within the melt.

The interfacial energy between the new solid phase and the parent phase may affect the nucleation mechanism. If an orientation relationship exists between the phases that lowers the interfacial energy, then heterogeneous nucleation is favored. Otherwise, the new phase will nucleate homogeneously within the melt.

7.2.2 Growth mechanisms

Apart from the difference in nucleation mechanisms, the distinct growth mechanisms during peritectic melting of TiAg and Ni_3Sn_4 also lead to different microstructures. In partially decomposed TiAg samples, the hemispherical Ti phase has a relatively smooth growth front, while in partially decomposed Ni_3Sn_4 samples, spherical clusters of Ni_3Sn_2 ligaments can be found. The two structures represent the planar growth and the cellular growth at the growth front respectively.

The growth mechanism of the product phase can be affected by both the grain size of the master alloy and the nucleus density. In the case of large grain size and low nucleus density (peritectic melting of Ni_3Sn_4 in Chapter 5), spherical clusters of Ni_3Sn_2 cells are observed.

The cellular structure of the product phase, induced by constitutional supercooling, can accommodate the liquid Sn phase during phase partitioning. In contrast, in the case of small grain size and high nucleus density (peritectic melting of TiAg in Chapter 4), the newly formed Ag phase can be easily channeled to intergranular areas of TiAg grains. Without the requirement of accommodating the liquid Ag phase, the newly formed Ti phase grows to a less ordered granular structure.

7.3 Outlook

The study of distributed internal melting processes of metals in this thesis provides insight in both fundamentals of the melting process as well as practical applications for fabricating bicontinuous structures through DIM. However, both aspects of the field deserve to be further studied.

Many studies focus on the solidification microstructure after peritectic reaction [197–199], while for peritectic melting, research is scarce. LFM has only been predicted by phase field simulations [107] during peritectic melting. This thesis shows experimental evidence of LFM as the key microstructure formation mechanism during peritectic melting of TiAg and Ni_3Sn_4, however, it remains uncertain whether the LFM mechanism is ubiquitous during DIM processes of various alloys. Additional studies on more alloy systems are still required.

DIM utilizes crystal defects as pre-melting sites in alloys to generate fine-scale structures. A natural thought would be to increase the density of those defects by metal-forming techniques such as severe plastic deformation (SPD). This may lead to a finer structure after DIM by providing more positions for melt nucleation and also potentially reducing the time required for melting to mitigate the coarsening effect. By applying DIM to nano-grained master alloys, it might be possible to produce bicontinuous microstructures at nanoscale.

DIM of a single crystal is also worth exploring. An essential requirement of the LFM mechanism during DIM is grain boundary wetting, which generates the liquid layer as the fast diffusion channel. It is obvious that this can only be achieved in a polycrystalline material. Previous studies [200, 201] claim that peritectic melting of single-crystal FeZn forms eutectic-like colonies by cooperative growth of the solid and liquid phase, similar to eutectic and eutectoid reactions. The reaction starts at the sample surface and then proceeds into the master alloy. Until now, no other studies on peritectic melting of single-crystal intermetallic compounds have been found. For certain alloy systems, it might be possible that pre-melting happens at vacancies or dislocations within the single crystal lattice. In that case, melting starts at intragranular areas of the single crystal, and may produce a distinct structure from the eutectic-like structures. However, further studies on DIM of single crystal alloys are required before any conclusion can be made.

For application aspects, it has been revealed in this thesis that LFM is the key mechanism during DIM. Since LFM has been found in other material processing methods (see table 1.1), it is also worth finding out if bicontinuous structures can also form through those processes.

Finally, the distinct structure obtained after peritectic melting of TiAg and Ni_3Sn_4 has shown the effect of nucleation and growth process on the final microstructure. In future studies, these processes could potentially be controlled by different heating methods (for example, directional melting), or by changing the composition of the master alloy in order to obtain different microstructures.

References

[1] L. Scriven, Equilibrium bicontinuous structure, Nature 263 (1976) 123–125.

[2] N. Beets, Y. Cui, D. Farkas, A. Misra, Mechanical response of a bicontinuous copper–molybdenum nano-composite: Experiments and simulations, Acta Mater. 178 (2019) 79–89.

[3] I. McCue, S. Ryan, K. Hemker, X. Xu, N. Li, M. Chen, J. Erlebacher, Size effects in the mechanical properties of bulk bicontinuous Ta/Cu nanocomposites made by liquid metal dealloying, Adv. Eng. Mater. 18 (2016) 46–50.

[4] I. Okulov, P.-A. Geslin, I. Soldatov, H. Ovri, S.-H. Joo, H. Kato, Anomalously low modulus of the interpenetrating-phase composite of Fe and Mg obtained by liquid metal dealloying, Scr. Mater. 163 (2019) 133–136.

[5] S.-H. Joo, H. Kato, I. V. Okulov, Evolution of 3d interconnected composites of high-entropy TiVNbMoTa alloys and Mg during liquid metal dealloying, Composites, Part B 222 (2021) 109044.

[6] H.-J. Jin, X.-L. Wang, S. Parida, K. Wang, M. Seo, J. Weissmüller, Nanoporous Au- Pt alloys as large strain electrochemical actuators, Nano Lett. 10 (2010) 187–194.

[7] H.-J. Jin, J. Weissmüller, A material with electrically tunable strength and flow stress, Science 332 (2011) 1179–1182.

[8] I. McCue, E. Benn, B. Gaskey, J. Erlebacher, Dealloying and dealloyed materials, Annu. Rev. Mater. Res. 46 (2016) 263–286.

[9] R. Song, J. Han, M. Okugawa, R. Belosludov, T. Wada, J. Jiang, D. Wei, A. Kudo, Y. Tian, M. Chen, et al., Ultrafine nanoporous intermetallic catalysts by high-temperature liquid metal dealloying for electrochemical hydrogen production, Nat. Commun. 13 (2022) 5157.

[10] Y. Cui, B. Derby, N. Li, A. Misra, Design of bicontinuous metallic nanocomposites for high-strength and plasticity, Mater. Des. 166 (2019) 107602.

[11] Y. B. Jeong, T. Wada, S.-H. Joo, J.-M. Park, J. Moon, H. S. Kim, I. V. Okulov, S. H. Park, J. H. Lee, K. B. Kim, et al., Beyond strength-ductility trade-off: 3d interconnected heterostructured composites by liquid metal dealloying, Composites, Part B 225 (2021) 109266.

[12] J. E. Jang, J. Seong, S.-H. Joo, S. H. Park, Development of 3d bicontinuous metal–intermetallic composites through subsequent alloying process after liquid metal dealloying, J. Magnesium Alloys 11 (2023) 4274–4281.

[13] H. Guan, H. Xie, Z.-P. Luo, W.-K. Bao, Z.-S. You, Z. Jin, H.-J. Jin, Ultrastrong spinodoid alloys enabled by electrochemical dealloying and refilling, PNAS 120 (2023) e2214773120.

[14] I. V. Okulov, J. Wilmers, S.-H. Joo, S. Bargmann, H. S. Kim, H. Kato, Anomalous compliance of interpenetrating-phase composite of Ti and Mg synthesized by liquid metal dealloying, Scr. Mater. 194 (2021) 113660.

[15] A. Wittstock, B. Neumann, A. Schaefer, K. Dumbuya, C. Kübel, M. M. Biener, V. Zielasek, H.-P. Steinrück, J. M. Gottfried, J. Biener, et al., Nanoporous Au: an unsupported pure gold catalyst?, J. Phys. Chem. C 113 (2009) 5593–5600.

[16] J.-J. Gao, G.-P. Zhou, H.-J. Qiu, Y. Wang, J. Wang, Dealloying monolithic Pt-Cu alloy to wire-like nanoporous structure for electrocatalysis and electrochemical sensing, Corros. Sci. 108 (2016) 194–199.

[17] X. Wang, F. Peng, B. Chang, Sound absorption of porous metals at high sound pressure levels, J. Acoust. Soc. Am. 126 (2009) EL55–EL61.

[18] D. Zhou, W. Stronge, Mechanical properties of fibrous core sandwich panels, Int. J. Mech. Sci. 47 (2005) 775–798.

[19] S.-I. Kim, S.-W. Kim, K. Jung, J.-B. Kim, J.-H. Jang, Ideal nanoporous gold based supercapacitors with theoretical capacitance and high energy/power density, Nano Energy 24 (2016) 17–24.

[20] S. Zhou, X. Yang, Y. Lin, J. Xie, D. Wang, A nanonet-enabled Li ion battery cathode material with high power rate, high capacity, and long cycle lifetime, ACS nano 6 (2012) 919–924.

[21] H.-J. Jin, J. Weissmüller, Bulk nanoporous metal for actuation, Adv. Eng. Mater. 12 (2010) 714–723.

[22] W.-K. Hu, L.-Z. Liu, L. Zou, J.-C. Shao, S.-G. Wang, H.-J. Jin, Synthesis and mechanical properties of porous metals with inverted dealloying structure, Scr. Mater. 210 (2022) 114483.

[23] J. W. Cahn, Phase separation by spinodal decomposition in isotropic systems, J. Chem. Phys. 42 (1965) 93–99.

[24] C. Soyarslan, S. Bargmann, M. Pradas, J. Weissmüller, 3d stochastic bicontinuous microstructures: Generation, topology and elasticity, Acta Mater. 149 (2018) 326–340.

[25] Q. Chen, Bicontinuous nanoporous metals with self-organized functionalities, Chem. Mater. 34 (2022) 10237–10248.

[26] K. Campo, E. Lopes, C. Parrish, R. Caram, Rapid quenching of semisolid Ti-Cu alloys: Insights into globular microstructure formation and coarsening, Acta Mater. 139 (2017) 86–95.

[27] K. Sieradzki, R. Newman, Stress-corrosion cracking, J. Phys. Chem. Solids 48 (1987) 1101–1113.

[28] R. Newman, T. Shahrabi, K. Sieradzki, Film-induced cleavage of alpha-brass, Scr. Metall. 23 (1989) 71–74.

[29] J. Erlebacher, M. J. Aziz, A. Karma, N. Dimitrov, K. Sieradzki, Evolution of nanoporosity in dealloying, Nature 410 (2001) 450–453.

[30] Q. Chen, K. Sieradzki, Mechanisms and morphology evolution in dealloying, J. Electrochem. Soc. 160 (2013) C226.

[31] J. Erlebacher, An atomistic description of dealloying: porosity evolution, the critical potential, and rate-limiting behavior, J. Electrochem. Soc. 151 (2004) C614.

[32] L. Qian, M. Chen, Ultrafine nanoporous gold by low-temperature dealloying and kinetics of nanopore formation, Appl. Phys. Lett. 91 (2007).

[33] X. Wang, Z. Qi, C. Zhao, W. Wang, Z. Zhang, Influence of alloy composition and dealloying solution on the formation and microstructure of monolithic nanoporous silver through chemical dealloying of Al-Ag alloys, J. Phys. Chem. C 113 (2009) 13139–13150.

[34] T. Wada, K. Yubuta, A. Inoue, H. Kato, Dealloying by metallic melt, Mater. Lett. 65 (2011) 1076–1078.

[35] T. Wada, K. Yubuta, H. Kato, Evolution of a bicontinuous nanostructure via a solid-state interfacial dealloying reaction, Scr. Mater. 118 (2016) 33–36.

[36] C. Zhao, K. Kisslinger, X. Huang, J. Bai, X. Liu, C.-H. Lin, L.-C. Yu, M. Lu, X. Tong, H. Zhong, et al., Design nanoporous metal thin films via solid state interfacial dealloying, Nanoscale 13 (2021) 17725–17736.

[37] I. McCue, B. Gaskey, P.-A. Geslin, A. Karma, J. Erlebacher, Kinetics and morphological evolution of liquid metal dealloying, Acta Mater. 115 (2016) 10–23.

[38] J. W. Kim, M. Tsuda, T. Wada, K. Yubuta, S. G. Kim, H. Kato, Optimizing niobium dealloying with metallic melt to fabricate porous structure for electrolytic capacitors, Acta Mater. 84 (2015) 497–505.

[39] J.-C. Shao, H.-J. Jin, From liquid metal dealloying to liquid metal expulsion, J. Mater. Sci. 55 (2020) 8337–8345.

[40] B. Gaskey, I. McCue, A. Chuang, J. Erlebacher, Self-assembled porous metal-intermetallic nanocomposites via liquid metal dealloying, Acta Mater. 164 (2019) 293–300.

[41] I. V. Okulov, S. V. Lamaka, T. Wada, K. Yubuta, M. L. Zheludkevich, J. Weissmüller, J. Markmann, H. Kato, Nanoporous magnesium, Nano Res. 11 (2018) 6428–6435.

[42] Z. Lu, C. Li, J. Han, F. Zhang, P. Liu, H. Wang, Z. Wang, C. Cheng, L. Chen, A. Hirata, et al., Three-dimensional bicontinuous nanoporous materials by vapor phase dealloying, Nat. Commun. 9 (2018) 276.

[43] J. Han, C. Li, Z. Lu, H. Wang, Z. Wang, K. Watanabe, M. Chen, Vapor phase dealloying: A versatile approach for fabricating 3d porous materials, Acta Mater. 163 (2019) 161–172.

[44] Z. Lu, F. Zhang, D. Wei, J. Han, Y. Xia, J. Jiang, M. Zhong, A. Hirata, K. Watanabe, A. Karma, et al., Vapor phase dealloying kinetics of MnZn alloys, Acta Mater. 212 (2021) 116916.

[45] W.-K. Hu, J.-C. Shao, S.-G. Wang, H.-J. Jin, Evolution of a bicontinuous structure in peritectic melting: The simplest form of dealloying, Phys. Rev. Mater. 3 (2019) 113601.

[46] A. K. Ng, S. S. Welborn, E. Detsi, Time-dependent power law function for the post-dealloying chemical coarsening of nanoporous gold derived using small-angle X-ray scattering, Scr. Mater. 206 (2022) 114215.

[47] Y. Ding, Y.-J. Kim, J. Erlebacher, Nanoporous gold leaf:“ancient technology”/advanced material, Adv. Mater. 16 (2004) 1897–1900.

[48] C. Zhao, T. Wada, V. De Andrade, G. J. Williams, J. Gelb, L. Li, J. Thieme, H. Kato, Y.-c. K. Chen-Wiegart, Three-dimensional morphological and chemical evolution of nanoporous stainless steel by liquid metal dealloying, ACS Appl. Mater. Interfaces 9 (2017) 34172–34184.

[49] J. Erlebacher, Mechanism of coarsening and bubble formation in high-genus nanoporous metals, Phys. Rev. Lett. 106 (2011) 225504.

[50] K. Kolluri, M. J. Demkowicz, Coarsening by network restructuring in model nanoporous gold, Acta Mater. 59 (2011) 7645–7653.

[51] F. Kertis, J. Snyder, L. Govada, S. Khurshid, N. Chayen, J. Erlebacher, Structure/processing relationships in the fabrication of nanoporous gold, Jom 62 (2010) 50–56.

[52] M. Ziehmer, K. Hu, K. Wang, E. T. Lilleodden, A principle curvatures analysis of the isothermal evolution of nanoporous gold: Quantifying the characteristic length-scales, Acta Mater. 120 (2016) 24–31.

[53] H. Jeon, N.-R. Kang, E.-J. Gwak, J.-i. Jang, H. N. Han, J. Y. Hwang, S. Lee, J.-Y. Kim, Self-similarity in the structure of coarsened nanoporous gold, Scr. Mater. 137 (2017) 46–49.

[54] S. Bapari, L. Lührs, J. Weissmüller, Metrics for the characteristic length scale in the random bicontinuous microstructure of nanoporous gold, Acta Mater. 260 (2023) 119333.

[55] J. Wang, R. Xia, J. Zhu, Y. Ding, X. Zhang, Y. Chen, Effect of thermal coarsening on the thermal conductivity of nanoporous gold, J. Mater. Sci. 47 (2012) 5013–5018.

[56] S.-H. Joo, J. W. Bae, W.-Y. Park, Y. Shimada, T. Wada, H. S. Kim, A. Takeuchi, T. J. Konno, H. Kato, I. V. Okulov, Beating thermal coarsening in nanoporous materials via high-entropy design, Adv. Mater. 32 (2020) 1906160.

[57] Y. Li, B.-N. Dinh Ngô, J. Markmann, J. Weissmüller, Topology evolution during coarsening of nanoscale metal network structures, Phys. Rev. Mater. 3 (2019) 076001.

[58] B. Zandersons, L. Lührs, Y. Li, J. Weissmüller, On factors defining the mechanical behavior of nanoporous gold, Acta Mater. 215 (2021) 116979.

[59] G. Henkelmann, D. Waldow, M. Liu, L. Lührs, Y. Li, J. Weissmüller, Self-detachment and subsurface densification of dealloyed nanoporous thin films, Nano Lett. 22 (2022) 6787–6793.

[60] J. Snyder, P. Asanithi, A. B. Dalton, J. Erlebacher, Stabilized nanoporous metals by dealloying ternary alloy precursors, Adv. Mater. 20 (2008) 4883–4886.

[61] A. A. Vega, R. C. Newman, Nanoporous metals fabricated through electrochemical dealloying of Ag-Au-Pt with systematic variation of Au:Pt ratio, J. Electrochem. Soc. 161 (2013) C1.

[62] A. Kosinova, D. Wang, E. Baradács, B. Parditka, T. Kups, L. Klinger, Z. Erdélyi, P. Schaaf, E. Rabkin, Tuning the nanoscale morphology and optical properties of porous gold nanoparticles by surface passivation and annealing, Acta Mater. 127 (2017) 108–116.

[63] A. Chen, S. Shi, Y. Qiu, X. Xie, H. Ruan, J. Gu, D. Pan, Pore-size tuning and optical performances of nanoporous gold films, Microporous Mesoporous Mater. 202 (2015) 50–56.

[64] C. Rurainsky, A. G. Manjón, F. Hiege, Y.-T. Chen, C. Scheu, K. Tschulik, Electrochemical dealloying as a tool to tune the porosity, composition and catalytic activity of nanomaterials, J. Mater. Chem. A 8 (2020) 19405–19413.

[65] Z. Qi, J. Weissmuller, Hierarchical nested-network nanostructure by dealloying, Acs Nano 7 (2013) 5948–5954.

[66] S. Shi, Y. Li, B.-N. Ngo-Dinh, J. Markmann, J. Weissmüller, Scaling behavior of stiffness and strength of hierarchical network nanomaterials, Science 371 (2021) 1026–1033.

[67] J. Campbell, Castings, Elsevier, 2003.

[68] D. Brandon, W. D. Kaplan, Joining processes: an introduction, John Wiley & Sons, 1997.

[69] D. H. Kirkwood, M. Suéry, P. Kapranos, H. V. Atkinson, K. P. Young, Semi-solid processing of alloys, volume 124, Springer, 2010.

[70] S. M. A. Bukhari, N. Husnain, F. A. Siddiqui, M. T. Anwar, A. A. Khosa, M. Imran, T. H. Qureshi, R. Ahmad, Effect of laser surface remelting on microstructure, mechanical properties and tribological properties of metals and alloys: A review, Opt. Laser Technol. 165 (2023) 109588.

[71] I. Gibson, D. Rosen, B. Stucker, M. Khorasani, D. Rosen, B. Stucker, M. Khorasani, Additive manufacturing technologies, volume 17, Springer, 2021.

[72] M. Rettenmayr, Melting and remelting phenomena, Int. Mater. Rev. 54 (2009) 1–17.

[73] M. Hillert, M. Rettenmayr, Deviation from local equilibrium at migrating phase interfaces, Acta Mater. 51 (2003) 2803–2809.

[74] J. C. Baker, J. W. Cahn, Thermodynamics of Solidification, American Society for Metals, Metals Park, Ohio, 1971, pp. 23–58.

[75] M. Hillert, Solute drag, solute trapping and diffusional dissipation of gibbs energy, Acta Mater. 47 (1999) 4481–4505.

[76] B. Chalmers, Principles of solidification, Springer, 1964.

[77] M. Faraday, Experimental researches in chemistry and physics, CRC Press, 1990.

[78] J. W. Frenken, P. M. Marée, J. F. Van Der Veen, Observation of surface-initiated melting, Phys. Rev. B 34 (1986) 7506.

[79] A. D. van der Gon, R. Smith, J. Gay, D. O'connor, J. Van der Veen, Melting of Al surfaces, Surf. Sci. 227 (1990) 143–149.

[80] R. Barnett, U. Landman, Surface premelting of Cu (110), Phys. Rev. B 44 (1991) 3226.

[81] E. Chen, R. Barnett, U. Landman, Surface melting of Ni (110), Phys. Rev. B 41 (1990) 439.

[82] B. Pluis, A. D. Van der Gon, J. Frenken, J. van der Veen, Crystal-face dependence of surface melting, Phys. Rev. Lett. 59 (1987) 2678.

[83] Q. Mei, K. Lu, Melting and superheating of crystalline solids: From bulk to nanocrystals, Prog. Mater Sci. 52 (2007) 1175–1262.

[84] F. Inoko, T. Okada, T. Nishimura, M. Ohomori, T. Yoshikawa, Strain induced grain boundary premelting along twin boundaries in copper polycrystals, Interface Sci. 7 (1999) 131–140.

[85] S. Divinski, M. Lohmann, C. Herzig, B. Straumal, B. Baretzky, W. Gust, Grain-boundary melting phase transition in the Cu-Bi system, Phys. Rev. B: Condens. Matter 71 (2005) 104104.

[86] A. M. Alsayed, M. F. Islam, J. Zhang, P. J. Collings, A. G. Yodh, Premelting at defects within bulk colloidal crystals, Science 309 (2005) 1207–1210.

[87] J. Luo, V. Gupta, D. Yoon, H. Meyer, Segregation-induced grain boundary premelting in nickel-doped tungsten, Appl. Phys. Lett. 87 (2005).

[88] L. Burakovsky, D. L. Preston, R. R. Silbar, Melting as a dislocation-mediated phase transition, Phys. Rev. B 61 (2000) 15011.

[89] M. Pokorny, G. Grimvall, Pre-melting effects in lead from resistance measurements, J. Phys. F: Met. Phys. 14 (1984) 931.

[90] J. Lutsko, D. Wolf, S. Phillpot, S. Yip, Molecular-dynamics study of lattice-defect-nucleated melting in metals using an embedded-atom-method potential, Phys. Rev. B 40 (1989) 2841.

[91] J. Broughton, G. Gilmer, Thermodynamic criteria for grain-boundary melting: a molecular-dynamics study, Phys. Rev. Lett. 56 (1986) 2692.

[92] P. Stoltze, Simulations of the premelting of Al (110), J. Chem. Phys. 92 (1990) 6306–6321.

[93] J. Daeges, H. Gleiter, J. Perepezko, Superheating of metal crystals, Phys. Lett. A 119 (1986) 79–82.

[94] D. Zhang, B. Cantor, Melting behaviour of In and Pb particles embedded in an Al matrix, Acta Metall. Mater. 39 (1991) 1595–1602.

[95] K. Chattopadhyay, R. Goswami, Melting and superheating of metals and alloys, Prog. Mater Sci. 42 (1997) 287–300.

[96] A. Straumal, B. Bokstein, A. Petelin, B. Straumal, B. Baretzky, A. Rodin, A. Nekrasov, Apparently complete grain boundary wetting in Cu–In alloys, J. Mater. Sci. 47 (2012) 8336–8343.

[97] G. López, E. Mittemeijer, B. Straumal, Grain boundary wetting by a solid phase; microstructural development in a Zn–5 wt% Al alloy, Acta Mater. 52 (2004) 4537–4545.

[98] I. Mazilkin, K. Tsoy, A. Straumal, A. Rodin, B. Baretzky, Grain boundary wetting of different types of grain boundaries in the Cu–Ag system, Mater. Lett. 272 (2020) 127730.

[99] M. C. Flemings, Behavior of metal alloys in the semisolid state, Metall. Trans. A 22 (1991) 957–981.

[100] Z. Fan, Semisolid metal processing, Int. Mater. Rev. 47 (2002) 49–85.

[101] W. Loue, M. Suery, Microstructural evolution during partial remelting of Al- Si7Mg alloys, Mater. Sci. Eng., A 203 (1995) 1–13.

[102] E. Zoqui, M. Shehata, M. Paes, V. Kao, E. Es-Sadiqi, Morphological evolution of SSM A356 during partial remelting, Mater. Sci. Eng., A 325 (2002) 38–53.

[103] T. Chen, Y. Hao, J. Sun, Microstructural evolution of previously deformed ZA27 alloy during partial remelting, Mater. Sci. Eng., A 337 (2002) 73–81.

[104] N. Limodin, L. Salvo, M. Suéry, M. DiMichiel, In situ investigation by X-ray tomography of the overall and local microstructural changes occurring during partial remelting of an Al–15.8 wt.% Cu alloy, Acta Mater. 55 (2007) 3177–3191.

[105] J.-Y. Li, S. Sugiyama, J. Yanagimoto, Y.-L. Chen, G.-W. Fan, Effect of inverse peritectic reaction on microstructural spheroidization in semi-solid state, J. Mater. Process. Technol. 208 (2008) 165–170.

[106] E. A. Brener, D. Temkin, Melting of alloys along the inter-phase boundaries in eutectic and peritectic systems, Acta Mater. 55 (2007) 2785–2789.

[107] G. Boussinot, E. Brener, D. Temkin, Kinetics of isothermal phase transformations above and below the peritectic temperature: Phase-field simulations, Acta Mater. 58 (2010) 1750–1760.

[108] E. A. Brener, G. Boussinot, C. Hüter, M. Fleck, D. Pilipenko, R. Spatschek, D. Temkin, Pattern formation during diffusional transformations in the presence of triple junctions and elastic effects, J. Phys.: Condens. Matter 21 (2009) 464106.

[109] A. Viardin, G. Boussinot, J. Zollinger, Phase field modeling of partial remelting during reheating of a multiphase peritectic solidification microstructure, Materialia 26 (2022) 101590.

[110] N. Reilly, B. Rouat, G. Martin, D. Daloz, J. Zollinger, Enhanced dendrite fragmentation through the peritectic reaction in TiAl-based alloys, Intermetallics 86 (2017) 126–133.

[111] A. King, Diffusion induced grain boundary migration, Int. Mater. Rev. 32 (1987) 173–189.

[112] D. Y. Yoon, Theories and observations of chemically induced interface migration, Int. Mater. Rev. 40 (1995) 149–179.

[113] I. Manna, S. Pabi, W. Gust, Discontinuous reactions in solids, Int. Mater. Rev. 46 (2001) 53–91.

[114] W. Pfann, Temperature gradient zone melting, Jom 7 (1955) 961–964.

[115] H. Pickering, C. Wagner, Electrolytic dissolution of binary alloys containing a noble metal, J. Electrochem. Soc. 114 (1967) 698.

[116] W. McPhee, G. Schaffer, J. Drennan, The effect of iron on liquid film migration and sintering of an Al–Cu–Mg alloy, Acta Mater. 51 (2003) 3701–3712.

[117] O. Ojo, N. Richards, M. Chaturvedi, Liquid film migration of constitutionally liquated γ' in weld heat affected zone (HAZ) of Inconel 738LC superalloy, Scr. Mater. 51 (2004) 141–146.

[118] J. K. Kim, D. Y. Yoon, The suppression of chemically induced liquid film migration in Co-Cu at high temperature, Acta Metall. Mater. 42 (1994) 913–919.

[119] B. Radhakrishnan, R. Thompson, Liquid film migration (LFM) in the weld heat affected zone (HAZ) of a Ni-base superalloy, Scr. Metall. Mater. 24 (1990) 537–542.

[120] H.-S. Shin, J.-S. Kim, D.-Y. Yoon, Y.-D. Song, The liquid film migration in a sintered Fe-Cr-C base alloy, Metall. Mater. Trans. A 26 (1995) 1389–1393.

[121] R. Nakkalil, N. Richards, M. Chaturvedi, Grain boundary liquid film migration during welding of Incoloy 903, Scr. Metall. Mater. 26 (1992).

[122] B. Young-Joon, D. N. Yoon, Migration of liquid film and grain boundary in Mo-Ni induced by temperature change, Acta Metall. 33 (1985) 1911–1917.

[123] K.-R. Lee, Y.-J. Baik, D. N. Yoon, A critical test for the coherency strain energy as the driving force for the discontinuous precipitation in Mo-Ni alloy, Acta Metall. 35 (1987) 2145–2150.

[124] S. Chen, H. Hu, M. Zhao, L. Rong, Effect of post-weld aging treatment on the precipitation and mechanical behavior of Fe-Ni based alloy weldment, Mater. Sci. Eng. A 718 (2018) 363–370.

[125] H. K. Rang, S. Hackney, D. Yoon, Migration of liquid film and grain boundary in Mo-Ni induced by W diffusion, Acta Metall. 36 (1988) 695–699.

[126] A. Kliauga, M. Ferrante, Liquid formation and microstructural evolution during re-heating and partial melting of an extruded A356 aluminium alloy, Acta Mater. 53 (2005) 345–356.

[127] N. Haghdadi, A. Zarei-Hanzaki, S. Heshmati-Manesh, H. Abedi, S. Hassas-Irani, The semisolid microstructural evolution of a severely deformed A356 aluminum alloy, Mater. Des. 49 (2013) 878–887.

[128] Y.-J. Baik, D. Yoon, Chemically induced migration of liquid films and grain boundaries in Mo-Ni-(Fe) alloy, Acta Metall. 34 (1986) 2039–2044.

[129] J. Y. Ko, S.-Y. Park, D. Y. Yoon, S.-J. L. Kang, Migration of intergranular liquid films and formation of core-shell grains in sintered TiC–Ni bonded to WC–Ni, J. Am. Ceram. Soc. 87 (2004) 2262–2267.

[130] M. Kuo, R. Fournelle, Diffusion induced grain boundary migration (DIGM) and liquid film migration (LFM) in an Al-2.07 wt% Cu alloy, Acta Metall. Mater. 39 (1991) 2835–2845.

[131] S. Barker, G. Purdy, On liquid film migration in aluminium–copper alloys, Acta Mater. 46 (1998) 511–524.

[132] W.-H. Rhee, Y.-D. Song, D. N. Yoon, A critical test for the coherency strain effect on liquid film and grain boundary migration in Mo-Ni (Co-Sn) alloy, Acta Metall. 35 (1987) 57–60.

[133] W.-H. Rhee, D. N. Yoon, The grain boundary migration induced by diffusional coherency strain in Mo-Ni alloy, Acta Metall. 37 (1989) 221–228.

[134] S. Annavarapu, R. Doherty, Inhibited coarsening of solid-liquid microstructures in spray casting at high volume fractions of solid, Acta Metall. Mater. 43 (1995) 3207–3230.

[135] S.-Y. Koo, G.-G. Lee, S.-J. L. Kang, Measurement of reduction kinetics in Nb2O5-doped SrTiO3 by use of a new technique of liquid film migration, J. Phys. Chem. Solids 66 (2005) 498–503.

[136] T.-H. Kim, T. Sasaki, T. Koyama, Y. Fujikawa, M. Miwa, Y. Enokido, T. Ohkubo, K. Hono, Formation mechanism of Tb-rich shell in grain boundary diffusion processed Nd–Fe–B sintered magnets, Scr. Mater. 178 (2020) 433–437.

[137] T. Muschik, W. Kaysser, T. Hehenkamp, Melting of Cu-In solid solutions at small superheating by droplet formation and liquid film migration, Acta Metall. 37 (1989) 603–613.

[138] Z. Li, L. Lührs, J. Weissmüller, Bicontinuous microstructure formation through partial melting, Scr. Mater. 250 (2024) 116192.

[139] S. Young-Duh, A. Sung-Tae, D. N. Yoon, Chemically induced migration of liquid film in W-Ni-Fe alloy, Acta Metall. 33 (1985) 1907–1910.

[140] L. Zhang, J. Fan, D. Liu, M. Zhang, P. Yu, Q. Jing, M. Ma, P. Liaw, G. Li, R. Liu, The microstructural evolution and hardness of the equiatomic CoCrCuFeNi high-entropy alloy in the semi-solid state, J. Alloys Compd. 745 (2018) 75–83.

[141] R. Chaim, A. H. Heuer, D. G. Brandon, Phase equilibration in ZrO2-Y2O3 alloys by liquid-film migration, J. Am. Ceram. Soc. 69 (1986) 243–248.

[142] E. Rabkin, B. Straumal, L. Shvindlerman, R. Fournelle, W. Gust, High temperature DIGM in an Fe–5 at.% Al bicrystal during zinc diffusion, Scr. Metall. Mater. 26 (1992) 901–906.

[143] E. P. Butler, A. H. Heuer, Grain-boundary phase transformations during aging of a partially stabilized ZrO2-A liquid-phase analogue of diffusion-induced grain-boundary migration (DIGM)(?), J. Am. Ceram. Soc. 68 (1985) 197–202.

[144] L. Fan, M. Zhou, Y. Zhang, Q. Tang, G. Quan, B. Liu, The semi-solid microstructural evolution and coarsening kinetics of AZ80-0.2Y-0.15Ca magnesium alloy, Mater. Charact. 154 (2019) 116–126.

[145] H. K. Schmid, Diffusion-induced grain-boundary migration in ceria-stabilized tetragonal zirconia polycrystals, J. Am. Ceram. Soc. 74 (1991) 387–394.

[146] R. A. Woods, Liquid film migration during aluminum brazing, Technical Report, SAE Technical Paper, 1997.

[147] M. Benoit, M. Whitney, M. Wells, H. Jin, S. Winkler, Liquid film migration in warm formed aluminum brazing sheet, Metall. Mater. Trans. A 48 (2017) 4645–4654.

[148] P. Peng, X. Li, J. Li, Y. Su, J. Guo, H. Fu, On migration of primary/peritectic interface during interrupted directional solidification of Sn-Ni peritectic alloy, Sci. Rep. 6 (2016) 24512.

[149] P. Peng, Migration of liquid particle from mushy zone interface in temperature gradient, Int. J. Heat Mass Transfer 142 (2019) 118467.

[150] H. Jin, M. Kozdras, B. S. Amirkhiz, S. Winkler, Liquid–solid interaction in Al-Si/Al-Mn-Cu-Mg brazing sheets and its effects on mechanical properties, Metall. Mater. Trans. A 49 (2018) 3091–3107.

[151] Y. J. Baik, J. K. Kim, D. Y. Yoon, The effect of elastic anisotropy on the migration of intergranular liquid films and the precipitation of a liquid phase in a Co-Cu alloy, Acta Metall. Mater. 41 (1993) 2385–2393.

[152] K.-W. Chae, D.-I. Chun, D.-Y. Kim, Y.-J. Baik, K.-Y. Eun, Microstructural evolution during the infiltration treatment of titanium carbide-iron composite, J. Am. Ceram. Soc. 73 (1990) 1979–1982.

[153] F.-S. Chen, A. King, The misorientation dependence of diffusion induced grain boundary migration, Scr. Metall. 20 (1986) 1401–1404.

[154] F.-S. Chen, A. King, Misorientation effects upon diffusion induced grain boundary migration in the copper-zinc system, Acta Metall. 36 (1988) 2827–2839.

[155] H. Y. Lee, S.-J. L. Kang, D. Y. Yoon, The effect of elastic anisotropy on the direction and faceting of chemically induced grain boundary migration in Al2O3, Acta Metall. Mater. 41 (1993) 2497–2502.

[156] B. Straumal, E. Rabkin, W. Lojkowski, W. Gust, L. Shvindlerman, Pressure influence on the grain boundary wetting phase transition in Fe-Si alloys, Acta Mater. 45 (1997) 1931–1940.

[157] J. W. Cahn, Critical point wetting, J. Chem. Phys. 66 (1977) 3667–3672.

[158] C. Ebner, W. Saam, New phase-transition phenomena in thin argon films, Phys. Rev. Lett. 38 (1977) 1486.

[159] A. Passerone, R. Sangiorgi, N. Eustathopoulos, P. Desré, Microstructure and interfacial tensions in Zn-In and Zn-Bi alloys, Met. Sci. 13 (1979) 359–365.

[160] B. Straumal, S. Polyakov, E. Mittemeijer, Temperature influence on the faceting of $\Sigma3$ and $\Sigma9$ grain boundaries in Cu, Acta Mater. 54 (2006) 167–172.

[161] P. Wynblatt, M. Takashima, Correlation of grain boundary character with wetting behavior, Interface Sci. 9 (2001) 265–273.

[162] A. Brokman, R. Balluffi, Coincidence lattice model for the structure and energy of grain boundaries, Acta Metall. 29 (1981) 1703–1719.

[163] H. Gleiter, On the structure of grain boundaries in metals, Mater. Sci. Eng. 52 (1982) 91–131.

[164] J. Li, S. J. Dillon, G. S. Rohrer, Relative grain boundary area and energy distributions in nickel, Acta Mater. 57 (2009) 4304–4311.

[165] G. S. Rohrer, Grain boundary energy anisotropy: a review, J. Mater. Sci. 46 (2011) 5881–5895.

[166] B. Straumal, T. Muschik, W. Gust, B. Predel, The wetting transition in high and low energy grain boundaries in the Cu (In) system, Acta Metall. Mater. 40 (1992) 939–945.

[167] M. Tsuda, T. Wada, H. Kato, Kinetics of formation and coarsening of nanoporous α-titanium dealloyed with Mg melt, J. Appl. Phys. 114 (2013).

[168] J. Dona, J. Gonzalez-Velasco, Mechanism of surface diffusion of gold adatoms in contact with an electrolytic solution, J. Phys. Chem. 97 (1993) 4714–4719.

[169] Y.-c. K. Chen-Wiegart, S. Wang, I. McNulty, D. C. Dunand, Effect of Ag–Au composition and acid concentration on dealloying front velocity and cracking during nanoporous gold formation, Acta Mater. 61 (2013) 5561–5570.

[170] I. McCue, A. Karma, J. Erlebacher, Pattern formation during electrochemical and liquid metal dealloying, MRS Bull. 43 (2018) 27–34.

[171] W. Kurz, D. Fisher, M. Rappaz, Fundamentals of solidification, trans tech publications ltd, 2023.

[172] W. Tiller, K. Jackson, J. Rutter, B. Chalmers, The redistribution of solute atoms during the solidification of metals, Acta Metall. 1 (1953) 428–437.

[173] M. Hillert, Phase equilibria, phase diagrams and phase transformations: their thermodynamic basis, 2nd ed., Cambridge University Press, Cambridge, UK, 2008.

[174] K. G. F. Janssens, D. Raabe, E. Kozeschnik, M. A. Miodownik, B. Nestler, Computational materials engineering: an introduction to microstructure evolution, Academic Press, 2010.

[175] G. Haidemenopoulos, A. Katsamas, H. Kamoutsi, Thermodynamics-based computational design of Al-Mg-Sc-Zr alloys, Metall. Mater. Trans. A 41 (2010) 888–899.

[176] M. Bonvalet-Rolland, T. Philippe, J. Ågren, Kinetic theory of nucleation in multicomponent systems: An application of the thermodynamic extremum principle, Acta Mater. 171 (2019) 1–7.

[177] L. Lührs, Mechanical properties of nanoporous metals: model experiments and technology-relevant materials, Ph.D. thesis, Hamburg University of Technology, 2020. doi:`10.15480/882.2778`.

[178] Z. Li, L. Lührs, T. Krekeler, J. Weissmüller, How peritectic melting forms bicontinuous microstructures, Acta Mater. 289 (2025) 120917.

[179] O. Dezellus, R. Arroyave, S. G. Fries, Thermodynamic modelling of the Ag–Cu–Ti ternary system, Int. J. Mater. Res. 102 (2011) 286–297.

[180] R. Van Thyne, W. Rostoker, H. Kessler, Observations on the phase TiAg, Trans. Am. Inst. Min., Metall. Pet. Eng. 197 (1953) 670–671.

[181] R. W. G. Wyckoff, R. W. Wyckoff, Crystal structures, volume 1, Interscience publishers New York, 1963.

[182] W. Burgers, On the process of transition of the cubic-body-centered modification into the hexagonal-close-packed modification of zirconium, Physica 1 (1934) 561–586.

[183] T. Furuhara, S. Takagi, H. Watanabe, T. Maki, Crystallography of grain boundary α precipitates in a β titanium alloy, Metall. Mater. Trans. A 27 (1996) 1635–1646.

[184] H. Donthula, B. Vishwanadh, T. Alam, T. Borkar, R. Contieri, R. Caram, R. Banerjee, R. Tewari, G. Dey, S. Banerjee, Morphological evolution of transformation products and eutectoid transformation (s) in a hyper-eutectoid Ti-12 at% Cu alloy, Acta Mater. 168 (2019) 63–75.

[185] C. Mahr, J. A. Tapia Burgos, M. Schowalter, A. Wittstock, A. Rosenauer, Investigation of the dealloying front in partially corroded alloys, Mater. Res. Lett. 10 (2022) 824–831.

[186] Y. Xia, Z. Lu, J. Han, F. Zhang, D. Wei, K. Watanabe, M. Chen, Bulk diffusion regulated nanopore formation during vapor phase dealloying of a Zn-Cu alloy, Acta Mater. 238 (2022) 118210.

[187] Z. Li, L. Lührs, J. Weissmüller, Microstructure refinement and bicontinuity formation by distributed internal melting at the Ni3Sn4 peritectic, Journal of Materials Research and Technology 41 (2026) 6202–6210.

[188] C. Schmetterer, H. Flandorfer, K. W. Richter, U. Saeed, M. Kauffman, P. Roussel, H. Ipser, A new investigation of the system Ni–Sn, Intermetallics 15 (2007) 869–884.

[189] A. Figueredo, M. Cima, M. Flemings, J. Haggerty, Directional phase formation on melting via peritectic reaction, Metall. Mater. Trans. A 25 (1994) 1747–1760.

[190] A. Bolcavage, S. Chen, C. Kao, Y. Chang, A. Romig, Phase equilibria of the Cu-In system i: Experimental investigation, J. Phase Equilib. 14 (1993) 14–21.

[191] Z. Bahari, E. Dichi, B. Legendre, J. Dugué, The equilibrium phase diagram of the copper–indium system: a new investigation, Thermochim. Acta 401 (2003) 131–138.

[192] D. Brandon, The structure of high-angle grain boundaries, Acta Metall. 14 (1966) 1479–1484.

[193] H. Rösner, S. Parida, D. Kramer, C. A. Volkert, J. Weissmüller, Reconstructing a nanoporous metal in three dimensions: An electron tomography study of dealloyed gold leaf, Adv. Eng. Mater. 9 (2007) 535–541.

[194] R. Li, N. Wu, J. J. Liu, Y. Jin, X. B. Chen, T. Zhang, Formation and evolution of nanoporous bimetallic Ag-Cu alloy by electrochemically dealloying Mg-(Ag-Cu)-Y metallic glass, Corros. Sci. 119 (2017) 23–32.

[195] L. Yang, Y. Q. Shi, L. J. Shen, E. L. Zhang, G. W. Qin, X. P. Lu, X. R. Zhou, Effect of Ag on cathodic activation and corrosion behaviour of Mg-Mn-Ag alloys, Corros. Sci. 185 (2021) 109408.

[196] R. W. Balluffi, J. W. Cahn, Mechanism for diffusion induced grain boundary migration, Acta Metall. 29 (1981) 493–500.

[197] H. Fredriksson, T. Nylen, Mechanism of peritectic reactions and transformations, Met. Sci. 16 (1982) 283–294.

[198] D. StJohn, The peritectic reaction, Acta Metall. Mater. 38 (1990) 631–636.

[199] H. Shibata, Y. Arai, M. Suzuki, T. Emi, Kinetics of peritectic reaction and transformation in Fe-C alloys, Metall. Mater. Trans. B 31 (2000) 981–991.

[200] M. Hillert, B. Uhrenius, Eutectoid and peritectoid reactions in alloyed steels, Scand. J. Metall. (1972).

[201] M. Hillert, L. Höglund, Melting of a peritectic phase, Scr. Mater. 50 (2004) 1055–1059.